School of Electrical Engineering, Computing and Mathematical Sciences

Calibrating Low Frequency Aperture Arrays With High Sidelobes: Imaging at 300 MHz With the Murchison Wide-field Array

Jaiden Hue Cook

0000-0001-8001-0791

**This thesis is presented for the Degree of
Master of Research (Physics)
of
Curtin University**

July 2020

Declaration

To the best of my knowledge and belief this thesis contains no material previously published by any other person except where due acknowledgement has been made.

This thesis contains no material which has been accepted for the award of any other degree or diploma in any university.

Signature: ....

Date: ....

Abstract

In the regime where the observing wavelength is comparable to the dipole separation in low-frequency aperture array tiles, the grating sidelobes for the tile primary beam response become very prominent. These grating sidelobes are reflections of the main lobe, and are comparable in size and sensitivity. For the Murchison Wide-field Array (MWA), this regime occurs at higher frequencies around 300 MHz. These highly sensitive sidelobes are typically located far from the main lobe, making traditional calibration methods difficult. As a result until now, MWA observations at 300 MHz have largely been ignored. With the advent of all sky surveys such as the Galactic And Extra-galactic MWA (GLEAM) survey, in conjunction with accurate models of the MWA tile primary beam pattern, it is now possible to calibrate observations using a large number of field sources rather than a single calibrator source. This method works by attenuating a model of the sky with a model of the MWA tile primary beam at a particular frequency to create an apparent sky-model. With this apparent sky-model it is possible to predict and therefore calibrate MWA observations. This calibration method is called sky-model calibration. The sky-model calibration method is applied to MWA observations at 300 MHz, using a 300 MHz sky-model developed in this project. This model is created by interpolating the 300 MHz flux density from a composite catalogue that covers the frequency range of 72 MHz to 1400 MHz. This composite catalogue is a subset of the GLEAM and 150 MHz TGSS surveys cross-matched with higher frequency all-sky surveys (e.g. NRAO VLA all-sky survey at 1.4 GHz). The resulting sky-model contains $433,345$ radio sources covering the southern sky below DEC $< +45$ deg. Using this model and the MWA tile primary beam model, two observations are calibrated; one with a bright dominant source, and one without. With the calibrated data from these two observations, two 2.4 arcminute resolution all-sky images are created. An imaging strategy was developed which uses these all-sky images to subtract the contribution of the grating sidelobes from the observation visibilities. This subtraction allows for higher dynamic range images of the main lobe. Using this image subtraction method deep images of the main lobe for five observations at 300 MHz were created. The median rms for these five snapshot observations was ~ 31 mJy/beam. With the work in this project there now exists a method to calibrate and image MWA observations at 300 MHz.

Acknowledgements

Contents

List of Figures

Chapter 1

Introduction

Low frequency aperture arrays (LFAA) are a type of radio telescope composed of tiles or stations, which are a collection of phased array dipole antennas that are fixed to the ground. The Murchison Wide-field Array (MWA) is a type of LFAA which is a precursor instrument to the Square Kilometre Array Low (SKA-Low). The MWA is capable of observing from $70-320\,\mathrm{MHz}$, and is comprised of 256 tiles, where each tile is a collection of 16 bow-tie dipole antennas, capable of observing the linear X and Y polarisations (Tingay et al., 2013; Ord et al., 2015). In contrast the elements of dish arrays are the dish and receiver system. In this system the dipole/receiver is typically fixed at the focus of the dish which is parabolic in shape. The additional collecting area of the dish increases the sensitivity of the array in comparison to a single dipole on the ground. Unlike LFAA tiles, dishes are capable of being mechanically pointed toward target observations. An example array is the Karl G Jansky Very Large Array (VLA), an array which consists of 27 dishes, capable of observing in the frequency range $1-50\,\mathrm{GHz}$ (Thompson et al., 1980; Perley et al., 2011). Dish arrays become less practical at lower frequencies ($\lesssim 150\,\mathrm{MHz}$) since, as the size of dipoles increases, so to does the necessary scale of the dishes. There is a practical size limit that dishes can be before they collapse under their own weight (Greenbank 1988 telescope collapse for example). Additionally large dishes are expensive and time consuming to construct, so LFAA's are typically preferred at lower frequencies.[1]

Both radio dishes and tiles observe the sky by projecting a frequency, altitude and azimuth dependent sensitivity pattern called the primary beam, which by design is peaked around the pointing centre. The tile primary beam pattern for the MWA is essentially the super position of the antenna patterns of individual dipoles, whereas for a dish antenna the primary beam pattern is determined by the size and nature of the dish, and the receiver. Determining the dependence of the tile primary beam pattern on the altitude, azimuth and frequency of the observations, requires the development of accurate beam models from simulation, as described in Sutinjo et al. (2015); Sokolowski et al. (2017). Using a realistic physical model for an MWA tile, Sokolowski et al. (2017) created the most accurate Fully Embedded Element (FEE) tile beam model in the frequency range $72-315\,\mathrm{MHz}$.

---

[1]Dish arrays such as the VLA can be used to observe at lower frequencies. The lowest VLA band is the 4m band which covers the frequency range $58-84\,\mathrm{MHz}$.

(a) 80 MHz
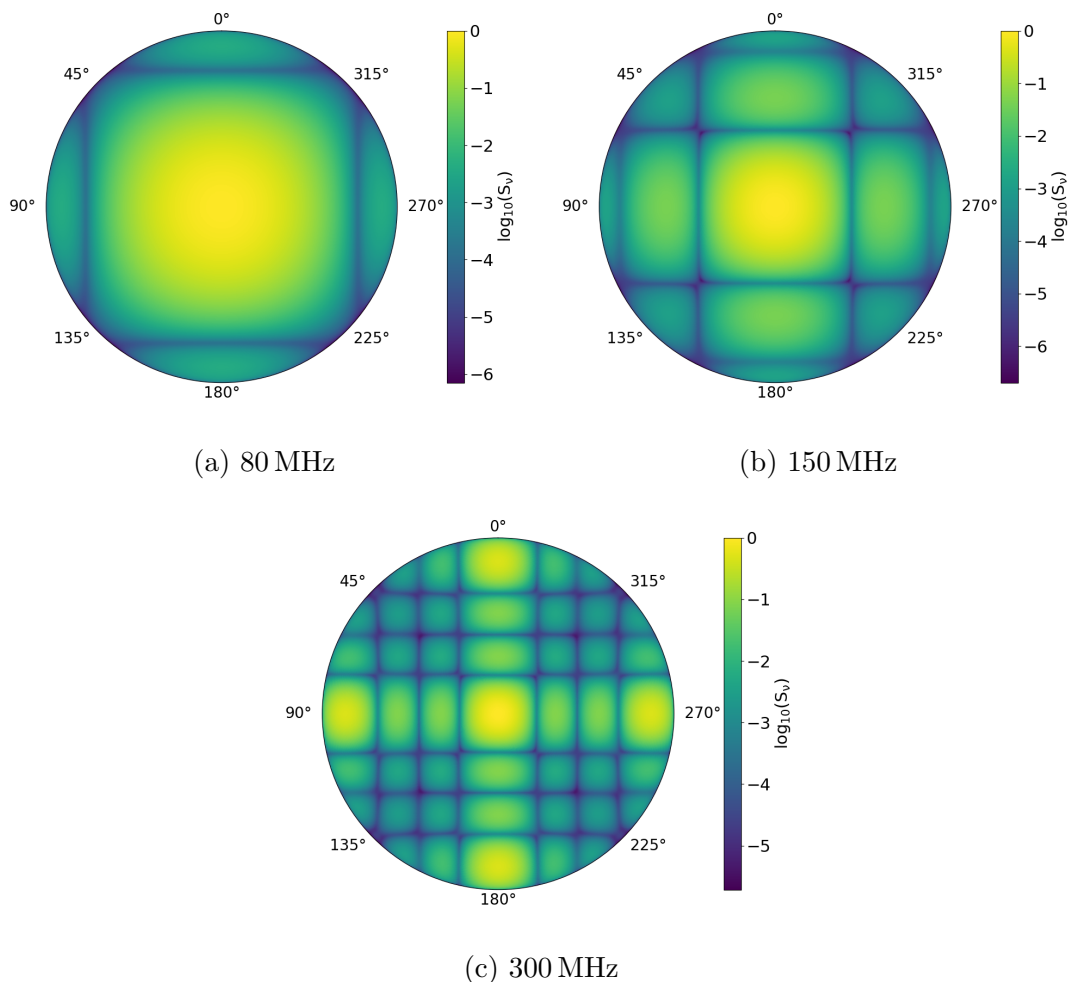
(b) 150 MHz

(c) 300 MHz

Figure 1.1: Shows the orthographic zenith pointing log-intensity tile primary beam patterns at approximately 80 MHz, 150 MHz and 300 MHz. At each frequency there is a main lobe at the centre with decreasing sensitivity away from zenith. Beyond the main lobe there are peaks in sensitivity called sidelobes. The grating sidelobes become apparent towards the horizon at 300 MHz, this is a result of the dipole spacing being close to the observing wavelength. These beams were produced with the FEE 2016 MWA tile beam model.

Examples of the model MWA tile primary beam sensitivity patterns can be seen in Figure 1.1, which shows a model of the logarithmic primary beam patterns for 80 MHz, 150 MHz and 300 MHz (Sokolowski et al., 2017). In each of the subfigures the primary beam patterns are for zenith pointing observations. Off zenith pointed observations have different primary beam shapes. This is due to the tile being fixed to the ground and hence not being able to point. In order to point off zenith, electronic delays need to be added to the signal path from each dipole in the tile beam former (Tingay et al., 2013). These electronic delays are discrete therefore the MWA can only be electronically pointed to a set of positions in a discrete grid across the sky. In contrast the primary beam pattern of a dish is largely independent of the pointing direction because it can mechanically point to the target field.[2]

Both dish and tile primary beam patterns are dominated by the main lobe. This can be seen for in Figure 1.1 which shows the main lobe at the centre of the image for each frequency. The main lobe of the primary beam determines the primary field of interest for a radio interferometric observation. This is because the main lobe is the region that is the most scientifically valuable[3]. The size of the main lobe is also frequency dependent where the half power beam width of the main lobe is inversely proportional to the frequency of the observation. Although the primary beam pattern is typically dominated by the main lobe, for both dishes and tiles there are additional regions of sensitivity known as sidelobes. These sidelobes are radially distributed away from the pointing centre and are typically less sensitive than the main lobe, but can detect exceptionally bright radio sources.

In the case of the MWA these sidelobes have a grating like pattern due to the regular square grid arrangement of the tile dipoles. In Subfigure 1.1c (the 300 MHz tile primary beam), there are four sidelobe regions of high sensitivity towards the horizon. These regions are called grating sidelobes and differ from the typical less sensitive sidelobes because they are reflections of the main lobe, and therefore have equal sensitivity to the main lobe in sine-projection. These reflections appear as the observing wavelength becomes comparable to the separation of dipoles in the tile. For the MWA this occurs at approximately a wavelength of 1 m which corresponds to an observing frequency of 300 MHz. These highly sensitive grating sidelobe regions at higher frequencies make calibrating and imaging 300 MHz MWA observations difficult.

Calibration of the elements in an interferometer are necessary as the signal path, including dish, receiver and back-end electronics, all potentially introduce random and systematic effects into the raw data. Calibration is the process by which these instrumental effects are calculated and hence corrected for in the data. Without this process data collected by radio interferometric instruments could not be used for scientific purposes. Traditional calibration methods (developed primarily for dish arrays) typically involve observing a bright unpolarised point source which dominates the main lobe. Radio interferometers when observing

---

[2]In reality the dish beam pattern is affected by reflections from the ground, deformation in the dish due to elevation, and for a non-equatorial mounted dish the primary beam will rotate while tracking a source over time.

[3]There are exceptions to this where the sidelobes are also used for scientific purposes.

the radio sky, measure a complex quantity known as a visibility. Each pair of tiles/dishes in an interferometric array measures a different visibility. This quantity has two main properties amplitude and a phase. The phase property has information about the position of the source, and the amplitude about the intensity. Not only do visibilities encapsulate the response of the source, but they include instrumental effects as well. For bright unpolarised point sources, the visibility amplitudes and the phases should be flat and stable. Deviations from this are likely due to instrumental effects and can be corrected for if the intensity and the position of the point source is known *a priori*. The resulting corrections are the calibration solutions. If the calibration solutions are stable over a long enough time period they can be transferred to other observations.

This traditional calibration method can be complicated for LFAA's such as the MWA especially at lower frequencies, where a tile is sensitive to a much larger fraction of the visible sky. Many bright sources can be present and need to be accounted for to properly calibrate the observation visibilities. Even with an accurate primary beam model, the direction dependent effects of the beam and the ionosphere limit calibration solutions for MWA observations to be transferred only to nearby observations at a similar pointing. In the Galactic and Extragalactic all-sky MWA survey (GLEAM), Wayth et al. (2015) conducted MWA observations using a drift scan approach. This drift scan approach effectively means that the MWA observed with a fixed altitude and azimuth[4] at each pointing in an observing run. For a fixed declination (DEC) a bright calibrator source such as 3C444 was observed for initial gain and phase solutions. This method obtained solutions good enough that a self-calibration process could be applied to further improve the solutions. This was necessary since most of this sky had not yet been observed at these frequencies, so initial calibration was required to create an initial flux scale (Hurley-Walker et al., 2017).

With the advent of an all sky survey with MWA in the frequency range of $72 - 231\,\text{MHz}$, and in conjunction with other all-sky low-frequency radio surveys, calibration of MWA observations without a specifically bright calibrator source in the FoV is possible. This sky model method first described by Mitchell et al. (2008) and implemented in the algorithm CALIBRATE by Offringa et al. (2016) has been utilised to calibrate MWA observations. This is done by using a model of the sources within the FoV attenuated by the tile primary beam model to determine the calibration solutions. This model of the sky attenuated by the MWA tile primary beam model is called an apparent sky model, this is what the MWA is predicted to see for that particular observation. This prediction can be used to determine the instrumental contributions to the visibilities and hence find calibration solutions.

At higher MWA frequencies, since most of the sensitivity is located in the grating sidelobes outside of the main lobe, observations of the whole southern sky at $300\,\text{MHz}$ have until now largely been unprocessed. A reliable method for calibrating MWA observations at $300\,\text{MHz}$ would open up the large volume of data for scientific use. Images of MWA observations at $300\,\text{MHz}$ are likely to overlap with those of some dish arrays. This is particularly important because the flux

---

[4]This corresponds to a fixed set of delays, pointing at only one point in the sky.

scale of the MWA can be directly compared to those of dish arrays. This comparison allows for a better understanding of the systematic differences between these two kinds of instrument, therefore providing a bridge between LFAA's and dish arrays. Samples at the higher frequency end of the MWA frequency range additionally provide better constraints on the models of spectral energy densities (SED) for radio sources. This is useful in understanding the radio spectrum of these sources and helping with their classification. If 300 MHz MWA observations can be calibrated for the XX and YY polarisation components polarimetry becomes possible. Astrophysical sources are more likely to be polarised at higher frequencies. Additionally, there may be transient radio sources or sources with positive spectral indices which cannot be detected at lower MWA frequencies. Lastly there may be radio sources with peaks at higher MWA frequencies which cannot be detected at the lower MWA frequency range.

Theoretically, with a good beam model, and a good model of the sky at 300 MHz using a least squares sky-model calibration method, it should be possible to calibrate the visibilities for MWA observations in the high frequency regime. In this project I use the existing MWA all-sky survey (GLEAM) as a base catalogue, combined with higher frequency surveys to create a model of the sky at 300 MHz. I then apply this 300 MHz sky catalogue with the FEE MWA tile beam model, to create calibration sky models for any given snapshot observation, enabling high-quality imaging. These are then used to calibrate and image 300 MHz MWA observations for the first time. While this thesis is focused on developing a method to process 300 MHz observations, this will enable a wide range of scientific applications including those described above. The rest of the thesis is laid out as follows.

Chapter 2 covers the background theory necessary to understand the work I did in this project. The first Section of this Chapter characterises the dominant emission mechanism from extra-galactic radio sources. It then summarises the models used to describe the spectral energy distributions of extra-galactic radio sources, these will be useful in Chapter 4. The rest of the Chapter focuses on developing the framework for interferometry and the matrix formalism used by the MWA to store radio interferometric data. With the matrix format established the calibration of radio interferometric arrays using a sky-model approach is reviewed. This lays down the crucial background necessary to understand some of the tools I used to model, process and calibrate data in this project.

Chapter 3 further focuses on the surveys and instrumentation of the MWA. The main focus of this Chapter is the first data release of the all-sky survey conducted by the MWA. The next part of this Chapter focuses on the FEE MWA tile beam model. These are both crucial components required to process and calibrate MWA observations at 300 MHz.

In Chapter 4 I establish the method I used to create the 300 MHz sky model. This involves using the MWA first data release all-sky catalogue as a basis cross-matched with higher frequency all-sky catalogues. Here I interpolate the sky flux density at 300 MHz using the models discussed in Chapter 2. I also explore the use of other catalogues to fill in the missing gaps in the sky-model. I then finish the Chapter by analysing and discussing the total 300 MHz sky-model.

Chapter 5 discusses the apparent-sky calibration method, as well as the general calibration strategy I employed at 300 MHz. Here a secondary calibration method is also proposed which involves transferring calibration solutions from one observation to another. This Chapter also discusses self-calibration by using all-sky images at 300 MHz observations.

Chapter 6 describes the imaging method required to image MWA observations at 300 MHz. In this Chapter I outline the method I developed to iteratively reduce the observational data for a set of test observations. This iterative process then allows for the deep imaging of the main lobe of the observation.

In Chapter 7 I summarise the results, with a specific focus on the flux scale and the astrometry for five observations imaged in this work. It also outlines the pipeline developed to process, calibrate, and image MWA observations at 300 MHz. Finally Chapter 7 concludes the results of the thesis.

Chapter 2

Background Theory

In this Chapter I provide the reader with a comprehensive but brief overview of extra-galactic radio emission and radio interferometry. This Chapter will have a specific focus on how to represent the instrumental and measured radio interferometry quantities in a matrix format. This format is how MWA data are represented. Additionally this format naturally leads to the discussion of the instrumental calibration algorithms I used to process MWA data for this project.

2.1 Characterising Extra-Galactic Radio Emission

The dominant emission mechanism for astrophysical radio sources is synchrotron radiation (Kardashev, 1962). This occurs when relativistic electrons are accelerated either through supernovae shocks, or in the case of extra-galactic radio sources, collimated into the vast radio jets of active galactic nuclei (AGN) (Condon, 1992). These electrons then interact with the host magnetic field of their galaxy which causes them to precess, and in turn emit radiation.

Power Law Model

The energy distribution of relativistic electrons can be represented by a power law (Kardashev, 1962). Electrons emit most of their radiation at one frequency, thus the radio Spectral Energy Distributions (SED) of radio sources can also be represented by a power law $S_\nu \propto \nu^\alpha$. Here, α is the spectral index and typically has a value of $\alpha \in [-0.8, -0.7]$ (Conway et al., 1963; Condon, 1992). The resulting power law for the radio spectrum can be represented in log-space as the equation of a straight line:

$$\log_{10}(S_\nu) = \log_{10}(S_{0,\nu}) + \alpha \left(\log_{10} \left(\frac{\nu}{\nu_0} \right) \right) \qquad (2.1)$$

In Equation 2.1 ν_0 is the reference frequency (which is also called the characteristic frequency), and $S_{0,\nu}$ is the flux density at the reference frequency.

7

Second Order Polylogarithmic Model

In reality the spectra of radio sources are more complex than a simple power law, and often there can be curvature in the spectrum as a result of many different extrinsic and intrinsic mechanisms. Two primary forms of curvature and peaks in the spectrum occur due to free-free absorption (FFA), and synchrotron self absorption (SSA). FFA occurs when the brightness temperature of the emission spectra is in thermal equilibrium with the surrounding diffuse plasma. This occurs typically if the surrounding medium is dense (Condon, 1992; Callingham et al., 2017). This causes a peak in the spectrum and results in a positive spectral index at lower frequencies. In a similarly simple treatment of SSA, this occurs when the brightness temperature at a particular frequency of emission is equal to the thermal temperature of the relativistic gas (Condon, 1992). This causes a peak in the spectrum due to absorption at low frequencies. These peaks can occur at different frequencies depending on the temperature of emission, or the redshift of the radio source. Peaks can also shift as the radio lobes adiabatically expand, and hence cool. These are all systems that display negative or concave curvature ($q < 0$), but it is possible for sources to display convex curvature ($q > 0$). This can arise due to multiple epochs of AGN activity, especially in the centre of cool clusters as seen by Hogan et al. (2015), or in isolated cases where the breaks in the spectrum could potentially be caused by tidal interruptions or mergers with the host galaxy (Hancock et al., 2010). The super position of multiple epochs can lead to convex curvature in the SED of radio sources.

The prevalence of sources with curved spectra is such that we should expect to see sources with peaks in their spectrum. This has been observed in lower MWA bands; see Callingham et al. (2017); Harvey et al. (2018). To model the curvature in these sources' spectra, a second order polylogarithmic function was used by Blundell et al. (1999); Duffy & Blundell (2012); Callingham et al. (2017); Harvey et al. (2018). Although this function is not a physical representation of the curvature, the curvature can be related to the magnetic field strength, and thus the relativistic electron energy density, as seen in Duffy & Blundell (2012). Additionally the second order polylogarithmic function and the log-power law are nested functions, where the log-power law is simply a first order polylogarithmic function. This means in the limit of small curvature the power law is a good approximation for the second order polylogarithmic function. The second order polylogarithmic function is defined below:

$$\log_{10}(S_\nu) = \log_{10}(S_{0,\nu}) + \alpha \left(\log_{10} \left(\frac{\nu}{\nu_0} \right) \right) + q \left(\log_{10} \left(\frac{\nu}{\nu_0} \right) \right)^2 \qquad (2.2)$$

In Equation 2.2 the parameter q represents the curvature of the spectra. The α term in this case represents the steepness at the reference frequency ν_0, as before.

This characterisation of radio emission from extra-galactic radio sources will be particularly useful in Chapter 4 when I develop the 300 MHz sky model. For now we set aside the modelling tools of equations 2.1 and 2.2, and we focus on the fundamentals of radio interferometry. It is with the measurements made by radio interferometers that the aforementioned tools can be applied to interpret the radio continuum emissions produced by various sources in our universe.

2.2   Radio Interferometry

In sufficiently general terms, radio interferometry is the science of measuring the interference patterns of incident radiation using an array of receptors, and using these measurements to reconstruct the brightness distribution of the incident radiation source. This is more formally laid out by Thompson (2017), but for this treatise a simple example will be considered. Consider the setup in Figure 2.1 which shows two antennas conveniently labelled "1" and "2" that form a baseline denoted by the vector $\vec{b}$. For the time being instrumental effects for the individual antenna signal paths will be ignored. The goal of this example is simply to establish the basic concepts of interferometry.

   Now consider a quasi-monochromatic point source located in the far field[1] which is unpolarised and emitting radiation incoherently. This point source is additionally located in the phase centre of both antennas, where the phase centre is simply located at the pointing centre of the radio dish. Sources outside of the central pointing of the dish have a phase delay. Considering a Cartesian coordinate system, if a source is in the far field the incident radiation can be represented by a plane wave which propagates in the z direction along the line of sight. The two antennas are pointed in the direction of $\hat{s}$ which is parallel to the propagation path of the incident radiation. This forms an angle θ with the baseline vector $\vec{b}$. As the plane wave radiation is received by both antennas the oscillating electric field induces a voltage in each antenna denoted V_1 and V_2. The plane wave has to travel an extra distance $\vec{b} \cdot \hat{s} = c\tau_g$, where τ_g is the time difference it takes for the incident wave to reach antenna "1" once it is received by antenna "2", and is called the geometric delay. This difference introduces a phase offset in antenna "1" given by $\omega\tau_g$ where $\omega = \nu/2\pi$, and ν is the frequency of the emitted radiation. Taking this phase offset into account when measuring the voltages, the two induced voltages are then multiplied together, and averaged in time and frequency. This cross correlation of the two voltages creates the response (R_c) for this particular baseline defined in Figure 2.1, and is given below:

$$R_C = \langle V_1 V_2 \rangle = \left(\frac{V^2}{2}\right)\cos\omega\tau_g \tag{2.3}$$

Here $\langle\,\rangle$ denotes the time average of the data. This effectively projects an interference pattern on the sky for this particular baseline. But this only measures the response of the even components, so an additional measurement of the odd components is made with a $\pi/2$ offset:

$$R_S = \left(\frac{V^2}{2}\right)\sin\omega\tau_g. \tag{2.4}$$

   By measuring the even and odd components, the total interference pattern can be measured. This allows for the convenient representation in exponential form, which is a complex valued function called the *visibility*:

$$\mathcal{V} = Ae^{-i\phi}. \tag{2.5}$$

---

[1]The far field approximation simply denotes that the radiation emitted from the quasi-monochromatic point source can be represented by a plane wave.
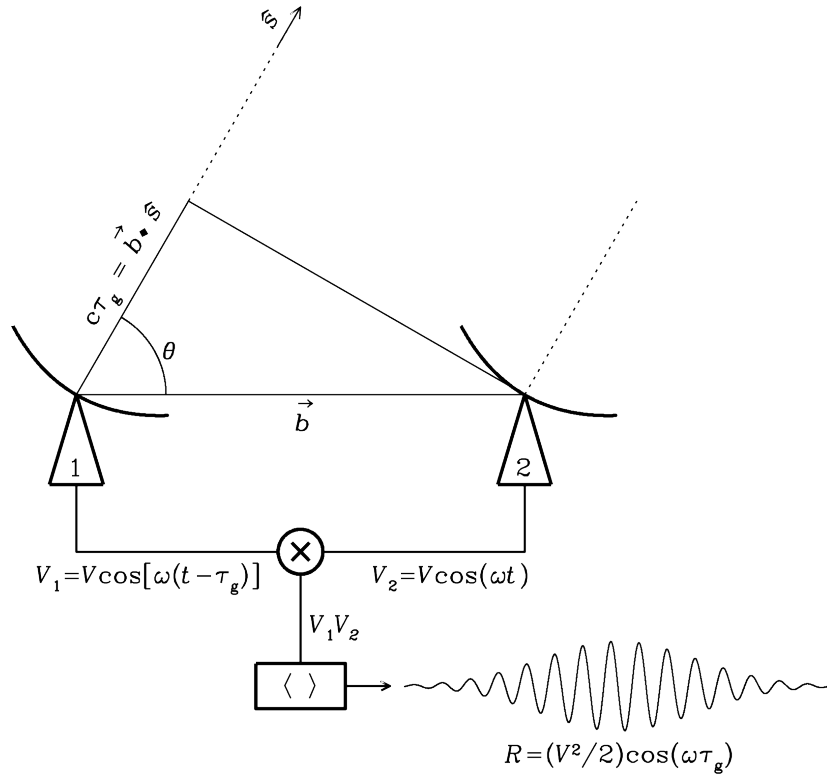
Figure 2.1: In this diagram two antennas "1" and "2" form a baseline $\vec{b}$. Incident plane wave radiation propagating from the far field is incident on both antennas, which induces a voltage that is correlated to form the response of this particular baseline. Image retrieved from NRAO
(https://www.cv.nrao.edu/course/astr534/Interferometers1.html).

In the above equation the fringe phase ϕ gives information about the source position and is baseline length dependent. The source position in the sky relative to the antenna pair has a projected baseline length. This projected length changes as the source moves through the sky. The position information encapsulated by the phase can be incredibly accurate if the projected baseline is many wavelengths long. The amplitude A is related to the flux density of the source. Here the visibilities measure the coherence of the incident radiation in the visibility space defined by the coordinates (u, v, w). These coordinates are the spatial frequencies defined in the observers space in terms of wavelengths. The Coordinates u and v are representative of the East-West and North-South spatial frequencies for the measured baseline projection. The w-term is parallel to the line of sight, and is defined as zero at the pointing/phase centre. The visibility (which is a coherency measurement), is non-zero for astronomical sources because the incident radiation is somewhat correlated. Even though the radiation from the source is incoherent, due to its location in the far field there is a correlation in the recieved radiation. These coherency measurements can be related to the brightness distribution of the radiating source through the Van Cittert-Zernike (VCZ) theorem (Thompson, 2017)[2]:

---

[2]The VCZ theorem is also known as the mutual coherence function

$$\mathcal{V}(u,v,w) = \int_{-\infty}^{\infty} \int_{-\infty}^{\infty} \frac{B(l,m)I(l,m)}{\sqrt{1-l^2-m^2}}$$
$$\times \exp{-2\pi i \left(ul + vm + w \left(\sqrt{1-l^2-m^2} - 1 \right) \right)} dl\,dm \tag{2.6}$$

The direction cosines as defined by l, m, and $\sqrt{1-l^2-m^2}$ form the basis of the image plane. Where the direction cosine $\sqrt{1-l^2-m^2}$ is the unit vector along the line of sight. The direction cosines can be used to define the phase centre in the image plane which is located at $l=m=0$. I is the Stokes intensity at a particular (l,m) in the image plane. $B(l,m)$ is the primary beam pattern of the dish which attenuates the intensity. Therefore the visibility function above is defined at a particular baseline projection (u,v,w), which is integrated over the entire intensity distribution for every (l,m) in the image plane.

This result is important because it underpins all of interferometric radio astronomy, but it is not an easily understandable concept. From Equation 2.6 by applying an inverse Fourier Transform (FT) the brightness distribution can be reconstructed. In principle this is more complicated than the previous statement alludes to, especially when dealing with arrays which have a wide Field of view such as the MWA. Sources with increasing angular distance from the pointing centre in the field of view also have increasing w-terms. For relatively small fields of view the w-terms can be approximated to be zero, and the denominator term $\sqrt{1-l^2-m^2}$ can be subsumed into the primary beam $B(l,m)$. Using these assumptions it is then possible to write the inverse Fourier transform of the visibility function independent of the w-terms:

$$\frac{B(l,m)I(l,m)}{\sqrt{1-l^2-m^2}} = \int_{-\infty}^{\infty} \int_{-\infty}^{\infty} \mathcal{V}(u,v) e^{2\pi i(ul+vm)} dl\,dm. \tag{2.7}$$

For the simple, single baseline dish array considered in this Chapter so far, this is approximately correct.[3] This approximation holds because dish arrays typically have small fields of view (typically on the order of a few degrees). The field of view is inversely proportional to the dish size, and directly proportional to the observing wavelength. For aperture arrays such as the MWA, the tiles have relatively small collecting areas, and observe at large wavelengths in comparison to dish arrays. As a result aperture arrays typically have very large fields of view relative to dish arrays and this approximation does not hold. There are ways to deal with these large terms, in lieu of doing a full three dimensional Fourier Transform, for example w-stacking (Offringa et al., 2014). This will be further discussed in Section 5.4 which is related to imaging with the MWA.

For now it is important to just establish the relationship between the mutual coherence function and the brightness distribution of the sky. In the next Section this will be recast into a matrix formalism. The formalism is the same for aperture arrays like the MWA, the only differentiation comes about in regards to the w-terms to account for the wide field of view correctly. The discussion in the following Subsection will also introduce instrumental effects, a necessary component for understanding instrumental calibration.

---

[3]Although this is correct there is a phase error of $\pi \left(l^2 + m^2 \right) w$.

2.2.1   The Measurement Equation

A useful approach for representing the complex visibilities measured by radio interferometers, is to represent them in a matrix format as outlined in the fundamental series of papers (Hamaker et al., 1996; Sault et al., 1996; Hamaker & Bregman, 1996; Hamaker, 2000). This notation is useful for many reasons, in particular it allows for the representation of the data in polarisation components. As will be seen later in this Section, this allows for the straightforward determination of the Stokes parameters (McMaster, 1954). This Subsection will use a similar notation to that laid out in the series of papers (Smirnov, 2011a,b) where Smirnov (2011a) revised the work performed by Hamaker et al. (1996). As in the preceding Subsection, a quasi-monochromatic unpolarised point source at a single time step which is fixed in space and emitting plane wave radiation is considered. This plane wave radiation propagates in the z direction oscillating in the (x, y) plane. Hence the electric field can be represented with the Cartesian orthonormal basis by the linearly independent x and y components:

$$\mathbf{e} = \begin{pmatrix} e_x \\ e_y \end{pmatrix}. \tag{2.8}$$

This vector representation of the electric field can be used with other bases such as the left and right circular polarisation components. Generally a plane wave can be decomposed into two linearly independent polarised components. If the plane wave is unpolarised both of these components have the same amplitude. Polarisation occurs when there is a difference in the amplitudes of the two components.

Now consider the plane wave radiation as it propagates along the signal path to the antenna. As the electric field vector propagates from the source to the receptor it will undergo transformations both by the instrument and in propagation. The multiplicative effect of the transformations can be represented by a Jones matrix (Jones, 1941). Thus the actual electric vector that is measured $\mathbf{e}'$ is the transformation of the true electric signal vector $\mathbf{e}$ by the multiplicative effects of the signal path, represented by the Jones matrix $\mathbf{J}$:

$$\mathbf{e}' = \mathbf{J}\mathbf{e}. \tag{2.9}$$

This is a very useful and important description, because it allows for the formulation of the instrumental effects as well as other effects by Jones matrices. The Jones matrix can be decomposed into these individual effects, where each matrix represents a different component. Generally this can be represented as a matrix multiplication:

$$\mathbf{J} = \mathbf{J}_n \cdots \mathbf{J}_1 \tag{2.10}$$

Importantly these must be in order of the physical effects from right to left, since matrix multiplication is not a commutative operation.

Now consider the signal as it is measured by the antenna. It is measured as a complex voltage, which can also be represented as a vector ($\mathbf{v}$) of two linearly independent x and y components:
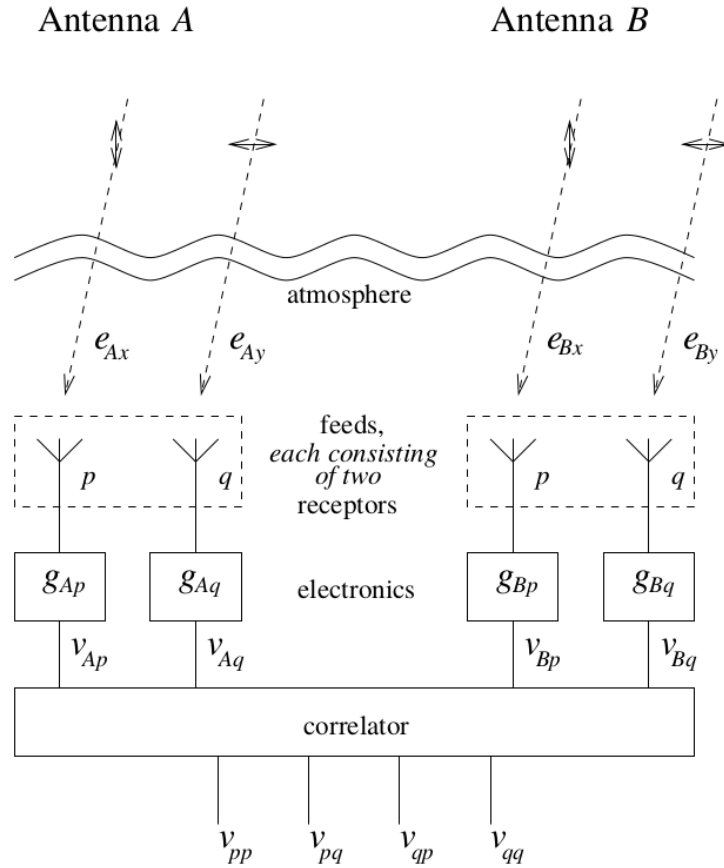
Figure 2.2: Shows the setup for an arbitrary baseline comprised of two antennas A and B. Here the receptors for the feed are general, such that the measured components can be circular polarisation components or linear polarisation components. Image retrieved from (Hamaker et al., 1996).

$$\mathbf{v} = \mathbf{J}\mathbf{e}. \tag{2.11}$$

This describes one signal path of propagating radiation to one antenna, but in interferometry antennas are considered in pairs, where each antenna has its own Jones matrix representing the slightly different transformations that occur along the individual signal paths. Now consider a pair of antennas represented in Figure 2.2 as displayed in Hamaker et al. (1996). In this diagram there are two antennas A and B (hereon i and j for notation consistency) each with their x and y linear polarisation feeds, which measure the incident plane wave radiation. The complex voltages from both antenna feeds are then multiplied together by the correlator and averaged in time and frequency to produce the four cross correlated components. This is what the interferometer measures and can be represented by the matrix multiplication of Equation 2.11 for antennas i and j:

$$\mathbf{V}_{ij} = \langle \mathbf{J}_i \mathbf{e} (\mathbf{J}_j \mathbf{e})^\dagger \rangle. \tag{2.12}$$

It is reasonable to assume that within the time frame for this particular observation, the Jones matrices are constant (in reality they can vary with both time and frequency). If this assumption holds they can be factored out of the averaging:

$$\mathbf{V}_{ij} = \langle \mathbf{J}_i \mathbf{e}\mathbf{e}^\dagger \mathbf{J}_j^\dagger \rangle = \mathbf{J}_i \langle \mathbf{e}\mathbf{e}^\dagger \rangle \mathbf{J}_j^\dagger = 2\langle \mathbf{v}_i \mathbf{v}_j^\dagger \rangle \tag{2.13}$$

Therefore expanding the matrix product out:

$$\mathbf{V}_{ij} = 2 \begin{pmatrix} \langle v_{ix,c} v_{jx,c}^* \rangle & \langle v_{ix,c} v_{jy,c}^* \rangle \\ \langle v_{iy,c} v_{jx,c}^* \rangle & \langle v_{iy,c} v_{jy,c}^* \rangle \end{pmatrix}. \tag{2.14}$$

Equation 2.14 represents the four cross-correlations from the two antennas for each complex voltage component. Formally this is the coherence matrix, but is more intuitively referred to by Smirnov (2011a) as the *Visibility Matrix*[4]. This is a useful representation because it can be used to directly relate the measurements to the Stokes parameters (I, Q, U, V) through the brightness matrix:

$$\mathbf{B} = 2 \begin{pmatrix} \langle e_{ix} e_{jx}^* \rangle & \langle e_{ix} e_{jy}^* \rangle \\ \langle e_{iy} e_{jx}^* \rangle & \langle e_{iy} e_{jy}^* \rangle \end{pmatrix} = \begin{pmatrix} I+Q & U+iV \\ U-iV & I-Q \end{pmatrix} \tag{2.15}$$

The Stokes parameters are described in Section B.1 of the appendix. This allows Equation 2.14 to be rewritten into a more familiar form:

$$\mathbf{V}_{ij} = \mathbf{J}_i \mathbf{B} \mathbf{J}_j^\dagger. \tag{2.16}$$

The above equation is referred to as the radio interferometer measurement equation (RIME), and is the matrix representation of the actual measurement products of an interferometer. From the RIME it is possible to almost trivially rederive the VCZ theorem (Thompson, 2017), but for this treatment it is only necessary to see the connection between the visibility matrix and the Stokes parameters. This concept can be extended from a simple point source to a collection of point sources which is the case encountered by arrays with a wide FoV such as the MWA:

$$\mathbf{V}_{ij} = \sum_s \mathbf{J}_{si} \mathbf{B}_s \mathbf{J}_{sj}^\dagger \tag{2.17}$$

In Equation 2.17 the sum is over the response to all point sources in the sky, where the subscript s denotes a given particular source. Since each source visibility is linearly independent, the total visibilities as measured by the response from the baseline ij, is just the sum of the individual visibilities from all point sources. This concept will be useful later when sky-model calibration is discussed.

Up until this point we have only been considering the visibilities measured from the cross-correlation of a single baseline pair ij. In Leshem et al. (2000) they extend this notion to describe the response of the entire array in terms of a covariance matrix $\mathbf{R}$. Each term in the covariance matrix $\mathbf{R}$ is a realisation of the visibility measurement for a pair of antennas ij, which samples a unique point in the (u, v) plane (at a given moment in time). Since the baseline projections for each antenna pair ij changes with time due to Earth's rotation, each time integration probes a different part of the (u, v) plane. Additionally since observations take place over a range of frequencies, there is a covariance matrix for each frequency channel. Each frequency sample f and time sample t therefore

---

[4]For the argument as to why there is a factor of two out the front of the visibility matrix refer to (Smirnov, 2011a).

has a corresponding covariance matrix $\mathbf{R}_{ft}$ which is the realisation of the array response at that time and frequency. Throughout this Chapter we will maintain the ij definition for a single antenna pair, since each baseline is independently calibrated.

With the matrix formalism established in Equation 2.17 it is possible to describe a radio interferometer's response to the sky for a particular baseline. This response is determined by the individual point sources that make up the sky Stokes I brightness intensity distribution, and the instrumental effects applied to that brightness distribution by the antennas. Therefore to reconstruct the brightness map one needs to invert the Jones matrices that describe these effects. The process of computing the Jones matrices is called calibration. The methods to calibrate and hence derive corrected data with which to image, are discussed in the following Subsection.

2.2.2 Calibration of Interferometers

In order to determine the values of the Stokes parameters and ultimately the brightness distribution (I), the instrumental effects which in Equation 2.16 are represented by the Jones matrices need to be determined (Sault et al., 1996; Mitchell et al., 2008; Smirnov, 2011a). Calibration is the process by which the instrumental Jones matrices are derived and then inverted from the visibilities. Traditional calibration of radio interferometers typically involves observing a bright unpolarised point source with a known intensity. Since interferometers typically have many elements, and hence $N(N-1)/2$ baselines, the order of unknown quantities N is readily solvable with numerical processes. Once the Jones matrices are determined the solution can readily be transferred to other observations at the same frequency which are close in time. This solution transfer assumes that the solutions are time invariant which is not necessarily true, but is a reasonable assumption on short enough timescales.

Introduction to Sky Model Calibration

For interferometers with larger fields of view the traditional single point source calibration method is often impractical. In many cases there can be many bright radio sources, some of which are far from the phase centre of the observation, which have substantial contributions to the visibilities. In these situations the sky can be modelled as a collection of N_c point sources. Since there are sources away from the phase centre there are two types of effects that need to be accounted for when calibrating the visibilities (Sault et al., 1996; Mitchell et al., 2008; Smirnov, 2011a). There are the direction independent effects (DIE) such as the complex gains for antennas, and there are direction dependent effects (DDE) such as ionospheric effects and primary beam effects (Smirnov, 2011b). Some of these effects may be known *a priori* or can be estimated through simulations such as the instrumental beam. This is not necessarily the case for other effects such as polarisation leakage and the gain terms. These effects need to be calibrated for by least squares estimation from the measured visibilities. Linear arguments can be applied in most cases to ignore higher order effects which makes estimating the effective Jones matrices simpler. Once they have been estimated they can be

inverted and the Brightness matrix $\mathbf{B}$ for a particular baseline projection can be determined.

For this Section a rather simple example for DIE and DDE will be considered. This will come in handy in later Sections when discussing the MWA beam model, as well as DDE calibration in the following Section. For a more comprehensive treatment refer to (Hamaker et al., 1996; Hamaker, 2000; Smirnov, 2011a,b). These two series of papers (specifically the first) go much more in depth into the other effects such as leakage which constitute non-diagonal matrices. In an attempt to build up an intuitive understanding of calibration only diagonal matrices are considered. For now it is convenient to consider the Jones matrix in Equation 2.16 which can be factored into a direction dependent and a direction independent form:

$$\mathbf{J} = \mathbf{GEK}. \tag{2.18}$$

The matrix $\mathbf{G}$ represents the DIE complex gain terms:

$$\mathbf{G} = \begin{pmatrix} g_x & 0 \\ 0 & g_y \end{pmatrix} \tag{2.19}$$

The matrix $\mathbf{E}$ represents the DDE of the primary beam:

$$\mathbf{E}(l,m) = \begin{pmatrix} e_x(l,m) & 0 \\ 0 & e_y(l,m) \end{pmatrix} \tag{2.20}$$

Matrix $\mathbf{K}$ constitutes a phase term which could represent ionospheric effects or even Faraday rotation:

$$\mathbf{K} = \begin{pmatrix} e^{i\phi} & 0 \\ 0 & e^{i\phi} \end{pmatrix} \tag{2.21}$$

Referring back to Equation 2.17 this can be recast into the form:

$$\mathbf{V}_{ij} = \mathbf{G}_i \left(\sum_s^{N_c} \mathbf{E}_{si}\mathbf{K}_{si}\mathbf{B}_s\mathbf{K}_{sj}^\dagger\mathbf{E}_{sj}^\dagger \right) \mathbf{G}_j^\dagger \tag{2.22}$$

Importantly if $\mathbf{E}_i = \mathbf{E}_j$ this assumes that the beam to first order is the same for every antenna, which is a reasonable assumption. In reality dipole deformations and rotations mean that the beams are not the same for every antenna or tile. Thus the beam described here is the average beam for each antenna or tile. If there exists a good model of the average beam, as will be discussed in Section 3.3, then the beam correction can occur in the image domain and a new brightness matrix (aptly named the apparent sky by Smirnov (2011a)) can be defined:

$$\mathbf{B}_{\mathrm{app}} = \mathbf{EBE}^\dagger. \tag{2.23}$$

Again recasting Equation 2.17 with this new definition:

$$\mathbf{V}_{ij} = \mathbf{G}_i \left(\sum_s^{N_c} \mathbf{K}_{si}\mathbf{B}_{s,\mathrm{app}}\mathbf{K}_{sj}^\dagger \right) \mathbf{G}_j^\dagger. \tag{2.24}$$

This above equation casts the visibility for a particular baseline projection as the sum of the DDE Jones matrix products with $\mathbf{B}_s$ for each source s. This is then multiplied by the DIE gain matrix terms $\mathbf{G}_i$ and $\mathbf{G}_j^\dagger$. With this formalism, there are of order N unknowns but there are $N(N-1)/2$ baseline measurements for a given array, hence it is possible to estimate the unknown phase and gain quantities using a least squares approach (Sault et al., 1996; Smirnov, 2011b). With this in mind in the next Section we will explore the direction dependent calibration algorithm of the real time system (RTS) implemented by (Mitchell et al., 2008).

2.2.3 Sky-Model Calibration (Mitchcal)

In Mitchell et al. (2008) the visibilities are approximated to be a superposition of N_c point source calibrators that follow a similar formalism to Equation 2.24 with the addition of noise $N_{ij,\nu}$, where importantly the visibilities are defined at the frequency ν of each fine spectral channel:

$$\mathbf{V}_{ij,\nu} = \mathbf{N}_{ij,\nu} + \mathbf{G}_{i,\nu} \left(\sum_s^{N_c} \mathbf{K}_{si,\nu} \mathbf{B}_{s,\nu,\mathrm{app}} \mathbf{K}_{sj,\nu}^\dagger \right) \mathbf{G}_{j,\nu}^\dagger \qquad (2.25)$$

Similar to the previous definition, $\mathbf{K}_{si,\nu}$ contains a phase offset which represents the perturbations as a result of the ionosphere. With this representation of the model visibilities, Mitchell et al. (2008) proposed an iterative calibration algorithm, that implements a peeling based approach and DDE correction. In Mitchell et al. (2008), the algorithm used a bootstrapped model of the Molongolo Reference Catalogue (Large et al., 1981, MRC) as a basis for the sky-model. With the advent of the GLEAM survey, it is now possible to use MWA data for the sky-model. The proposed algorithm follows the process outlined in the next Section.

Calibration Measurement Loop (CML)

> **Ranking:** Calibrator sources are ranked from the most apparently bright to the least using the MWA tile beam model. Due to the different beam shape across the 30.72 MHz bandwidth, the frequency dependence of the beam needs to be taken into consideration.

> **Initial source subtraction:** Using a formalism similar to Equation 2.25 an estimate of the visibilities is made through the summation over all calibrator sources. These estimations are then subtracted in what is referred to as a pre-peeling process to remove as much of the source power as possible. This is done sequentially from the brightest to faintest calibrator source, since the brightest calibrator source is less affected by subtraction errors in contrast to the faintest source.

> **Loop:** The next step is an iterative process which loops through each of the ranked calibrators s, performing the operations $1-4$ in the below sub-list.

>> 1. **Rotate Visibilities and Sum Over Frequency:** The visibility contribution of the ranked calibrator s is added back into the peeled visibility data set. The visibilities are then phase rotated to be centred

on the calibrator s. Visibilities at this stage are also separated into frequency subbands of size M. The visibilities are then summed and averaged in frequency over the subband M. This has the added benefit of eliminating the contributions from other sources as well as reducing the total number of calculations required by the algorithm. By averaging in frequency, this has a two fold benefit. First averaging acts as a directional filter. This effectively separates the signal of interest at the phase centre from the rest of the sky (Rioja et al., 2018). This also reduces the number of calculations necessary in the algorithm, and allows for parallel processing.

2. **Ionospheric Refraction Measurements:** Because the visibilities are dominated by the calibrator s, the Stokes parameters (particularly Stokes I) can be determined. A phase offset is assumed to be applied due to ionospheric effects that perturbs the u and v baseline projections. Applying linearisation constraints a least squares fit is performed to solve for the ionospheric phase ramp. Using these fits the averaged visibilities are phase shifted to the new position.

3. **Instrumental Gain Measurement:** To calibrate the gain solutions, a least squares optimisation approach is used, to find the Jones matrices which minimise the summed visibilities for the calibrator source s.

4. **Source Subtraction:** The ionospheric and gain measurements are then subjected to a goodness of fit threshold. If this is passed then the calibrator source s is fully peeled from the visibility data set. Otherwise initial subtraction is repeated. This process is repeated sequentially for each calibrator in the list.

This method is implemented in parallel for each of the fine channels. This method is implemented in both the RTS and CALIBRATE (Mitchell et al., 2008; Offringa et al., 2016), where the latter is used throughout this thesis to process and calibrate MWA observations at 300 MHz.

2.3   Summary

I aimed to describe the theoretical foundation for interpreting radio astronomy data and science products. In Section 2.1 I described the primary mechanism for radio emission which is synchrotron emission, and the models that can describe the resulting SED's of radio galaxies. These models will be useful in Chapter 4 where I develop the 300 MHz sky model. The SED's of radio sources are constructed from measurements made by radio interferometers, and therefore I then laid out a basic summary of interferometry considering a simple two antenna design. This set up was then formalised in a matrix format which could be used to understand how radio interferometry data can be calibrated.

Chapter 3

MWA Surveys and Instrumentation

In this Chapter I review the MWA as a radio telescope (Section 3.1) as well as the data products of the MWA. In Section 3.2 I discuss the all-sky survey conducted by the MWA. The all-sky survey is of particular importance for this project. It is the first data release of this survey that forms the basis of the 300 MHz sky model I develop in Chapter 4. I also discuss the fully embedded element (FEE) MWA tile beam model in Section 3.3.

3.1 MWA

The MWA is a low-frequency aperture array which is located in the Radio quite zone of the Murchison Radio-astronomy observatory (MRO) (Bowman et al., 2013; Ord et al., 2010). The MWA has been in its second phase (Phase II) configuration since 2016. This configuration consists of 256 tile (stations), as with Phase I only 128 tiles can be recorded and correlated at any one time. Each tile is comprised of 16 dipole bow tie antennas capable of observing the X and Y polarisations (East-West and North-South configurations) in the frequency range 70 to 320 MHz (Wayth et al., 2018). The total frequency range for the Phase 1 (2013-2016) and Phase 2 configurations is split into observing bands with a maximum width of 30.72 MHz. Each of these observing bands is further subdivided into 24 coarse channels of width 1.28 MHz. These coarse channels can be further subdivided into fine channels of 10 kHz, for the GLEAM observations a 10 kHz fine channel width was used[1]. This is the same for the Phase I and Phase II configurations.

3.1.1 MWA Science Goals

The MWA has excellent uv coverage, a wide field of view, and a large fractional bandwidth. These features of the array make the MWA a very flexible scientific instrument, suited for many different applications. Specifically the MWA was designed with four main science goals. The first science goal is the detection of the 21-cm signal from the epoch of reionisation (EoR) (Tingay et al., 2013;

---

[1]these were then averaged down to 40 kHz.

Bowman et al., 2013; Beardsley et al., 2019). The 21-cm signal is the hyperfine spin flip transition line of neutral hydrogen. The EoR is the period of time in the early universe when the first stars, galaxies and quasars began ionising the surrounding neutral hydrogen. The 21-cm EoR signal is expected to lie in the frequency range of 120-200 MHz at a redshift range of 6-10. The second primary goal is galactic and extra-galactic science and the group working in this area are interested in studying radio emission from HII regions in the galaxy, as well as extra-galactic radio galaxies. The important scientific output from this group is the all-sky survey, this will be further discussed in Section 3.2, and is a key component to the work in this thesis. The third primary goal is related to time domain science. This includes studying transient objects, and other phenomena such as pulsars and fast radio burst. The last science goal is related to studying the ionosphere, solar activity and the heliosphere.

3.2   The Galactic and Extra-galactic All-sky MWA Survey

The GLEAM survey was conducted by the MWA covering the southern sky declinations below +30 deg (Wayth et al., 2015). This survey observed the southern radio sky in the frequency range of $72 - 231$ MHz. This frequency range was split into five observing bands of 30.72 MHz bandwidth. Each of these observing bands was further split into subbands of spectral resolution 8 MHz. The GLEAM survey utilised a meridian drift strategy to reduce the number of different primary beam patterns needed to image and calibrate MWA data. This required that the survey be split into seven declination strips, each with five corresponding frequency ranges. The declination strips where chosen so that the full width half maximum (FWHM) of the primary beam overlapped with the peak of the next declination strip. The observations were broken into two minute intervals for each of the five frequency bands, of which approximately 108 seconds of data was useable. A calibration field was also observed for 10 minutes using the same two minute snapshots for each frequency band. Every two hours a bright calibrator source was observed, during observations where the ionosphere was relatively stable. Phase and amplitude calibration solutions were assumed to be transferable between pointings, reducing the overall amount of initial calibration required for the survey.

As mentioned in Section 3.1.1 the GLEAM survey is one of the main scientific products of the galactic and extra-galactic research of the MWA. The primary science goal of the survey was to study radio galaxies and active galactic nuclei. Additional science goals involve studying supernova remnants in the galactic plane; studying the radio emission from galaxy clusters; and mapping the Large and Small Magallenic clouds (Wayth et al., 2015).

3.2.1   GLEAM Year 1 Extra-Galactic Data Release

The GLEAM year 1 extra-galactic first data release (Hurley-Walker et al., 2017) from hereon GLEAM_exGal, covered 24,831 square degrees of sky, extending down for all declinations south of +30 deg. In total there were 20 subbands

for the entire survey, of which $307,455$ radio sources were detected. The first data release is missing some key regions from the southern sky; the region within $10\,\mathrm{deg}$ around the galactic plane (GP); the Large and Small Magallenic clouds (LMC,SMC); Centaurus A (Cen A) and a wedge region which was the sidelobe reflection of Cen A; and an additional wedge region that had particularly bad ionospheric conditions. The regions are all missing for different reasons; the GP, the LMC, and the SMC contain diffuse emission which makes processing the data more difficult. These regions were processed and released in later papers (Hurley-Walker et al., 2019; For et al., 2018), this will be discussed more in Chapter 4.

The image processing performed for the GLEAM_exGal observations produced 20 images; one for each of the subbands. In Hurley-Walker et al. (2017) they aimed to construct the most sensitive image by combining these images together. The combination of images started with the highest resolution image, continuing down until the noise of the stacked images no longer decreased. The combined images were convolved to have the same resolution. The resulting most sensitive image covered the frequency range $170 - 231\,\mathrm{MHz}$ with a central frequency of $200\,\mathrm{MHz}$. This image had an approximate resolution of 2 arcminutes.

The source finder AEGEAN was then applied to the wide-band image to create an initial reference catalogue (Hancock et al., 2012; Hurley-Walker et al., 2017). The initial catalogue could then be used as a basis for source finding the 20 subband images through a process known as priorised fitting (Hancock et al., 2018). This process uses the base catalogue to determine the position of sources in the subband catalogues and hence perform flux density measurements. The result of this is a catalogue which covers the 20 subbands for all $307,455$ sources. This catalogue is 90% complete down to $170\,\mathrm{mJy}$ at $200\,\mathrm{MHz}$.

The output catalogue from this work was used as the basis for the $300\,\mathrm{MHz}$ sky model I develop in Chapter 4.

3.3   MWA Tile Beam Model

As discussed in Section 2.2.2 the tile beam is assumed to be the same for each antenna. This is an important consideration, because with a good tile beam model it is possible to apply beam corrections in the imaging plane. In the following Section the current MWA tile beam model will be discussed, as well as the background behind its development.

3.3.1   FEE Model

In the original design of the MWA,Ord et al. (2010) modelled the tile beam analytically by assuming each dipole could be represented by a Hertzian dipole. A Hertzian dipole represents a differential radiating element which is small enough that it can be assumed that a constant current is applied across the dipole. This is a valid approximation at low frequencies when the wavelength of the observed radiation is larger than the dipole size, but at higher frequencies this approximation breaks down (Sutinjo et al., 2015). Additionally this original model did not account for the mutual coupling between dipole elements within the tile. Mutual coupling is when neighbouring dipoles excite each other, this occurs because
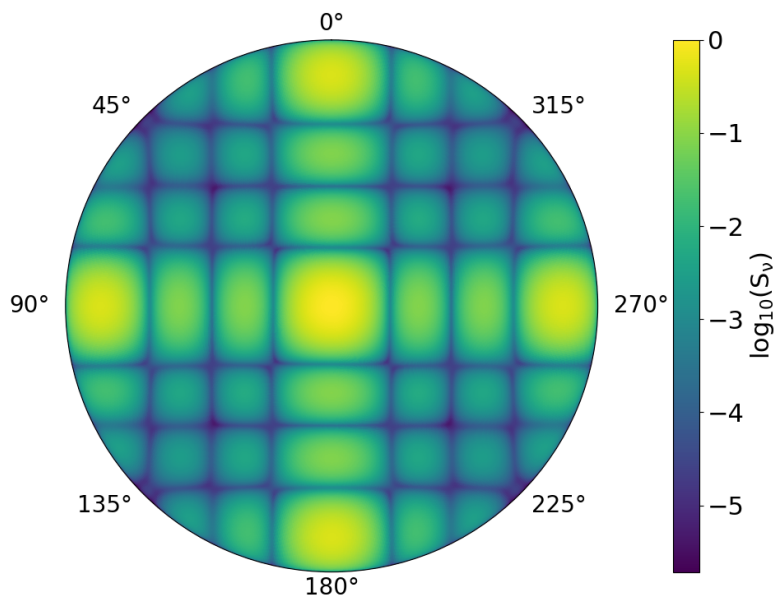
Figure 3.1: The logarithmic $300\,\mathrm{MHz}$ MWA tile primary beam model for a zenith pointing. Here the grating sidelobes are apparent. The orthographic beam projection was created using the MWA 2016 FEE beam model.

dipoles can also emit as well as receive radiation. Without accounting for this effect polarisation leakage in the linear Q polarisation was noted, which at some declinations and high frequencies reached values of 30% (Sutinjo et al., 2015). As such this motivated the development of a new beam model that could account for these effects and thus reduce the observed polarisation leakage.

Motivated by the need for a more physical representation of the MWA tile beam model Sutinjo et al. (2015) proposed the FEE model to account for the mutual coupling that occurs between dipoles. By considering reciprocity antennas can emit as well as receive radiation. Thus to model the sensitivity pattern for the embedded element pattern, each of the 16 different dipoles and their two orthogonal polarisations were independently simulated whilst the rest were left in an open circuit configuration. This takes into account the mutual excitation of the remaining inactive dipoles. In Sokolowski et al. (2017) the FEE model is recast using spherical waves. This improves upon the previous work of Sutinjo et al. (2015) since it is framed in terms of spherical basis functions, hence the beam can be determined at any (θ, ϕ) value, it also takes into account the frequency and pointing angle. This new model significantly reduced the Stokes Q leakage into Stokes I, but does not account for all of it. The FEE beam model presented in Sokolowski et al. (2017) will be referred to as BEAM2016 model.

An example of the BEAM2016 for a zenith pointing at $300\,\mathrm{MHz}$ can be seen in Figure 3.1. This figure shows the embedded element pattern which is characteristic of the MWA tile beam. It also shows the grating sidelobes which are reflections of the main lobe towards the horizon. Typically only the main lobe is of interest in the calibration process, but these grating lobes are a necessary consideration when processing MWA data at $300\,\mathrm{MHz}$. Without the beam model

these grating lobes would make calibrating MWA observation at 300 MHz very difficult.

3.4 Summary

In this Chapter I have summarised the data and the instrument which I use in this project. Additionally without GLEAM_exGal and the FEE MWA tile beam model the rest of the project would not be possible. In the next Chapter I describe the construction of the 300 MHz sky-model from low and high frequency catalogues that have been cross-matched together. The BEAM2016 model can then be used in conjunction with a 300 MHz sky model to construct an apparent sky model for a particular observation. This apparent sky model can then be used with the calibration process described in Chapter 2 to calibrate MWA observations at 300 MHz.

Chapter 4

300 MHz Sky Model

In Chapter 2 the groundwork for sky-model calibration was laid out. To review, sky model calibration is where an apparent model of the sky can be used to predict the visibilities of an observation. These predictions can then be used to calibrate the instrumental effects such as gain and phase offsets through least-squares estimation. This Chapter will focus on the construction of a total sky-model which can be used as a basis for constructing an apparent sky model. The 2016 MWA tile beam, the apparent sky and subsequent data calibration will be the focus of Chapter 5.

To construct this total sky-model, a natural choice for a base catalogue is the GLEAM_exGal catalogue, which can be cross-matched with higher frequency catalogues to cover a larger range of the radio spectrum. The GLEAM_exGal catalogue as mentioned in Chapter 3 covers the frequency range $72 - 231\,\mathrm{MHz}$ (Hurley-Walker et al., 2017). Section 4.1 covers the work by J. Line to create a high and low frequency catalogue with GLEAM_exGal as its base. This catalogue is used in work to interpolate the flux density at 300 MHz, and thus construct the 300 MHz sky-model.

This Chapter is composed of the following Sections; Section 4.1 relates to the cross-matched GLEAM_exGal catalogue with higher frequency catalogues, and the modelling used to estimate the 300 MHz flux density; Section 4.2 is about the TGSS/NVSS catalogue which is used to fill in missing regions in the GLEAM_exGal catalogue, as well as the 300 MHz flux density estimation; Section 4.3 follows the GLEAM-X sky-model which is used to fill in the remaining missing regions of the GLEAM_exGal catalogue. GLEAM-X is an ongoing MWA survey which covers the entire sky south of DEC $+30\,\mathrm{deg}$, this survey uses the extended baseline configuration of the MWA (Wayth et al., 2018). Section 4.4 describes the exceptionally bright "A-team sources"[1], and their addition to the sky model; and finally Section 4.5 describes the total sky-model as well as some of the statistics and analysis of the model.

---

[1]This is a colloquial definition for a set of the brightest apparent radio galaxies. These sources can be identified by the capital A at the end of their name. Examples include Centarus A, Pictor A, Cygnus A, and Fornax A.

4.1   Positional Update and Matching Algorithm (PUMA)

For this work a catalogue that contains the a high low frequency spectral range was needed to interpolate the sky flux density at 300 MHz. The catalogue used in this work uses the GLEAM_exGal catalogue as a base catalogue cross-matched to other high frequency catalogues (J. Line, personal communication). Cross-matching different surveys from different instruments can be a challenging task, since different instruments have different resolutions, sensitivities and systematics which affect the data output. This in particular motivated the creation of the cross-matching algorithm PUMA by Line et al. (2017).

The algorithm uses a two tier approach when identifying possible cross-matches. The first approach is a Bayesian probabilistic positional cross-match, and the second approach takes into consideration the spectral information. The method is designed to reliably create all-sky catalogues from low and high frequency information for the purpose of calibrating low frequency radio observations, particularly with the MWA (Line et al., 2017). Broadly, the algorithm cross-matches the base catalogue (typically the catalogue with the lowest angular resolution), via angular position with the other input catalogues. An example base catalogue is GLEAM_exGal. It keeps all possible matches with the base source from each catalogue. Where possible matches are defined by a user-designated angular separation. The algorithm then calculates the posterior probability that the base catalogue source is a match with every other cross-matched source. The posterior probability considers the angular position and the corresponding error for the base source, as well as the density of sources in each of the matched catalogues. It then applies spectral as well as positional criteria to each base source to identify the best possible cross-match. Match types are classified into four main classes:

`isolated`: This class of source only has one cross-match. These are accepted if the spectral data for the possible matches fits to a power law to within some specified threshold, or if the posterior probability is above some user defined threshold.

`dominant`: These are sources where multiple potential positional cross-matches exist with the base source. In this case the power law was fitted for each combination. If the residuals for a particular combination were lower than the rest of the fits by some significance threshold, then the source was classed as dominant.

`multiple`: The `multiple` case occurs when a source is unresolved in the base catalogue, which typically has a lower resolution than the other cross-matched catalogues. These unresolved sources can include multi-component sources such as double lobed radio galaxies. In the higher resolution cross-matched catalogues the lobes may be resolved. This therefore leads to multiple cross-matches with the base catalogue. If there is no dominant source, the multiple matches are combined into a single weighted source and are then fitted to a power law with the base catalogue source. If the fit is acceptable then the new weighted combined source is accepted otherwise the match is flagged as `eyeball`.

`eyeball`: This class of source is when `multiple` is flagged for visual inspection.

Using PUMA (J. Line, personal communication) created an all-sky low and high frequency catalogue with GLEAM_exGal as the base catalogue. A version of this catalogue forms the central part of the 300 MHz sky-model in this work, and is hereon referred to as the PUMAcat. The next Subsection 4.1.1 explores the details of this catalogue.

4.1.1 PUMA Catalogue

PUMAcat was created by cross-matching the GLEAM_exGal catalogue with the following list of surveys: the 74 MHz Very Large Array Low Frequency Sky Survey redux (Lane et al., 2014, VLSSr); the GMRT 150 MHz all sky radio survey (Intema, H. T. et al., 2017, TGSS); the 843 MHz Sydney University Molonglo Sky Survey (Bock et al., 1999, SUMSS); the 1.4 GHz NRAO VLA Sky Survey (Condon et al., 1998, NVSS) (J. Line, personal communication). PUMAcat covers the same areas of the sky as the base GLEAM_exGal catalogue.

Overall PUMAcat contains $308,584$ radio sources and covers a frequency range of 72 MHz to 1.4 GHz, including (where possible) the full GLEAM bands from 76 MHz to 227 MHz[2]. In this catalogue $257,583$ sources were identified as `isolated`, $33,783$ were identified as `multiple`, $4,753$ were identified as `dominant` as per Line et al. (2017) and described in Section 4.1. The remaining sources were split into several other additional class definitions not defined in Line et al. (2017). These classes include $5,203$ sources defined as `N/A`; these are GLEAM_exGal sources which did not have any corresponding matches in the other catalogues. The 783 sources designated `Aegean` come from a field centred at $RA = 0 \, \text{deg}$, $DEC = -37 \, \text{deg}$. These sources originate from a special run of AEGEAN and were not included in the original GLEAM_exGal catalogue (P. Hancock, personal communication).

The last class of sources are the $6,460$ sources classified as `Pietro`. These sources are derived from the sky-model described in Procopio et al. (2017). This sky-model was created to process over six hours of MWA observations for one of the MWA EoR survey fields (EoR1, centred at $RA = 60 \, \text{deg}$, and $DEC = -30 \, \text{deg}$). In Procopio et al. (2017) they used PUMA to cross-match GLEAM_exGal with reprocessed TGSS images of the EoR1 field, along with the other higher frequency catalogues mentioned above. These sources were then fit with second order polylogarithmic models to ensure smooth spectral behaviour across the 182 MHz MWA EoR band. As a result in PUMAcat these sources only have spectral values for the frequencies 170 MHz, 190 MHz and 210 MHz. These values were chosen in particular for calibration purposes, they capture the end and middle parts of the EoR 182 MHz band. Since these are fit values, in PUMAcat they do not have any quoted errors, the estimation of these errors will be discussed in the following Subsection 4.1.2.

---

[2]These frequencies are the central subband frequencies.
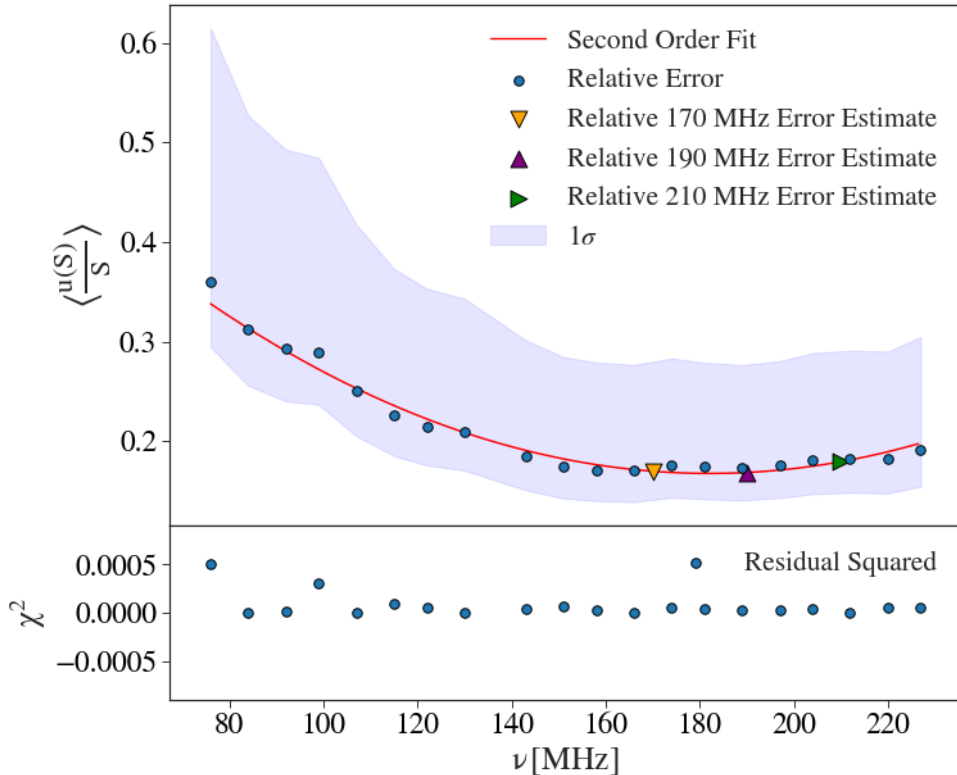
Figure 4.1: The top panel plots the median relative error in each of the MWA subbands against their respective frequency in MHz. Those data points are represented by the enclosed blue circles. The best fit second order polynomial is the solid red line, and the 1σ region is shown in the blue shaded region. The estimated relative errors for the 170 MHz, 190 MHz and 210 MHz are given by the yellow downwards triangle, the purple upright triangle and green sideways triangle respectively. The bottom panel shows the squared residuals given by χ^2 of the model compared to the relative errors.

4.1.2 Filtering & Processing

Before I could use PUMAcat to determine an estimate of the 300 MHz sky, it needed to be filtered and processed to eliminate potential outlier sources. Primarily I found there were 20 sources which had either no flux density measurements or had only one flux density measurement. I simply filtered these sources from PUMAcat. Other potential problems arise from the previously mentioned `Pietro` sources, which as mentioned do not have errors for their flux densities.

To estimate the errors for the `Pietro` sources I determined the average relative error for each of the 20 MWA bands. I calculated the statistical deviation in the average relative error $\langle u(S)/S \rangle$ by using the inter-quartile range (IQR) to estimate the standard deviation. For skewed distributions this is a more robust method for characterising the standard deviation of the sample. In this case I approximated the standard deviation as $\sigma \approx \text{IQR}/1.35$ (Higgins & Green, 2008). I then fitted the resulting average relative error and the 1σ error range with increasing orders of polynomials using the PYTHON2.7 package NUMPY class POLYFIT. This is shown in Figure 4.1.

ν [MHz]	$\langle u(S)/S \rangle$
170	0.17
190	0.17
210	0.18

Table 4.1: The estimated relative errors calculated in the fitted flux density sub-bands for the `Pietro` sources found in (Procopio et al., 2017).

Bayseian Information Criterion

I determined the best fitting polynomial by using the Bayesian information criterion (BIC) defined below (Schwarz, 1978):

$$\text{BIC} = \ln(n)k - 2\ln(\widehat{L}(\widehat{\theta})). \tag{4.1}$$

The BIC represents two components. The first component $\ln(n)k$ penalises models that overfit the data, where k is the number of parameters for a model, and n is the number of data points in the sample. In this case, the model is a polynomial $k = \text{order} + 1$. The second component is the natural log of the maximised likelihood function $\widehat{L}$. or a statistical distribution of data, the likelihood is a measure of how well the model for a given set of arbitrary parameters $\vec{\theta}$ fits the sample data. The set of parameters $\widehat{\theta}$ that maximises the likelihood is the best representation of the model fit to the data. In the special case where the likelihood function can be described by a Gaussian distribution, the BIC reduces to a simpler form given below:

$$\text{BIC} = \chi^2 + \ln(n)k. \tag{4.2}$$

χ^2 represents the sum of the square residuals, given by:

$$\chi^2 = \sum_{i=0}^{n} \frac{\left(f(\vec{\theta}|x_i) - y_{\text{data}}\right)^2}{\sigma^2}. \tag{4.3}$$

Here, $f(\vec{\theta}|x_i)$ is the model as a function of the vector of polynomial coefficients $\vec{\theta}$, and the ith MWA frequency band x_i. y_{data} is the measured or observed data, which is the average relative error in each subband, and σ is the standard deviation for that subband.

Determining the Best Fit

Using Equation 4.2 I found a second order polynomial had the minimum BIC value, and thus is the best fit to the data. I then used the fitted second-order polynomial to estimate the mean relative error in the three fitted bands 170 MHz, 190 MHz, and 210 MHz from (Procopio et al., 2017). The estimated errors to two significant figures can be found in Table 4.1.

I then multiplied the relative errors by the flux densities for all `Pietro` sources to determine estimates on their error. This step was necessary otherwise the model fitting in the following Section would not work. I additionally applied

this method to the other MWA subbands for sources that similarly had no error estimates for their flux densities, or had flux densities of -1. The origin of the negative values comes from the source fitting algorithm AEGEAN used to source find the GLEAM_exGal survey (Hancock et al., 2012; Hurley-Walker et al., 2017; Hancock et al., 2018). The value of -1 is assigned when AEGEAN fails to correctly estimate the flux density errors. This could be due to uncertainties in the position or other variables being above the upper limit threshold (Hancock et al., 2012; Hancock et al., 2018). For the purposes of this work these fit errors were replaced by the best estimates derived from the polynomial fit to the mean relative error.

4.1.3   SED Modelling

With the comprehensive PUMAcat data that covers the frequency range of 72 MHz to 1400 MHz across most of the sky, it is now possible to interpolate (and in cases where high frequency data does not exist, extrapolate) the flux density at 300 MHz. To model and hence estimate the flux density I considered two simple models which I discussed in Section 2.1. The first model I consider in this thesis is the power law model, which is well grounded in the literature (Kardashev, 1962). The second model I consider for this work is a second order polylogarithmic function. This is not an analytical model, but has been shown to be a useful model, fit to radio sources with peaks in their spectra (Blundell et al., 1999; Duffy & Blundell, 2012; Callingham et al., 2017; Harvey et al., 2018).

Fitting the Models

Using Equations 2.1 and 2.2, the SED's of radio sources with four or more data points could be fit to estimate the flux density at the reference frequency $\nu_0 = 300$ MHz. I used the PYTHON function POLYFIT from the package NUMPY to fit the data. This function is well suited to performing the fit. It determines the fit coefficients by minimising the χ^2 value as defined in Equation 4.3. This is easier with polynomials since the Jacobian matrix for polynomials is readily and analytically determined, thus numerical estimation is not necessary. This provides a faster and more accurate least-squares fit to the data. Additionally the data are fitted in log-space not in normal-space. This is a sensible choice because the flux densities of radio sources can vary by orders of magnitude over relatively small frequency ranges. Thus fitting SEDs in log-space provides a more numerically stable approach to modelling the flux density at 300 MHz. For this assumption to work the errors in log-space have to be assumed to be approximately Gaussian, which is not necessarily true. The derivation of the approximate errors can be found in Section B.3 of the Appendix. As I mentioned in Subsection 4.1.2 the BIC (Equation 4.2) can be used to discriminate between model fits.

The change in the BIC (ΔBIC) value is a significance threshold which in a sense compares the log maximum likelihoods for two models fitted to the same data set. In Kass & Raftery (1995) value ranges of significance for this threshold are given. These different significance levels suggest evidence in favour of the model with the lower BIC. Model comparisons with ΔBIC < 2 show very weak evidence for being a preferential fit to the data, $2 < \Delta$BIC < 6 shows weak evidence of a preferential fit, and $6 > \Delta$BIC > 10 shows strong evidence for being
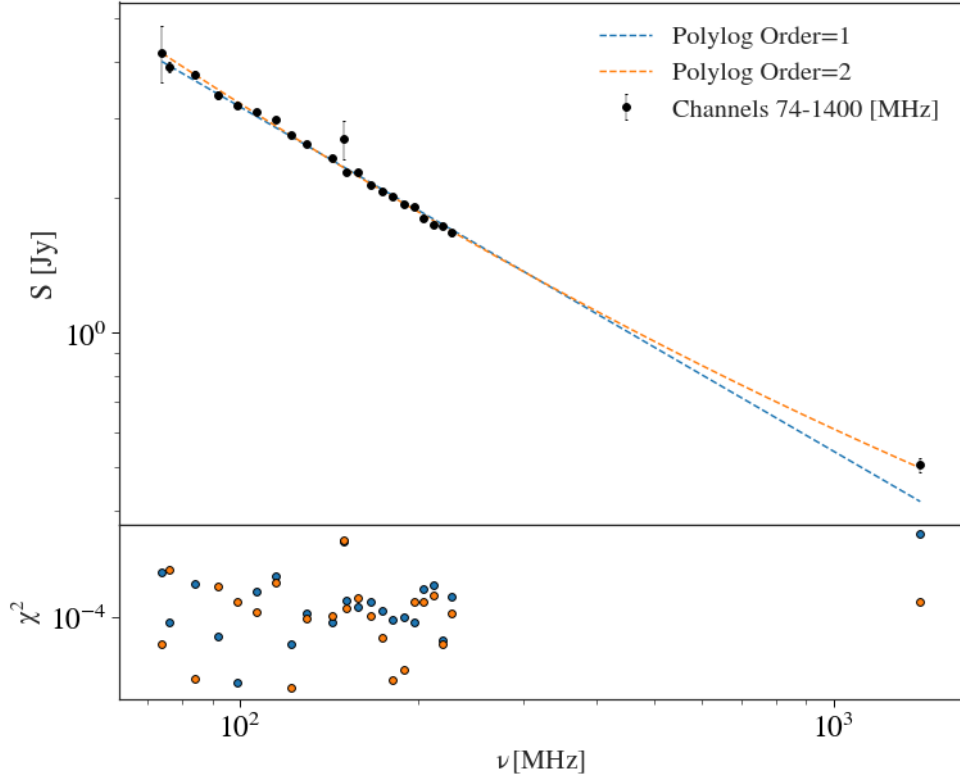
Figure 4.2: Log-log plot of the SED of an arbitrary source taken from PUMAcat. In the top subfigure the black circles are the flux densities as a function of the normalised frequency, where the normalisation frequency ν_0 is defined at $300\,\mathrm{MHz}$. The error bars for most of these points are too small to be seen. The dashed blue line is the power law fit to the SED (also first order polylogarithmic fit), the dashed orange line is the second order polylogarithmic fit to the SED. The bottom subfigure shows the residuals χ^2 for both fits as a function of normalised frequency, where the colours correspond to the model in the top subfigure. For this particular source a power law fit was found to be preferable.

preferential fits to the data. In this thesis I look at the difference of the second order polylogarithmic BIC compared to the power law BIC. For a second order polylogarithmic function to be accepted over a power law fit, my fitting requires that the ΔBIC > 6. If this threshold is not met then the power law model is selected as the default model. It should be noted that higher order polylogarithmic functions were not fitted to the radio SEDs of sources in PUMAcat. The gap in the frequency sampling of these sources can be large. As a result of this when fitting higher order polylogarithmic functions, inflections with positive and negative curvature are common in between the low and high frequency samples. This leads to significant over estimates and under estimates in the $300\,\mathrm{MHz}$ flux density.

Examples of fits from Equations 2.1 and 2.2 can be found in Figures 4.2 and 4.3. Figure 4.2 shows the case where a power law fit is preferable to a second order polylogarithmic fit, Figure 4.3 shows the case where there is significant curvature in the spectrum and a second order polylogarithmic fit is preferable. After applying the fitting process to all the sources in PUMAcat, $267,542$ of
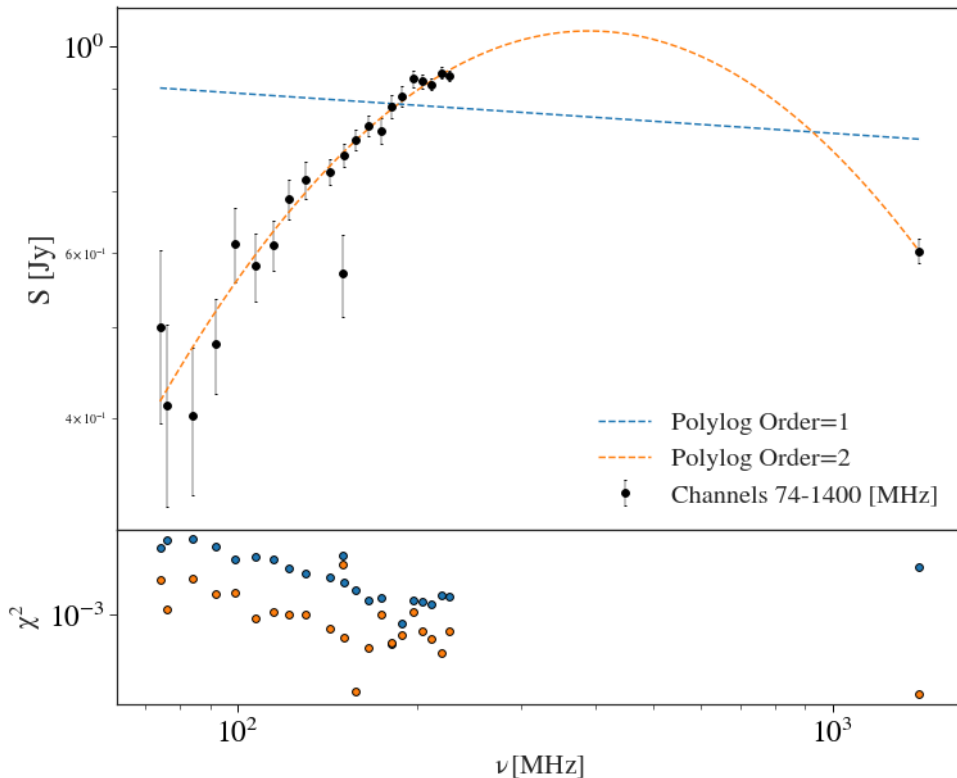
Figure 4.3: Log-log plot of the SED of an arbitrary sources taken from PUMAcat. In the top subfigure the black circles are the flux densities as a function of the normalised frequency, where the normalisation frequency ν_0 is defined at 300 MHz. The dashed blue line is the power law fit to the SED (also first order polylogarithmic fit), the dashed orange line is the second order polylogarithmic fit to the SED. The bottom subfigure shows the residuals χ^2 for both fits as a function of normalised frequency, where the colours correspond to the model in the top subfigure. For this particular source a second order polylogarithmic fit was found to be preferable.

them were found to have a preferred power law fit. The remaining $41,022$ sources were found to have a preferred second order polylogarithmic fit; these sources constitute $\sim 13\%$ of PUMAcat. The PYTHON script `Sky_model.py`[3] was written to perform the filtering and fitting for PUMAcat. The script was designed to be sufficiently general enough to accept any arbitrary reference frequency ν_0, so it should be able to generate any sky-model in the frequency range of $72-1400$ MHz. This is an important result because the script can be used to construct sky-models for the majority of the southern radio sky at any radio frequency in the range $72-1400$ MHz. This may be a useful tool for future science applications for the MWA and other radio telescopes such as MeerKAT or ASKAP which have bands in the 72-1400 MHz frequency range. The new fitted PUMAcat sky-model at 300 MHz will from hereon be referred to as the PUMA300 catalogue, or PUMA300 sky-model.

The PUMA300 sky-model covers a large portion of the sky, but like the GLEAM_exGal catalogue it is missing higher declination regions, the galactic

---

[3]The script is available with the rest of the scripts used in this work, at the following GitHub repository S300-PIPELINE (https://github.com/JaidenCook/300-MHz-Pipeline-Scripts)

plane, the SMC and the LMC, as well as two wedge regions. The next Section introduces the method and data used to cover some of these missing regions, specifically the higher declinations and the two wedge regions.

4.2 TGSS/NVSS Spectral Index Catalogue

The TGSS/NVSS spectral index catalogue (de Gasperin et al., 2018) is a cross-matched catalogue between the TGSS (Intema, H. T. et al., 2017) and NVSS surveys (Condon et al., 1998). This new high and low frequency catalogue covers a frequency range of 147 MHz to 1.4 GHz. TGSS and NVSS were chosen by de Gasperin et al. (2018) due to their similar angular resolution and large frequency range. The surveys have an overlap region covering approximately 80% of the sky from $DEC \in [-40, 90]$ deg. Additionally these two surveys are the most flux sensitive within their respective frequency regimes. The motivation behind creating this catalogue, was to explore and therefore analyse the global spectral index distribution for radio sources. In particular the spectral index is a useful metric for classifying radio sources (van der Laan, 1966). In total the TGSS/NVSS catalogue contains more than 1.4 million radio sources and covers areas of the sky previously missed by PUMAcat.

de Gasperin et al. (2018) classified cross-matched sources in the TGSS/NVSS catalogue into six different classes. The classification is derived from the method of cross-matching which involved re-processing TGSS images to match the NVSS images which have a lower $45''$ angular resolution. A source finding algorithm was then applied to both the mosiaced TGSS and NVSS images. This process involved splitting the images into island masks, which were individually fitted with Gaussians to determine the σ_{rms}, as well as the number of sources per island. The resulting source catalogues from TGSS and NVSS were then cross-matched with an angular separation of $15''$, where the matches were classified into the following definitions:

single (S): A single match where there is only an isolated source in both the TGSS and NVSS islands.

multiple (M): Islands with multiple matched sources. Multiple matches for a single island can occur in the case for double lobed radio galaxies.

complex (C): Multiple sources in one island, but only one match. For example this could be the result of a double lobed radio galaxy where one of the lobes may be too faint to be detected in one of the catalogues.

upper limit (U): Detected only in TGSS.

lower limit (L): Detected only in NVSS.

island (I): Island is composed of either matched, unmatched or both types of sources. In this case the global flux density value for the island is saved and constitutes a separate entry in the catalogue. For example (C) sources always have a corresponding island entry.

Region	RA Range [deg]	DEC Range [deg]	N
Wedge 1	$[196, 209]$	$[20, 30]$	$1,779$
Wedge 2	$[320, 360]$	$[0, 30]$	$13,408$
$DEC \in [30, 45]$	$[0, 360]$	$[30, 45]$	$60,729$

Table 4.2: Shows the breakdown of the final number of sources in the two wedge regions, and the declination strip from $30 \deg < \mathrm{DEC} \leq 45 \deg$.

Due to the large sky coverage, frequency coverage, and the sensitivity of the TGSS/NVSS spectral index catalogue, it makes a useful substitute for the parts of the sky that are missing in the PUMA300 sky-model. The next Section outlines the TGSS/NVSS sub-sample used to complete some missing regions of the sky.

4.2.1   Filtering Process

Since the PUMA300 sky-model only extends up to a declination of $+30 \deg$, the TGSS/NVSS catalogue is ideally suited to fill-in the higher declination regions of the sky. In addition, the TGSS/NVSS catalogue can be used to fill in the missing wedge regions in the GLEAM_exGal/PUMAcat catalogues mentioned in Section 3.2.1.

TGSS/NVSS Subset Catalogue

I split the TGSS/NVSS catalogue into three subsets using the astronomy software package TOPCAT (Taylor, 2005). The breakdown of the number of sources and the right ascension (RA) and DEC ranges of each subset can be found in Table 4.2. Two of the three subsets in particular are substitutes for the two missing wedge regions in the PUMA300 sky-model. The third subset covers the declination range of $30 \deg \leq \mathrm{DEC} \leq 45 \deg$ which is also missing from the PUMA300 sky-model. Once the subsets were created they were concatenated together into a single table. Since there is a possibility of double detections with sources classified as (I), I performed an internal cross match to group sources by their island ID. I discarded sources classified as (I) which had corresponding island ID matches with other sources in the catalogue. Additionally sources with only an upper limit (U) or lower limit (L) detection were discarded. These sources had unreliable spectral indices and were too faint for this project.

With the new sub-sample of TGSS/NVSS defined for the aforementioned three regions, the next step I performed was to calculate the flux density at 300 MHz. This is a relatively straightforward power law, where the spectral index for each source is defined in the TGSS/NVSS catalogue:

$$S_{300} = S_{NVSS} \left(\frac{300}{1400} \right)^{\alpha} \tag{4.4}$$

In Equation 4.4 the reference frequency is 1400 MHz and the reference flux density is the NVSS flux density for that particular source. This is then scaled to 300 MHz to derive the flux density estimate at 300 MHz for the same source. The
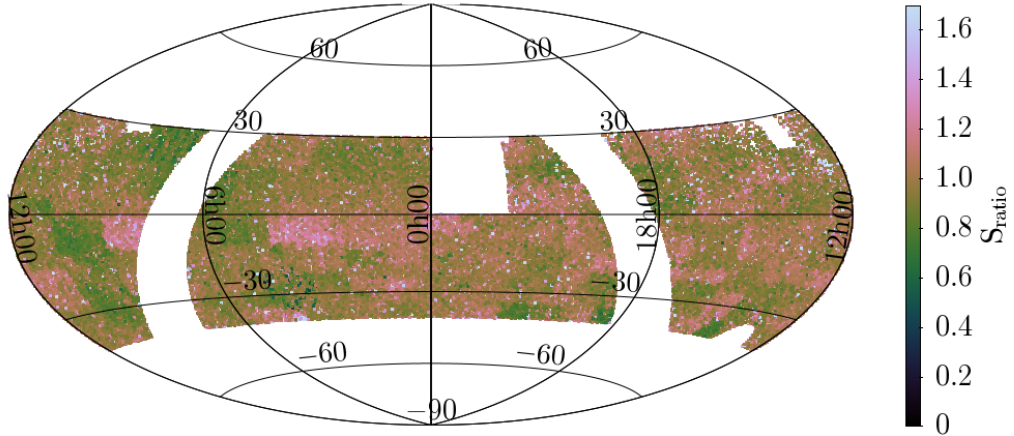
Figure 4.4: Shows the cross-matched PUMA300 catalogue with the TGSS/NVSS catalogue. The auxiliary axis shows the natural log ratio of the flux densities from both catalogues at 300 MHz. This has been truncated to a log ratio value of 1.7 to better accentuate the visual contrast of the figure. The log-ratio of the flux densities appears to be dominated by random noise, with visible deviations in RA and DEC patches that have average values less than the apparent global average. These are likely due to systematic effects present in the mosaiced images in either the GLEAM, NVSS, or TGSS surveys.

new TGSS/NVSS 300 MHz catalogue is hereon referred to as the TGSS/NVSS300 sky-model or catalogue.

One of the downsides to using the TGSS/NVSS300 sky-model to fill in these regions, is that because there is only two data points, the estimate at 300 MHz is less likely to be as reliable as the PUMA300 fits. As a result of this a different catalogue is used to fill in the GP, SMC, LMC and Cen A regions missing from the PUMA300 sky-model. This will be discussed in Section 4.3.

4.2.2   Adjusting the Flux Scale

There is an important consideration to be made when including the TGSS/NVSS300 sky-model with the PUMA300 sky-model. The flux density scales for MWA are not necessarily the same for TGSS or NVSS due to systematics arising from varying instrumental and survey related effects. These differences can vary as a function of RA and DEC which can make them non-trivial to correct. These systematics can be visually identified by looking at the ratio of the 300 MHz flux density in regions overlapping the PUMA300 sky-model and the TGSS/NVSS catalogue (the regions not in the TGSS/NVSS 300 sky-model). In the overlapping regions only sources classified as singles (S) in TGSS/NVSS were considered. These are point sources in TGSS/NVSS hence they would be point sources in PUMA300 due to the lower resolution of the MWA. I then cross-matched the PUMA300 sky-model and the TGSS/NVSS catalogue with an angular resolution of two arcminutes, this yielded 176,073 matches. I then computed the ratio of the 300 MHz flux densities of the cross-matched subset. Figure 4.4 shows the PUMA300 to TGSS/NVSS 300 MHz flux density ratio where the scale range has been restricted to a range of $S_{\mathrm{ratio}} \in [0, 1.7]$. In Figure 4.4 there is clearly an emergent chequered pattern, which varies as a function of both RA and DEC.
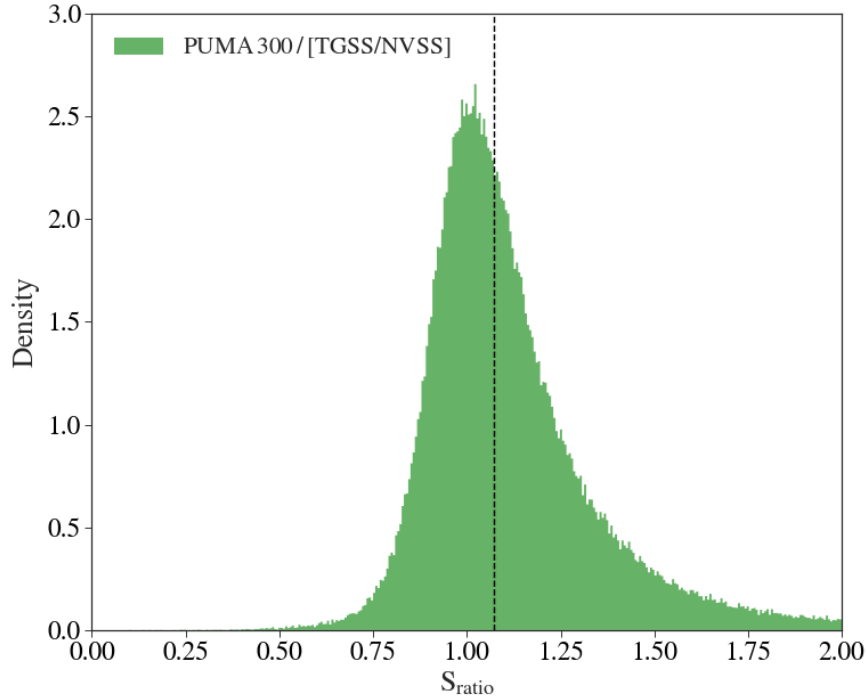
Figure 4.5: The histogram of the ratio of the PUMA300 300 MHz flux density to the TGSS/NVSS 300 MHz flux density in the overlapping regions. The histogram is almost Gaussian with a slight skew towards higher ratio values.

The pattern could potentially be a result of mosiacs or primary beam errors in either the GLEAM_exGal or TGSS surveys. It is important to note that this effect is known in the MWA and GMRT communities, where similar maps at 150 MHz have been made comparing GLEAM_exGal and TGSS (Hurley-Walker, 2017).

Globally there is a median offset of $\langle S_{\mathrm{ratio}} \rangle = 1.07$ for the flux density ratio with the PUMA300 catalogue biasing higher. The distribution of flux density ratios can be seen in Figure 4.5 where the median is represented by the dashed black line. This flux ratio distribution shows considerable skewness towards higher ratio values. This skewness is characteristic of an offset Cauchy distribution[4], which is defined by taking the ratio of two Gaussian distributions with non-zero means[5]. A simple correction of the flux scale in this case is to scale the flux density of TGSS/NVSS sources in the missing wedge regions, and higher declination regions by the global median flux density ratio. This method was preferable over more complicated methods involving fitting functions of RA and DEC, since it is difficult to extrapolate the flux ratio beyond the global average since the higher order effects appear to be random. In this work I scaled the TGSS/NVSS fluxes to the MWA flux scale since this project is concerned with processing and imaging MWA observations, where the data should be on a similar scale. This work does not further concern itself with the correctness of either the TGSS or MWA flux scales.

---

[4]Also known as the Lorentz distribution.

[5]A similar skewness is present in offset t-distributions

4.3 GLEAM Supplementary Catalogue

As previously mentioned the GLEAM survey covered the whole sky south of +30 deg, where the GLEAM_exGal data release did not contain the GP, several wedge regions, the LMC, the SMC and a large region around Cen A. The GP observations were later processed and published by Hurley-Walker et al. (2019), where a similar data reduction and processing method as Hurley-Walker et al. (2017) was applied. Hurley-Walker et al. (2019) found a median spectral index of $\langle \alpha \rangle = -0.83$ for the population of sources. The SMC and LMC data was processed and released by For et al. (2018), where they investigated the spectral curvature of the SMC and LMC by fitting second order polylogarithmic functions at a reference frequency of $\nu_0 = 200\,\mathrm{MHz}$.

The GLEAM-X survey is a follow up all-sky survey covering the same sky as the GLEAM survey (Hurley-Walker, 2019). The data reduction pipeline for GLEAM-X is available at the github repository GLEAM-X-Pipeline[6]. This repository contains a sky-model created from the GLEAM survey which is used to process the GLEAM-X observations. Importantly this sky model covers the missing regions included by For et al. (2018); Hurley-Walker et al. (2019). This sky model also contains extended 2D Gaussian models for Cen A, and point source models for the surrounding regions. It should be noted that the extended models of the Cen A do not capture the complex small scale spatial structure of Cen A as seen by McKinley et al. (2017). The only missing regions in this model are the wedge regions defined in Table 4.2 which in the Section 4.2 were substituted for by the TGSS/NVSS300 catalogue. Similar to the second order polylogarithmic fits applied in For et al. (2018) this sky model also fits for curvature, with a reference frequency of $\nu_0 = 200\,\mathrm{MHz}$. This sky model also contains extended Gaussian component models of the A-team sources Hydra A and Virgo A. These sources are many arcminutes in size with integrated flux densities on the order of hundreds of Janky's. I will consider these two sources in Section 4.4. The next Section follows the filtering process used to subset the sky-model for the missing regions.

4.3.1 Filtering Process

The GLEAM sky-model catalogue was subset by cross-matching it with the PUMA300 catalogue and selecting only the sources without matches up to 5 arcminutes. This constituted $48,816$ sources in total. This subset covered the GP, the LMC, the SMC and the Cen A region, as well as a small collection of sources that were not included in the original PUMAcat. Some of these sources were components of A-team models, in particular Gaussian components of Hydra A and Virgo A. These A-team sources were removed and will be considered separately in Section 4.4. This new subset from hereon is referred to as the GLEAM supplementary (GLEAM_Sup) catalogue (or sky-model). The recorded flux density of these sources is at 200 MHz, and so this needs to be converted to 300 MHz.

---

[6]https://github.com/nhurleywalker/GLEAM-X-pipeline

4.3.2   Transforming GLEAM Fit Coefficients

As mentioned previously sources in the GLEAM_Sup sky-model were fitted with first and second order polylogarithmic functions with a reference frequency of $\nu_0 = 200\,\text{MHz}$. Therefore the spectral index α_{200} and the curvature term q_{200} are defined relative to this reference frequency. For reasons that will be explored in the next Chapter 5, the fit coefficients for sources with second order polylogarithmic fits need to be re-expressed in terms of a reference frequency of $\nu_0 = 300\,\text{MHz}$. For a second order polylogarithmic function this is a straightforward transformation where in Equation 2.2 a simple substitution of $\log_{10}\left(\nu/\nu_{200}\right) = \log_{10}\left(\nu/\nu_{300}\right) + \log_{10}\left(\nu_{300}/\nu_{200}\right)$, where the subscript indicates the reference frequency. This process can be generalised to higher order polylogarithmic functions, which in the next Section is necessary to describe the SEDs of some bright complicated sources. The general proof for an arbitrary order polylogarithmic coefficient transformation can be found in Section A.1 of the Appendix. For the main thesis work only the results of the GLEAM_Sup coefficient transformation are necessary:

$$\log_{10}(S_{300}) = \log_{10}(S_{200}) + \alpha_{200}\left(\log_{10}\left(\frac{300}{200}\right)\right) + q_{200}\left(\log_{10}\left(\frac{300}{200}\right)\right)^2 \quad (4.5)$$

$$\alpha_{300} = \log_{10}(S_{200}) + 2\alpha_{200}\left(\log_{10}\left(\frac{300}{200}\right)\right) \quad (4.6)$$

$$q_{300} = q_{200}. \quad (4.7)$$

For sources which were preferentially fit with a single power law, the coefficient transformation is trivially given by:

$$\log_{10}(S_{300}) = \log_{10}(S_{200}) + \alpha_{200}\left(\log_{10}\left(\frac{300}{200}\right)\right) \quad (4.8)$$

$$\alpha_{300} = \alpha_{200}. \quad (4.9)$$

The above expressions for the polylogarithmic coefficients at a reference frequency of $\nu_0 = 300\,\text{MHz}$ were used to transform the GLEAM_Sup catalogue into a 300 MHz sky-model. With this inclusion to the PUMA300 catalogue, and the TGSS/NVSS catalogue the total 300 MHz sky-model is almost complete.

4.4   A-team Sources

The A-team sources constitute a collection of exceptionally bright radio galaxies, a large portion of which are extended and resolved at MWA frequencies (such as Fornax A). Some are only partially resolved or completely unresolved (such as 3C444 or Pictor A (Pic A)). Due to the bright nature of these sources, some of them have long been used as calibrators for radio interferometers (Perley & Butler, 2017). The fully resolved and partially resolved sources, typically have complicated morphologies which require multi-component models to describe the distribution of their flux densities (such is the case for Hydra A and Virgo A). Since these sources are incredibly bright, accurate models of their total SED's

Source	a_0^{1000}	a_1^{1000}	a_2^{1000}	a_3^{1000}	a_4^{1000}
Fornax A	2.218 ± 0.003	-0.661 ± 0.006			
Pictor A	1.9380 ± 0.001	-0.7470 ± 0.001	-0.074 ± 0.005		
Hydra A	1.78 ± 0.01	-0.918 ± 0.001	-0.084 ± 0.004	-0.014 ± 0.001	0.03 ± 0.003
Virgo A	2.466 ± 0.0007	-0.8116 ± 0.002	-0.048 ± 0.003		
Hercules A	1.8298 ± 0.0007	-1.0247 ± 0.0009	-0.0951 ± 0.0020		
Cygnus A	3.3498 ± 0.0010	-1.0022 ± 0.0014	-0.225 ± 0.006	0.023 ± 0.002	0.043 ± 0.005
3C444	1.1064 ± 0.0009	-1.005 ± 0.002	-0.075 ± 0.004	-0.077 ± 0.005	

Source	a_0^{300}	a_1^{300}	a_2^{300}	a_3^{300}	a_4^{300}
Fornax A	2.193 ± 0.003	-0.661 ± 0.006			
Pictor A	2.3144 ± 0.001	-0.6696 ± 0.001	-0.074 ± 0.005		
Hydra A	1.6152 ± 0.01	-0.948 ± 0.001	-0.0857 ± 0.004	-0.0072 ± 0.001	0.03 ± 0.003
Virgo A	2.3021 ± 0.0007	-0.8285 ± 0.002	-0.048 ± 0.003		
Hercules A	2.3396 ± 0.0007	-0.9252 ± 0.0009	-0.0951 ± 0.0020		
Cygnus A	3.8122 ± 0.0010	-0.7726 ± 0.0014	-0.1905 ± 0.006	0.0669 ± 0.002	0.043 ± 0.005
3C444	1.6229 ± 0.0009	-0.9897 ± 0.002	0.0458 ± 0.004	-0.077 ± 0.005	

Table 4.3: The top panel provides the coefficients for each of the considered A-team sources, where the coefficients were fit at a reference frequency of $\nu = 1000\,\mathrm{MHz}$ by Perley & Butler (2017) using arbitrary polylogarithmic functions. The 1 GHz fitted coefficients have the superscript 1000. The bottom panel shows the transformed coefficients, where the reference frequency is now $\nu_0 = 300\,\mathrm{MHz}$ for the A-team sources in Table. The transformed coefficients have the superscript 300.

are a necessity if they are to be properly calibrated in the 300 MHz apparent-sky-models. Small errors on the order of 10% in some of these sources can lead to errors in the range of $1-100\,\mathrm{Jy}$. These errors vary depending on the location of the source relative to the main lobe or the grating sidelobes, which at 300 MHz are comparable in sensitivity to the main lobe. Therefore it is paramount to have accurate models of their SED's in order to have accurate calibration solutions for 300 MHz observations.

Perley & Butler (2017) provide a comprehensive model of a selection of 20 bright radio galaxies, most of which are A-team sources. These models are used to determine a new absolute flux scale from $50\,\mathrm{MHz}-50\,\mathrm{GHz}$, effectively covering three orders of magnitude. This work improved on the previous absolute scale of Baars et al. (1977) who fitted arbitrary order polylogarithmic functions to the SED's of these bright calibrator sources, with a reference frequency of $\nu_0 = 1\,\mathrm{GHz}$. The fit coefficients for the total SED's for these sources can be found in the top panel of Table 4.3.

As mentioned in Section 4.3 the fit coefficients need to be transformed to a reference frequency of $\nu_0 = 300\,\mathrm{MHz}$. The method outlined in the Appendix Section A.1 was used to transform the A-team fit coefficients from 1 GHz to 300 MHz. The new fit coefficients at 300 MHz can be found in the bottom panel of Table 4.3.

The validity of the flux scale presented in Perley & Butler (2017) below 240 MHz is not certain, due to the reliance on a single measurement at 74 MHz. As such the flux density scale at lower frequencies may not be ideal, and it may be necessary in future work to compare the flux density scale with MWA measurements at lower frequencies. For now the models presented in Perley & Butler (2017) will be used to determine the flux density of the A-team sources as well as their spectral behaviour for the total 300 MHz sky-model.

4.4.1   Hydra A & Virgo A

Hydra A and Virgo A are considered separately because they are partially or fully resolved at higher MWA frequencies. In the GLEAM_Sup 200 MHz sky-model these two sources are modelled with multi-component Gaussian models. The total SED's for these two sources was taken from Perley & Butler (2017). The flux density for each of the components was determined by multiplying the fraction of the total 200 MHz flux density of that particular component, by the total 300 MHz flux density from Table 4.3. For an arbitrary component with subscript a this is defined below in both log-space and normal-space:

$$\log_{10}\left(S_{\mathrm{a}}(\nu)\right) = \log_{10}\left(\frac{S_{\mathrm{a,200}}}{S_{\mathrm{tot,200}}}S_{\mathrm{tot,300}}\right) + \sum_{i=1}^{p} a_i\left(\log_{10}\left(\frac{\nu}{\nu_{300}}\right)\right)^i \qquad (4.10)$$

$$S_{\mathrm{tot},\nu} = \frac{S_{i,200}}{S_{\mathrm{tot,200}}}S_{\mathrm{tot,300}}\left(\frac{\nu}{\nu_{300}}\right)^{a_1 + \sum_{i=2}^{p} a_i\left(\log_{10}\left(\frac{\nu}{\nu_{300}}\right)\right)^{i-1}} \qquad (4.11)$$

In the above equations p denotes the order of the arbitrary polylogarithmic fit applied in Perley & Butler (2017), and the subscripts 200 and 300 represent the values at that particular frequency in MHz. Each component of the Hydra A and Virgo A models was additionally renamed, where each component was given a designation of the form `Virgo Aa`, $\cdots$, `Virgo Ah`.

4.4.2   Fornax A

Since the GLEAM_Sup 200 MHz sky-model does not contain a model of Fornax A a bespoke model was required, where the total SED for Fornax A was derived from the flux scale paper (Perley & Butler, 2017). It should be noted that in Perley & Butler (2017) they consider the fit for Fornax A to not be reliable due to the extended nature of the source. More accurate models do exist, such as the shapelet model described in Procopio et al. (2017), but since CALIBRATE is not compatible with shapelet models I could not use it in this work. As a result of these restrictions as well as time constraints, I constructed a relatively simple point source model to meet the needs of the sky-model.

I derived the point source model for Fornax A by using a GLEAM cutout image of Fornax A from the 227 MHz subband. These cutout images come from the GLEAM VO[7] server, which is a public service that offers GLEAM cutout images for given RA and DEC coordinates. I chose the 227 MHz subband because it is closer to the resolution of the MWA at 300 MHz than the other subbands which means the same features should be present at 300 MHz. Using the astronomy image software `ds9` I set the flux scale of this image to a min max setting so the finer features of the structure of Fornax A were present. I then overlaid Contours, where the contours were defined in a linear scale with 12 flux density bins. In `ds9` I defined regions using the major and minor axes of the MWA PSF for this cut out image. Copies of these regions were then made and placed on prominent features with the aid of the contours. The naming convention used in Subsection 4.4.1 was also applied to the point source components of Fornax A, except for the

---

[7]http://gleam-vo.icrar.org/gleam$_p$ostage/q/form
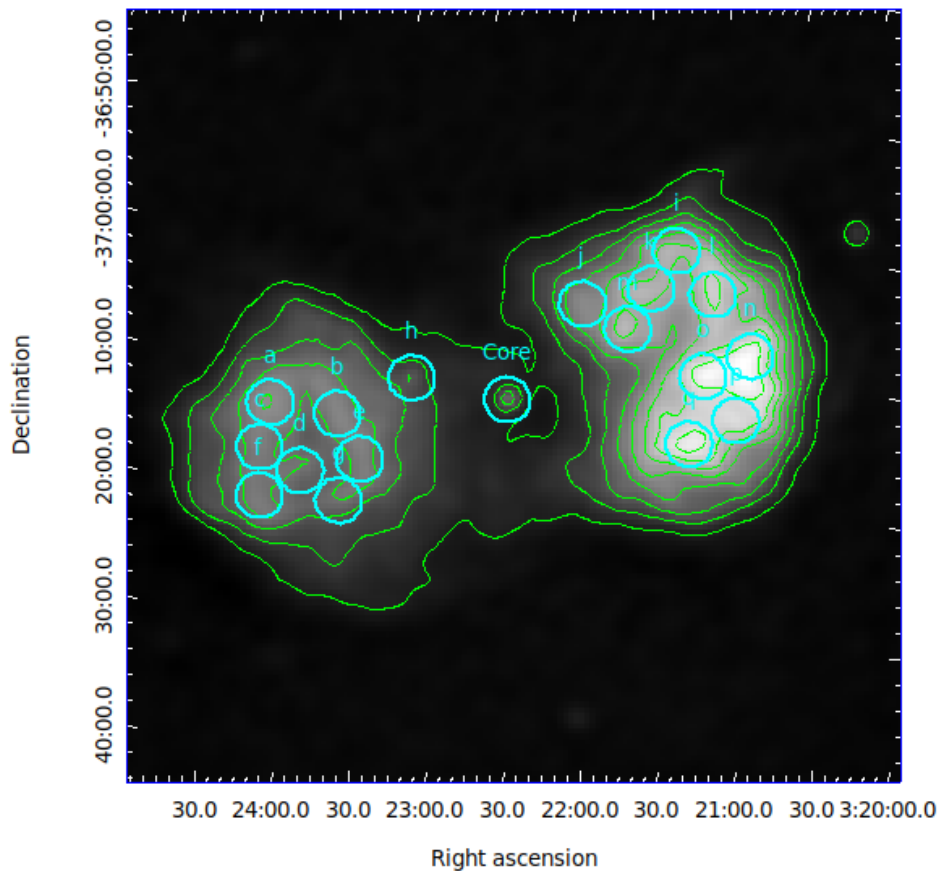
Figure 4.6: Multi-component point source model of Fornax A. The scale is a min max scale, where the green contours represent 12 linear flux density levels. The cyan circles represent the psf sized point source components. An additional point source J032033-365727 can be seen to the right as outlined by the green contours.

core which was uniquely identified. The resulting point source model can be seen in Figure 4.6, where the contours are presented in green, and the point source components are in cyan. Each has been labelled. In total there are 18 point sources in the model. An additional point source J032033-365727 which was not previously in the catalogue was added to the model as well.

The shortfall of this model is that it does not capture the entire extended scale of the flux density distribution of Fornax A. As such a lot of the large scale emission is omitted in this model. This issue was partially side stepped by assuming the total flux density SED of Perley & Butler (2017) was representative of the total emission of Fornax A. The 300 MHz flux density for each component was determined using the same method outlined in Subsection 4.4.1.

4.4.3 Single & Double Sources

The remaining sources in Table 4.3 are partially resolved or unresolved. For the sources that are expected to be fully resolved or partially resolved in some 300 MHz observations, I modelled them with two point sources. The point source

model for Pic A was updated from the GLEAM_exGal catalogue, by using a GLEAM cutout image of Pic A at 227 MHz (Hurley-Walker et al., 2017). The Pic A cutout image was aquired from the public GLEAM VO[8] server. I applied a similar method to Pic A as was used for Fornax A. In this case I fit ellipses manually to the two lobes of Pic A. I then determined the relative flux density contributions to the total flux density. The contributions for the left and right lobes were approximately 50%. Using the new model at 300 MHz the contributions at the new reference frequency were determined. For 3C444 this is an unresolved radio galaxy at lower MWA frequencies and is only expected to be partially resolved at 300 MHz. As such the flux density contributions for both lobes could not be estimated so I assumed them to be 50%. I assumed Hercules A and Cygnus A to be point sources with total SEDs taken again from (Perley & Butler, 2017).

4.5   Total 300 MHz Sky-Model

With the PUMA300 catalogue, the TGSS/NVSS300 catalogue, the GLEAM_Sup catalogue and the A-team model the first total sky-model version at 300 MHz is now complete (Total300). Figure 4.7 is an Aitoff projection of the total sky-model onto the celestial sphere. This image shows the different contributing components to the patchwork sky model, where the red region indicates the PUMA300 model, the blue region indicates the GLEAM_Sup contribution, the grey region indicates the TGSS/NVSS300 region, and the assorted shapes indicate the positions of the more prominent A-team sources. Total300 covers the entire southern sky south of DEC $< +45$ deg, with the exception of a missing region RA $\in [127, 140]$ deg and DEC $\in [30, 37]$ deg. This region is missing in the TGSS/NVSS catalogue (de Gasperin et al., 2018). There are additional incomplete regions in the Total300 catalogue which can be seen in Figure 4.7. These regions are found at the boundaries between catalogues. Future all-sky surveys such as the Rapid ASKAP Continuum Survey (RACS), which covers the entire sky south of $+40$ deg in the frequency range 700-1800 MHz, will be able to fill in some of the missing gaps in spectral information and in the sky for the total sky survey (McConnell et al., 2020).

4.5.1   Total Sky-Model Statistics

Now that the total sky-model Total300 is complete, the statistics of the sample and the component sub-samples can be analysed. Figure 4.8 shows three Subfigures. Subfigure 4.8a is the log-flux density of the three main samples PUMA300 in red, GLEAM_Sup in blue, and TGSS/NVSS in grey. This colour convention for each sub-sample is kept consistent throughout this Chapter. I excluded the A-team sample because it contains many orders of magnitude fewer sources than the three other components. The log-flux density histograms are normalised to the area of the histogram such that they are plotted on the same scale. The median flux density, the IQR for each of the subsets, the number of sources in

---

[8]http://gleam-vo.icrar.org/gleam$_p$ostage/q/form
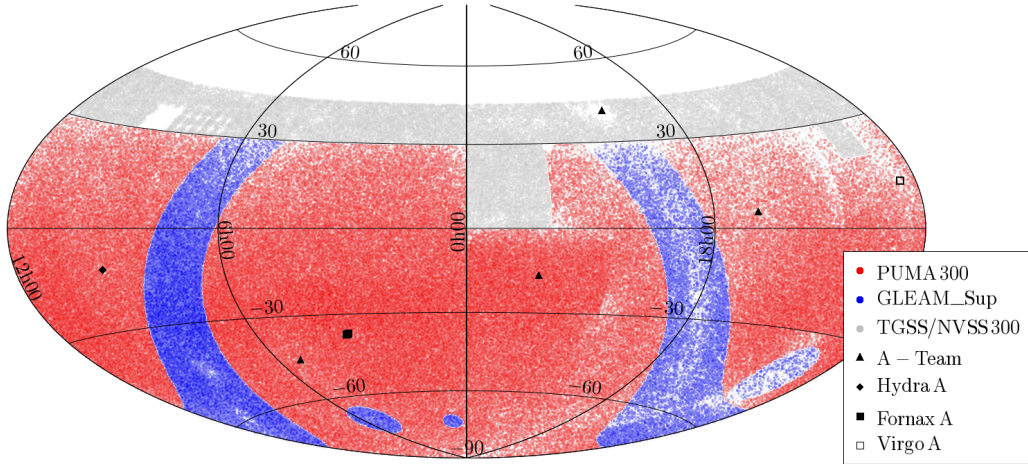
Figure 4.7: 2D Aitoff projection of the celestial sphere, where the red sources correspond to the PUMA300 catalogue, the blue sources to the GLEAM_Sup sub-sample, the grey sources to the TGSS/NVSS300 sky-model, and the various black shapes to the A-team sub-sample. Sources from each catalogue are plotted with a transparency factor to accentuate the density features of source distributions. Important to note that the TGSS/NVSS300 sub-sample is a lot denser than the other samples. This is not apparent with the current transparency setting.

Catalogue	$\langle S_{300} \rangle$ [Jy]	$\langle \alpha \rangle$	$\langle q \rangle$	N
PUMA300	0.095 ± 0.135	-0.814 ± 0.253	-0.170 ± 0.882	$308,563$
GLEAM_Sup	0.136 ± 0.194	-0.799 ± 0.604	0.271 ± 1.330	$48,816$
TGSS/NVSS300	0.091 ± 0.117	-0.736 ± 0.275	-	$75,916$
Total	0.0981 ± 0.140	-0.805 ± 0.269	-0.098 ± 0.908	$433,345$

Table 4.4: Statistics for the three main subsets of the total 300 MHz sky-model. The total number of sources in this table also includes the A-team sources which are not listed in this table.

each subsets is given in Table 4.4. I chose the median over the mean as a representation of the average because it is more robust to skewness. Skewness is clearly present in the distributions shown in Figure 4.8. Likewise the IQR is a more robust choice than the standard deviation in estimating the distribution widths, since it is less affected by the skewness of the distributions.

300 MHz Flux Density Distribution

In Figure 4.8a the PUMA300 and TGSS/NVSS samples show a high degree of similarity, with similar skewness and median values as see in Table 4.4. This is indicative of the flux density re-scaling applied in Section 4.2. Interestingly the GLEAM_Sup sub-sample deviates from this distribution, but likewise shows a similar skewness towards higher flux densities. The deviation could be explained by the lack of high frequency information for the GLEAM sky-model. The missing high frequency data means that the 300 MHz flux density has to be estimated through extrapolation. This could potentially explain the offset between the PUMA300 and GLEAM_Sup flux density distributions. This offset could be analysed by cross-matching and comparing the 300 MHz flux densities

(a) $\log_{10}(S_{300})$ Histograms

(b) α Histograms
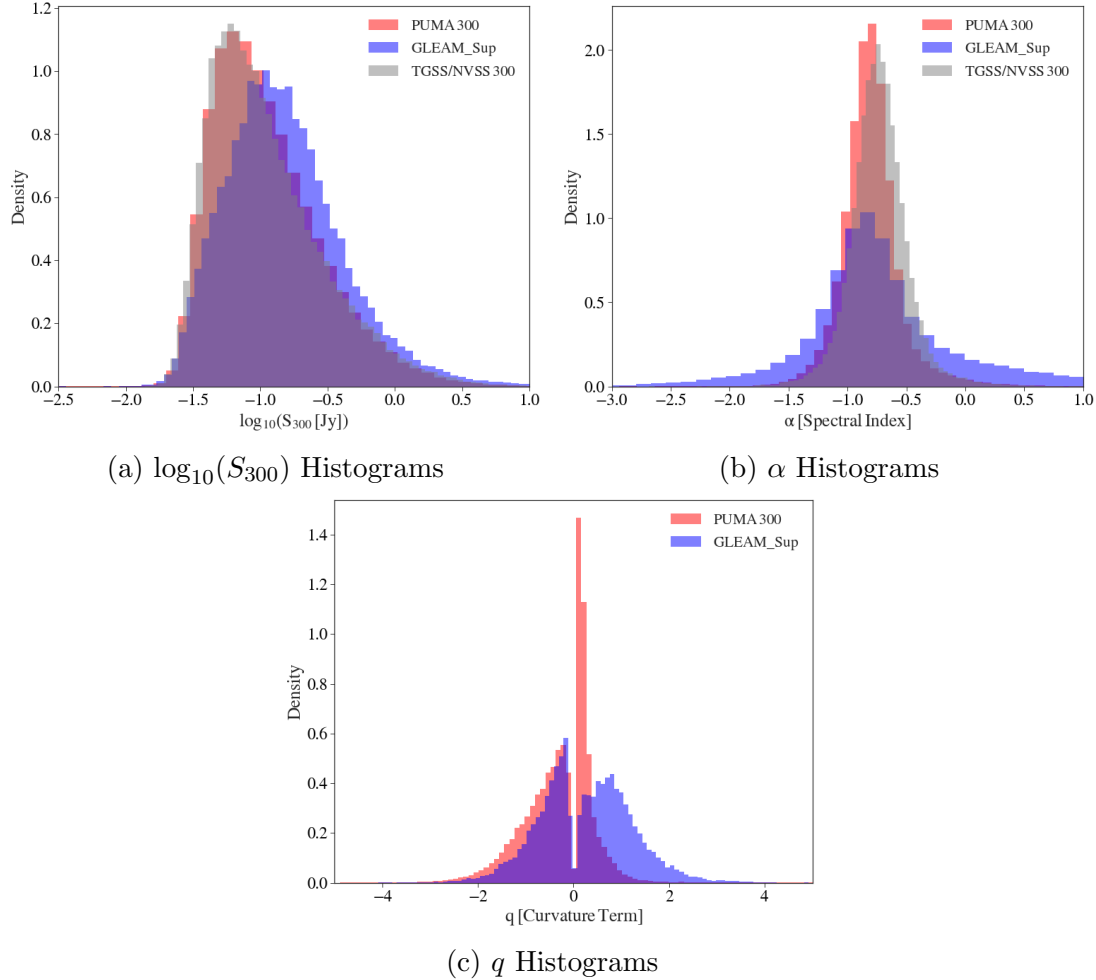
(c) q Histograms

Figure 4.8: Shows the sub-sample catalogues of Total300, where the red histogram is the PUMA300 sample, the blue histogram is the GLEAM_Sup sample, and the grey histogram is the TGSS/NVSS300 sample. Subfigure (a) shows the $\log_{10}(S_{300})$ distribution for each sample. Subfigure (b) shows the sub-sample distributions for the spectral index, as expected these are peaked about a value $\alpha \in [-0.7, -0.8]$, notably the GLEAM_Sup sample has a larger standard deviation. Subfigure (c) shows the distribution of the q-curvature term for PUMAS300 and GLEAM_Sup, this distribution has filtered out all sources where $q = 0$. Sources with $q = 0$ are sources with a preferential power law fit to their SED. Notably the GLEAM_Sup sub-sample again has a wider distribution of values, with a mean close to $\langle q \rangle = 0$, whereas the PUMAS300 sample appears to be skewed towards negative q values.

for the PUMA300 catalogue and the entire GLEAM sky-model catalogue. This would indicate if there is an average population overestimate. This could then be accounted for by down scaling the GLEAM_Sup sky-model in a similar fashion to the up scaling performed with the TGSS/NVSS300 catalogue.

It should be noted that the distributions presented in Figure 4.8a are not sensitive to large scale diffuse radio emission. The GLEAM observations I discussed in Chapter 3 excluded shorter baselines larger than $\sim 1\,\mathrm{deg}$ due to the large scale diffuse Galactic emission. This means that large scale radio emission is not encapsulated in the Total300 sky-model. This should not be an issue for the 300 MHz observations that I processed as part of this thesis. Similarly I do not include short baselines on the same $\theta > 1\,\mathrm{deg}$ angular scales as lower frequency MWA observations to avoid large scale diffuse emission.

Spectral Index Distribution

Subfigure 4.8b shows the spectral index distributions for each of the three main catalogues of Total300, where the median and IQR values can be found again in Table 4.4. Each subset has a median value close to the accepted literature value of $\alpha \sim [-0.7, -0.8]$ (Conway et al., 1963; Kardashev, 1962; Condon, 1992). It should be noted that the median spectral index value for the PUMA300 and GLEAM 2019 catalogues includes sources with curvature terms. When isolating sources that only had a power law fit, the mean spectral indices for both the PUMA300 and GLEAM_Sup catalogues are $\langle \alpha_{\mathrm{PUMA}} \rangle = -0.820 \pm 0.244$ and $\langle \alpha_{\mathrm{GLEAM}} \rangle = -0.833 \pm 0.358$ respectively, both of which are within agreement with results from Hurley-Walker et al. (2017, 2019). Interestingly the mean spectral indices for sources with curvature terms are $\langle \alpha_{\mathrm{PUMA}} \rangle = -0.756 \pm 0.353$ and $\langle \alpha_{\mathrm{GLEAM}} \rangle = -0.608 \pm 1.338$ respectively. The flattening of the spectral index for sources with curvature could suggest that the inflection point (whether it be for concave or convex spectra) could be close to the reference frequency $\nu_0 = 300\,\mathrm{MHz}$. This would cause the gradient at the reference frequency to flatten.

Curvature Term Distribution

Subfigure 4.8c shows the distribution of sources with curvature terms for the PUMA300 catalogue and the GLEAM_Sup catalogue. All sources with $q = 0$ were subsetted from the data set. Sources with $q = 0$ correspond to sources with a preferential power law fit to their SED's. This partly explains why there is a missing chunk in the middle of the distribution. Depending on the data it may not be possible in many cases to identify sources with curvature in the domain where $q \to 0$. The median values and the IQR for both subsets are given in Table 4.4. Interestingly the GLEAM_Sup and the PUMA300 catalogues show opposite skews, with the PUMA300 data skewed right (negative), and the GLEAM_Sup data skewed left (positive). This skew maintains itself for the full GLEAM_Sup catalogue. In comparison to PUMA300 which has only 13% of its sources with appreciable curvature, GLEAM_Sup has 33% of sources have non-zero curvature terms. This is almost a factor of three times higher than that reported in the PUMA300 catalogue. Additionally most sources have convex curvature ($q > 0$) instead of concave curvature ($q < 0$) which might initially be expected to be more likely. A potential explanation for this might be that the model selection
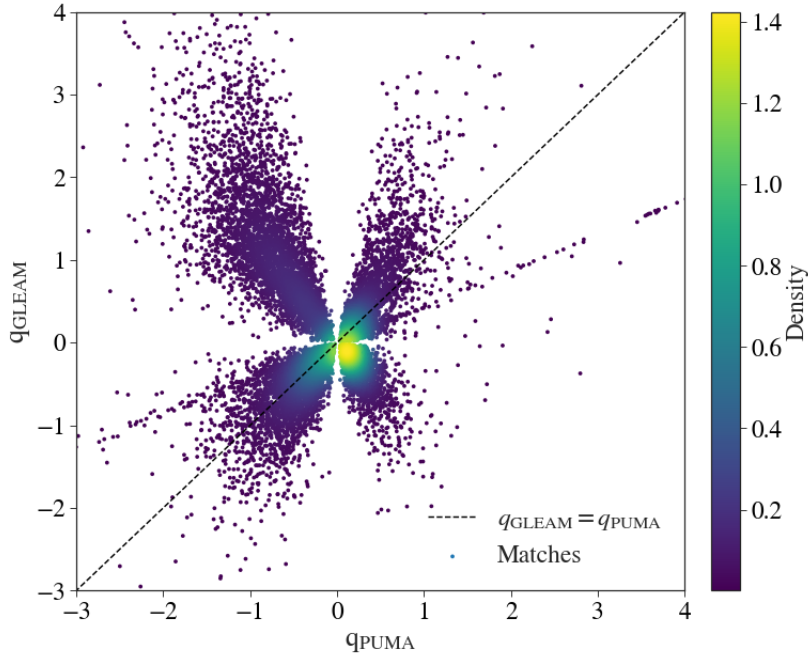
Figure 4.9: The q_{PUMA} curvature term is plotted against the q_{GLEAM} curvature term for 18,045 sources that were cross-matched in GLEAM_Sup and PUMA300. The colour bar indicates the density of points determined using a kernel density estimator. There are two important features in this plot. The "butterfly" feature, which indicates that there is no solid agreement between both curvature terms. This feature is also a result of filtering out sources with $q = 0$ which corresponds to power law fit sources. The second feature is the straight line that cuts through the negative and positive quadrants. Additionally the dashed black line represents $q_{\mathrm{GLEAM}} = q_{\mathrm{PUMA}}$.

criteria used in creating the GLEAM_Sup 200 MHz sky-model may not have been as stringent as the PUMA300 sky-model. Potential evidence for this comes from For et al. (2018) who used a $\Delta \mathrm{BIC} > 2$ as their significance threshold to accepting a model with curvature. Additionally with only low frequency data the curvature is not as well constrained for these sources.

To investigate these two claims, a comparison can be made between the GLEAM_Sup and the PUMA300 catalogue. These two catalogues were cross-matched together with a maximum separation of two arcminutes. This yielded a matched catalogue of $307,358$ sources. Of these matches $40,910$ had PUMA curvature terms and $99,225$ had GLEAM curvature terms. These two subsets were then cross-matched together which yielded a match of $18,045$ sources. This constitutes less than 50% of the PUMA300 catalogue and less than 20% of the GLEAM_Sup catalogue. Figure 4.9 plots the PUMA300 curvature term q_{PUMA} against the GLEAM_Sup curvature term q_{GLEAM}. If the two fits were in agreement the source points should only occupy the positive and negative quadrants of Figure 4.9 with some scatter. This does not appear to be the case. There is almost an even spread throughout each quadrant. There does appear to be a straight line that cuts through the origin starting in the negative quadrant then passing through to the positive quadrant. The sources on this straight line would seem to indicate a linear relationship between q_{PUMA} and q_{GLEAM}. Since there is no appreciable scatter, it would seem to indicate that these sources likely

Column Name	Format	Notes
Name[a]	-	Unique source identification of the format JHMS $\pm$ DMS
RA	degree	Right ascension
DEC	degree	Declination
PA	degree	Position angle
Major	degree	Major axis
Minor	degree	Minor axis
Fint300	Jy	Total integrated flux density
coefficients[b]	Tuple	SED polylogarithmic coefficients
Flag	Integer	Subset flag

[a] The naming convention takes exception to A-team sources. The format used for A-team sources is laid out in Subsection 4.4.

[b] The polylogarithmic coefficients for a source are formatted in a tuple of size 6 with the format $(a_0, a_1, \cdots, a_6)$. Sources with only a power law or second order polylogarithmic fit have coefficients a_3 to a_6 set to a value of 0. Coefficient a_1 is the spectral index, a_2 is the curvature parameter, and a_0 is the log of the 300 MHz flux density.

Table 4.5: Shows the column format for the Total300 sky-model table.

correspond to PUMA sources which only had GLEAM data. Therefore the data used to determine the curvature term in the GLEAM_Sup and PUMA300 catalogues should be the same. It would then be expected that the gradient of this straight line should corresponds to $q_{\mathrm{PUMA}} = q_{\mathrm{GLEAM}}$, but it clearly does not. To demonstrate this I plotted a dash black line in Figure 4.9 where $q_{\mathrm{PUMA}} = q_{\mathrm{GLEAM}}$. This could be caused by systematic differences in how the fitting is performed. Importantly in these sources in particular when the range of the axes is extended there is a visible bias towards positive curvature. This seems to give evidence towards the previous claim. Higher frequency information may correct the bias.

4.5.2 Total 300 MHz Catalogue

The total-sky model at 300 MHz contains $433,345$ radio sources is available in a catalogue format, where the catalogue columns are laid out in Table 4.5. Each of the main subsets described in the previous Sections are given flag values, where a flag value of 1 indicates the PUMA300 catalogue; flag value of 2 indicates the GLEAM_Sup catalogue; flag value of 3 indicates the TGSS/NVSS catalogue, and flag value of 4 indicates the A-team sources. This total 300 MHz sky-model catalogue is available in the github repository S300-PIPELINE[9].

4.6 Summary

In this Chapter I laid out the method I used to create the total 300 MHz sky-model Total300. This sky-model comprises three main components. The first is the PUMA300 sky-model which is the GLEAM_exGal catalogue as a base catalogue cross-matched with higher frequency catalogues such as NVSS. I used this to interpolate the 300 MHz flux density of these radio sources using a power law

---

[9]https://github.com/JaidenCook/300-MHz-Pipeline-Scripts

or second order polylogarithmic function. The second component is the TGSS/N-VSS spectral index catalogue subset. This covers the two wedge regions absent from GLEAM_exGal as well as declinations higher than $+30$ deg, in the frequency range $150-1400$ MHz. The third main component is GP, LMC, SMC and Cen A GLEAM data releases (GLEAM_Sup). In this sample I extrapolated the 300 MHz flux density from the GLEAM-X sky-model. With the addition of bespoke A-team models to these three main component catalogues, the total catalogue covering the entire southern sky in the declination range DEC $\in$ $[-90, 45]$ deg is now largely complete. With the Total300 sky-model it is now possible in conjunction with the FEE MWA tile beam model to create apparent sky-models to calibrate MWA observations at 300 MHz.

Chapter 5

Calibration Strategy

With the creation of the Total300 sky model as described in Chapter 4 we can now focus on building the apparent sky model for a particular observation and calibrating the raw data. This Chapter aims to demonstrate the framework built to process MWA 300 MHz observations, from downloading the raw data files to correcting and calibrating the data so it can be imaged.

In this Chapter the process is demonstrated by focusing on several example observations. The first observation has the main lobe of its primary beam dominated by the bright partially-resolved calibrator source Pic A. This observation is given the ID (OBSID) 1131042024 (from hereon ObsA), and is an off zenith pointed observation. The OBSID is a unique identification tag for MWA observations that reflects the GPS time the observation started. The second observation is taken in the same night as the first and has the OBSID 1131038424 (from hereon ObsB). ObsB has the same off-zenith pointing as the first observation. This means that the primary beam patterns for both observations are the same. The third observation 1121285808 (from hereon ObsG23) is a close to zenith pointing observation of the GAMA 23 field, and the fourth observation 1145130584 (from hereon ObsZen) is a zenith pointed observation. Observations one and two are the main focus of this Chapter. Observations three and four are useful examples that demonstrate the changing primary beam behaviour across the sky and across the 300 MHz bandwidth. These effects are not as obvious with observations one and two. Observations three and four are the focus of Section 5.2.3. All four observations are publicly available, and were taken during an extension of the second year of the GLEAM survey[1].

Unlike ObsA, the visibilities of ObsB are not dominated by a bright calibrator source such as Pic A. This poses a challenge to the apparent sky-model calibration method. As a result this Chapter proposes a second calibration strategy for these types of observations that reflects the more traditional calibration methods employed in radio astronomy. This second strategy involves transferring the calibration solutions from ObsA to ObsB. I outlined both strategies in Chapter 2. In this Chapter I will also present the various algorithms written in bash and PYTHON scripts for processing the two example observations A and B. In Section 5.1 I outline the acquisition of raw MWA 300 MHz observations and the preliminary data processing and flagging. In Section 5.2 I outline the theory and

---

[1]These observations have the project ID G008

method behind building the apparent sky model for the two example observations. In Section 5.3 I detail the apparent sky model calibration and the results of applying that calibration to the two example observations. Section 5.4 outlines the self-calibration method applied to observations after initial calibration phase in Section 5.3. Finally 5.5 outlines the calibration solution transfer method.

5.1   Raw Observation Data

There exists a large archive of publicly available MWA Phase I observations, which includes all-sky observations at 300 MHz. These are available on the MWA All-Sky Virtual Observatory (ASVO)[2] server. This service allows the user to download observations in one of two forms. The first form is the raw un-processed data in the form of gpu fits files, this is the form used in this project. The second form is the processed data which has been flagged for RFI and consolidated into a measurement set. Measurement sets are a flexible database format for radio astronomy data, specifically for visibilities generated from radio interferometers (Kemball & Wieringa, 2000). This data format is capable of storing the raw uncorrected visibilities, the corrected visibilities and the model visibilities for an observation in a single table-like database. It can also store the flags for the data, making it a very useful database format. Additionally the measurement set format is built upon the CASACORE[3] C++ library which is used by most of the radio astronomy software in this thesis.

Once the raw gpu FITS files for an observation are downloaded from the ASVO server, they have to be averaged in time and frequency, as well as consolidated into a measurement set. This is performed by the tool COTTER written by Offringa et al. (2015) specifically for MWA observations. For the observations discussed in this thesis the chosen averaged time resolution was $4\,s$ and averaged frequency resolution was 40 kHz. One of the main tasks of COTTER is to flag fine channels that are known to be bad in MWA data. These specific channels are bad as a result of aliasing, and cable reflections. Due to these effects bad channels occur in known locations across the bandwidth at the edges and centre of each coarse channel. This flagging step was performed with COTTER for all the observations discussed in this thesis. After this step, COTTER then optionally performs a round of RFI flagging on the newly consolidated data using the tool AOFLAGGER (Offringa et al., 2015). This process was also applied to the observations discussed in this thesis, since RFI corruption is a common issue in radio interferometric data.

Figure 5.1 shows the visibility amplitude versus frequency plot for each fine channel (40 kHz) for each tile from ObsA. This plot shows the visibility amplitude data for ObsA after flagging and processing by COTTER. RFI spikes are clearly present at multiple coarse channels across the entire bandwidth. This result is important since it indicates that AOFLAGGER is not successfully eliminating most of the RFI, and this appears to be a consistent feature of all observations at 300 MHz. As such it is important that the data corrupted by RFI be removed. There is no such tool available to identify and remove all of the remaining RFI. Therefore I developed a new flagging strategy that combines pre-existing tools

---

[2]https://asvo.mwatelescope.org/dashboard
[3]http://casacore.github.io/casacore/
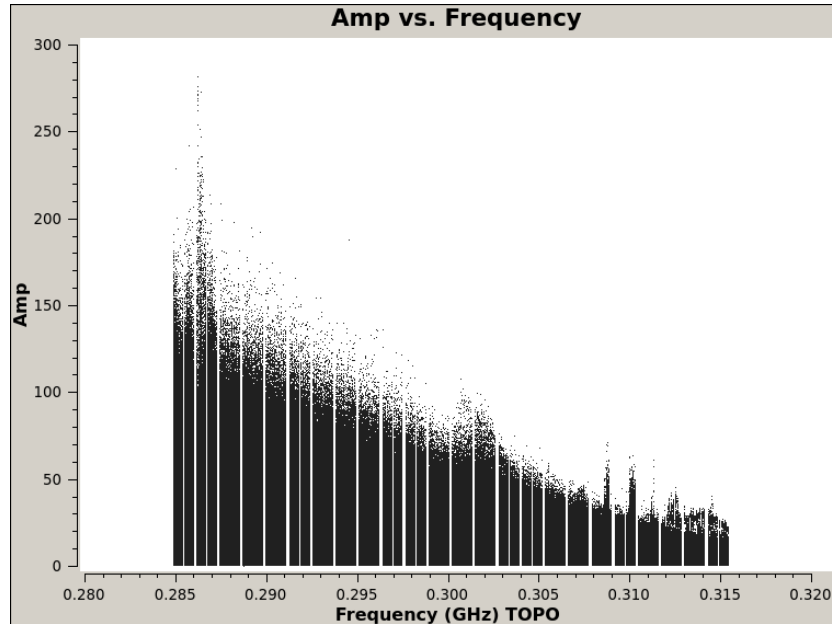
Figure 5.1: Amplitude versus frequency plot for observation A of Pic A. This plot shows the full bandwidth of the observations, where each point is a single fine channel, and the fine channels of each tile are plotted. The edges of each coarse channel are flagged due to aliasing effects as well as the centre of each coarse channel. RFI spikes are clearly present at multiple subbands across the full bandwidth.

in an iterative process to remove as much RFI as possible. This new strategy I developed can be applied at any point in the data processing described throughout this Chapter. I describe the tools and the strategy in the following Section.

5.1.1 RFI Flagging Strategy

RFI across the bandwidth poses a serious challenge when processing and imaging MWA observations at 300 MHz. If unaccounted for, RFI can make it impossible to image observations because the amplitude introduced by RFI in certain channels far outweighs that from astronomical sources. Sources of RFI can be terrestrial or they can come from satellites. Throughout this project I have observed the lowest fine channels (around 284.64 MHz) in the 300 MHz sub-band to be the most affected by RFI. This is clearly present in Figure 5.1. An example of RFI from a satellite can be seen in Figure 5.2. This image shows a suspected satellite found in an all-sky image of the observation A. The all-sky image will be discussed in further detail in Section 5.4. The apparent flux density of this source is 7 Jy. This source is located far from the main lobe in ObsA in a Section of the sky which the beam attenuates by a factor of $\sim 10^{-3}$. This means that this particular source has an approximate flux density of 7000 Jy. This is brighter than any of the 300 MHz flux densities predicted in the Total300 sky-model. Additional sources of RFI have not been identified but their effects can be seen in images as patches of high signal-to-noise ratio (SNR). These patches tend to have specific fringe patterns which indicates that certain baselines are more affected by RFI than others.

To remove the RFI missed by AOFLAGGER, I developed an RFI flagging strategy using tools from the Common Astronomy Software Applications package
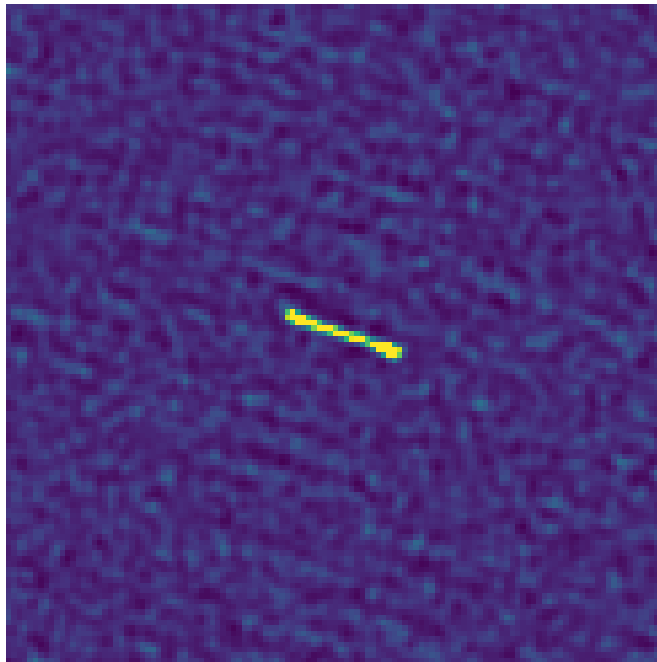
Figure 5.2: Satellite found in an all-sky image of ObsA. This is far from the main lobe or any grating lobes, in a region where the primary beam attenuates the flux density by a factor of 0.001. This has an apparent flux density of $\sim 7\,\mathrm{Jy}$, which means its actual flux density is approximately 7000 Jy, which would indicate it is emitting not reflecting RFI.

(CASA McMullin et al., 2007). This software package is capable of flagging and calibrating radio astronomy data. For the purposes of this work I only use CASA for its data flagging functionality. Specifically CASA is a PYTHON package that acts as a virtual IPython environment for the CASACORE library, and its native radio astronomy data structure is the measurement set. This makes it very user friendly therefore it was a natural choice to use CASA in this project. The flagging strategy I developed proceeds in three steps, with an optional fourth step to flag specific coarse channels. The flagging steps I chose for this strategy are encapsulated in the bash script `flag-routine.sh`. This script takes observation metadata, the measurement set data column to flag, and the channels that the user wants to flag. Importantly this script can be called to flag data at any point during the processing phase, and will be used throughout the work I describe in this Chapter. This script is available with the rest of the software from this project in the github repository S300-PIPELINE[4]. The specific CASA flagging functions used by `flag-routine.sh` are ones designed to flag RFI. These functions are defined below.

clip: Flagging Specific Channels

CLIP[5] is a CASA flagging mode which takes a range of channels as input, and flags the channels with amplitudes outside of a specified range. In the case of MWA data the channels are the fine channels mentioned in Section 3.1. This

---

[4]https://github.com/JaidenCook/300-MHz-Pipeline-Scripts
[5]https://casa.nrao.edu/Release4.1.0/doc/UserMan/UserMansu159.html

mode is useful because it allows for the flagging of entire fine channels or (if the appropriate range of fine channels is given) even coarse channels. This is especially useful in the case of 300 MHz MWA observations where some coarse channels are heavily corrupted by RFI as seen in Figure 5.1.

rflag: General RFI Flagging

Similar to AOFLAGGER which performs RFI flagging in the time and frequency domain, RFLAG[6] is an iterative flagging algorithm which also operate in these domains. This is the primary flagging tool used in `flag-routine.sh` to remove the additional RFI missed by AOFLAGGER. This algorithm works by applying a sliding statistical filter in the time and frequency domains to determine outliers.

The first process of this algorithm uses a sliding statistical window in the time domain to calculate the local σ_{rms} for each channel (for this project each fine channel). It does this for both the real and imaginary visibility components. It then determines the median σ_{rms} across all channels. It then flags channels which have local σ_{rms} values greater than some user defined or default threshold. It applies a similar process to the frequency domain where the sliding statistical filter is calculated for each time step. Again visibilities are flagged if the local σ_{rms} deviation is larger than some threshold.

tfcrop: Narrow Band RFI Flagging

TFCROP[7], similarly to RFLAG and AOFLAGGER, operates in the frequency and time domains. Specifically TFCROP was designed to identify narrow band RFI peaks. The algorithm does this by averaging visibility data in the time domain. This creates an effective average bandpass which is then fitted with a piece-wise polynomial. This fit ensures a smooth bandpass template. By dividing this smooth bandpass template out of the data narrow peaks that deviate from the bandpass become more apparent. These peaks become narrow band RFI candidates. The standard deviation is then determined for each time step, and points that deviate some specified N times from the standard deviation are flagged. This process is repeated for five iterations with the standard deviation being recalculated after flagging. The algorithm then repeats the same process but in the frequency domain.

steflag: Baseline Flagging

STEFLAG[8] is a python script developed by Stefan Duchesne to flag baselines affected by RFI. In this project I have observed particular baselines in 300 MHz MWA to be more affected by RFI than others. This script applies a similar approach to the two aforementioned CASA functions. It calculates the mean and standard deviation of visibility amplitudes as a function of baseline chunks. It then flags antenna pairs that have amplitudes that are larger than a user defined standard deviation threshold (the default is 3σ). This script then outputs a list of antenna pairs to be flagged. This list can be read by CASA, where the antenna

---

[6]https://casa.nrao.edu/Release4.1.0/doc/UserMan/UserMansu164.html
[7]https://casa.nrao.edu/Release4.1.0/doc/UserMan/UserMansu163.html
[8]https://gitlab.com/Sunmish/piip/blob/master/ms_flag_by_uvdis.t.py

pairs can be manually flagged using the MANUAL flagging mode for the CASA function FLAGDATA.

In some cases this script fails to flag all the baseline dependent RFI. This could be improved by estimating the standard deviation using the IQR, since the baseline chunk distributions are going to be disproportionately skewed to higher amplitudes as a result of RFI. In future work this modification could be added to the script. In the interim a lower threshold could be applied, but this might over flag the data.

Algorithm

The CASA function FLAGDATA is used to perform all the flagging methods mentioned above. This function works by calling different flagging modes. These modes include the auto-flagging algorithms RFLAG, TFCROP, as well as the manual flagging algorithms CLIP and MANUAL. Each flagging step in `flag-routine.sh` calls a different instance of CASA. This instance runs the CASA function FLAGDATA with the appropriate input mode. The general process applied for each step in `flag-routine.sh` is described below.

1. If specified, `flag-routine.sh` accepts a range of coarse channels which it then converts to the appropriate fine channels range to be flagged by the FLAGDATA mode CLIP. The flagging process is applied to the data column of the observation measurement set. If multiple coarse channels are provided the clipping process becomes iterative.

2. Once coarse channels have been flagged CASA is called and the FLAGDATA mode RFLAG is applied to the data. The default parameters are used for this mode. The flagging process is applied to the data column of the observation measurement set.

3. CASA is called again and the FLAGDATA mode TFCROP is applied with default parameters. The flagging process is applied to the data column of the observation measurement set.

4. The PYTHON script STEFLAG is then applied to the measurement set data column with default parameters. This then outputs a text list. CASA is then called with the FLAGDATA mode MANUAL. The antenna list is then passed to the antenna variable in the function FLAGDATA..

5. CASA is then called where the function PLOTMS is used to make plots of the amplitude versus frequency and amplitude versus baselines for all MWA tiles for this observation.

Flagging Results

`flag-routine.sh` was applied to ObsA. Figure 5.3 shows the new amplitude versus frequency plot after the data have been flagged for RFI. There is a clear improvement; a large portion of this comes from flagging the first four coarse channels. As previously stated these coarse channels contain a large amount of RFI. This corruption at lower frequencies seems to be a persistent feature in
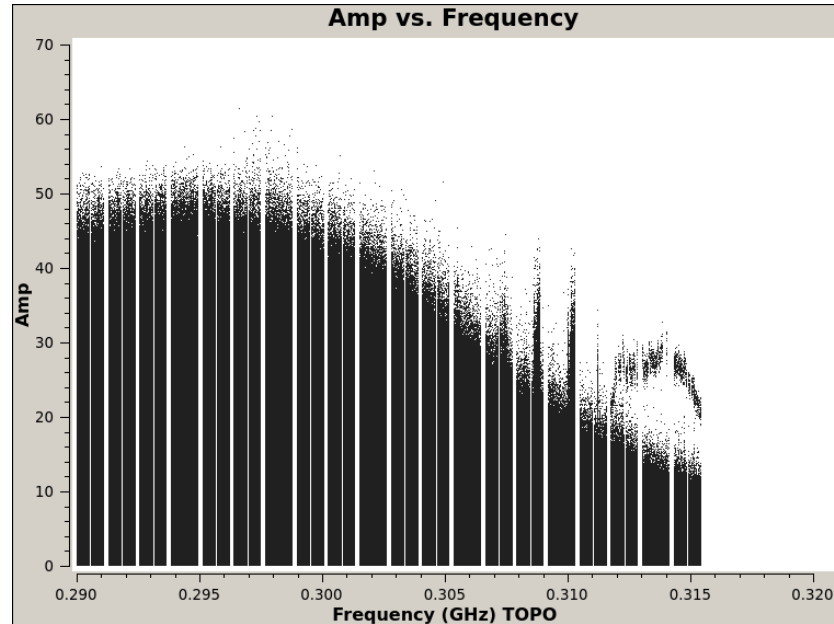
Figure 5.3: Amplitude versus frequency plot for ObsA. This after the flagging strategy in `flag-routine` has been applied to the data. There is a clear improvements, but RFI is still present especially at the higher frequency end of the bandwidth. The scale has changed from the previous Figure 5.1

the MWA 300 MHz observations. There are still some peaks present at higher frequency coarse channels, and some scatter at the highest frequency channels. These show the failures of CASA flagging modes such as TFCROP which is not well suited to flagging broadband RFI. In total after applying the RFI flagging process, in addition to the central and edge fine channels flagged by cotter for each coarse channel, a total of 41.6% of the data was flagged.

Future Work

Future versions of `flag-routine.sh` will allow for reduced flagging times. All of the CASA flagging modes invoked in `flag-routine.sh` require calling a new instance of CASA. Each call to CASA has an overhead loading time. Depending on the number of coarse channels being flagged the number of calls to CASA has a lower limit of 3. Alternatively CASA has a LIST flagging mode which allows for multiple modes of flagging. This means only one instance of CASA will be required to perform all RFI flagging procedures in `flag-routine.sh`. For now the flagging process is relatively quick in comparison to calibration and imaging and typically takes $5 - 10$ minutes to run.

The current flagging options I use for this project are set to CASA default values, and need to be changed manually. In future versions of the script I will consider adding input options for specific CASA FLAGDATA mode parameters. The flagging routine implemented in `flag-routine.sh` is used throughout various data processing stages. For example these stages include calibration and self-calibration. Each time the observational visibility data is processed the script `flag-routine.sh` is run. Each processing step reveals more RFI, which makes it easier to flag.

5.1.2   Observation Download Algorithm

The process of downloading observations, consolidating them into measurement sets, and flagging them for RFI is performed by the script `Obs-download.sh`. The process performed by this bash script is described below:

1. An input Observation list is given. This list is used to submit jobs to the MWA_CLIENT[9]. This client is the PYTHON API which submits jobs to the ASVO server. This operates in a virtual PYTHON environment. This environment remains active along with the script until each of the observation jobs is either downloaded or fails to download.

2. Observations are then unzipped and COTTER is applied to the first observation's raw gpu fits files. This produces a measurement set for that observation. The raw gpu fits files are then removed.

3. `flag-routine.sh` is then called and applied to the observation's measurement set.

4. Steps 2 and 3 are repeated for each observation in the given list.

With the pre-processed measurement sets for observations ready, the apparent sky models for these observations can now be created.

5.2   Building the Apparent Sky Model

After processing and flagging the raw data, the next step is to develop a model of the apparent sky for a given observation. This is simply the true sky multiplied by the MWA tile beam. The model of the apparent sky can be used to predict the visibilities for an observation, and hence be used to determine calibration solutions. I can create these models by using the MWA tile primary beam attenuated by the Total300 sky-model. The MWA 2016 beam model is generated for a given set of azimuth and altitude points (θ, ϕ) for a particular beam pointing. For an observation-specific attenuation pattern this is done by using the python package `mwa_pb`[10]. It is important to note that the beam is zenith normalised. This means that all beam values as a function of (θ, ϕ) are defined relative to the beam value at zenith. So for a zenith pointing the beam value (denoted as B_ν) ranges from zero to one. For observations pointing away from zenith the range will be from zero to greater than one.

5.2.1   Point Source Apparent Sky Model

Before discussing the general method for building the apparent sky model, first we will discuss a simple example where the MWA beam is pointed at zenith, and the sky contains only a single point source located at (θ, ϕ). For this example we consider the instantaneous observation of this source; we do not consider the motion of the point source through the beam. The beam value at the point

---

[9]https://github.com/ICRAR/manta-ray-client
[10]https://github.com/MWATelescope/mwa_pb

sources position will be $B_\nu(\theta, \phi)$, and the true flux density of the source at this frequency is just S_ν. Therefore the source, as viewed by the MWA, will have an apparent flux density given by:

$$S_{\nu,app} = S_\nu B_\nu(\theta, \phi). \tag{5.1}$$

Equation 5.1 is the general representation of the apparent flux density for a single point source and contains within it some important assumptions. For this project I only process snapshot observations which have time duration of 120 s, and I assume the source position is constant. Since the phase centre of the observation is tracked throughout the snapshot I do not assume there is any time smearing for the short integrations scans here of 0.5 seconds. Instead the effect time has on the observation is that the sources rotate through the primary beam pattern. I assume in this project that this effect is negligible and the beam is constant in time at each (θ, ϕ) point. In reality this may be a problematic effect for sources in rapidly changing parts of the primary beam pattern. These fast changing regions usually have high attenuation and should only appreciably affect the brightest sources.

In Chapter 2 we discussed that the flux density of a point source as a function of frequency can be modelled using a simple power law (Equation 2.1). For a fixed (θ, ϕ) we can consider the beam as a function of frequency to also be a simple power law:

$$B_{\theta,\phi}(\nu) = B_{0,\theta,\phi}\left(\frac{\nu}{\nu_0}\right)^{\alpha_b}. \tag{5.2}$$

Both models here are defined at a reference frequency of ν_0, allowing for a simple definition where the product of the two power laws itself is a power law. Hence substituting in Equation 2.1 and Equation 5.2 into Equation 5.1 we get the following apparent sky model for a single point source:

$$S_{app}(\nu) = S_0 B_{0,\theta,\phi}\left(\frac{\nu}{\nu_0}\right)^{\alpha_c+\alpha_b}. \tag{5.3}$$

Or as defined in log-space:

$$\log_{10}(S_{app}(\nu)) = \log_{10}(S_0) + \log_{10}(B_{0,\theta,\phi}) + (\alpha_c + \alpha_b)\log_{10}\left(\frac{\nu}{\nu_0}\right). \tag{5.4}$$

For simplicity we will use the log-space definition. The spectral index for the source here is defined as α_c and the beam spectral index is α_b. Here we see that the beam affects the apparent spectral behaviour. This relatively simple consideration is the one that was applied in the sky-model calibration method at lower frequencies (Franzen et al. in prep). This method describes how the beam and the source behave across the bandwidth for a snapshot observation. This situation gets increasingly more complex when you consider the situation where the log-beam response across the 30.72 MHz can possess curvature.

5.2.2   Curvature in the Log-Beam Response

Radio sources have long been known to show curvature in their SEDs over large frequency ranges (Blundell et al., 1999; Perley & Butler, 2017). Despite the

MWA fractional frequency range being relatively large, intrinsic source curvature across this range is normally negligible (Harvey et al., 2018). Curvature in the apparent flux density through the bandwidth, is therefore primarily the result of the inherent nature of the beam. This curvature is also more significant than the intrinsic source spectral curvature, and its behaviour at a specific (θ, ϕ) has a non-parametric expression. The log-beam response in some (θ, ϕ) points across the sky can vary significantly as a function of frequency. This variation can be complicated in a non-trivial way that cannot be modelled as a simple power law. To demonstrate how problematic this curvature can be, I consider here an example beam spectra at a particular (θ, ϕ) from the aforementioned ObsG23. This observation was chosen instead of ObsA or ObsB because it is pointing closer to zenith, and has several prominent grating lobes unlike ObsA and ObsB. Additionally this observation is scientifically important, since it observes the well documented GAMA 23 field, and along with other additional observations will be further discussed in Chapter 7. Figure 5.4 shows one of the more extreme cases far from the main lobe from a near-zenith observation of the GAMA 23 field. The coarse channels across the bandwidth are shown as blue filled circles, and the dashed lines are various polylogarithmic fits to the coarse channels. The behaviour of the beam shows clear local minima as well as inflections across the bandwidth.

This particular example occurs in a region close to the edges of two sidelobes, so the beam value is small. Exceptionally bright radio sources such as Cygnus A, or Cen A might still be detectable in these regions. Even if these complicated regions are discounted, the log-beam response can still show significant curvature in the main lobe, as well as the grating lobes. Since the beam model only has a frequency resolution of $\nu = 1.28\,\mathrm{MHz}$ the fine channels need to be interpolated (Sokolowski et al., 2017). It is necessary to interpolate the beam effects for the fine channels, since they need to be calibrated for instrumental effects. This can either be done by assuming they have the same beam value as the coarse channel, or by modelling them with a polylogarithmic function. The calibration software CALIBRATE used in this work is capable of accepting higher order polylogarithmic coefficients. Thus it is possible to derive more accurate estimates of the fine channels using this approach. The benefit of this approach is that the beam polylogarithmic coefficients can be linearly combined with the source polylogarithmic coefficients to produce a reliable and accurate apparent sky model.

The goal therefore is to assume that the log-beam response at a fixed (θ, ϕ) can be modelled by an arbitrary polylogarithmic function. This arbitrary form is given below:

$$\log_{10}(B_{\theta,\phi}(\nu)) = \sum_{i=0}^{p} a_i \left(\log_{10}\left(\frac{\nu}{300} \right) \right)^i \tag{5.5}$$

The next task is then determining which order polylogarithmic function p is the most appropriate fit to the coarse channels at a fixed (θ, ϕ). This is a similar situation to the one described in Section 4.1.3.
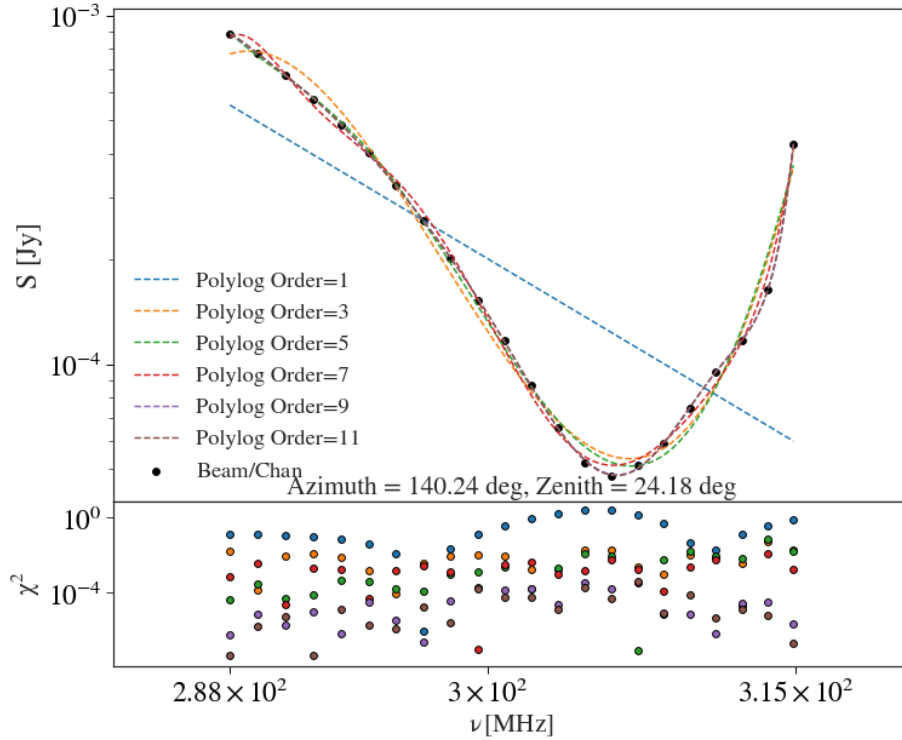
Figure 5.4: One of the more extreme examples of log-beam curvature across the 300 MHz bandwidth. This response has several kinks as well a local minima. This example comes from the observation ObsG23, which is a 300 MHz MWA observation of the GAMA 23 field. This is close to a zenith pointing. This figure additionally shows several polylogarithmic fits to the log-beam curvature. These are represented by the coloured dashed lines. The individual blue points are the coarse channels in the bandwidth. A 9th order polylogarithmic function is the optimal fit to the coarse channels, this is the purple dashed line.

5.2.3 Optimal Order Function

The MWA BEAM2016 primary beam model as discussed in Section 3.3 was derived from a FEKO simulation (Sokolowski et al., 2017). As such errors do not exist for the calculated coarse channels at fixed (θ, ϕ) positions on the sky. Thus the BIC cannot be used as a model fit metric to discern which order best describes the log-beam response. Therefore I was motivated to develop a new metric that behaved in a similar fashion to the BIC, but was applicable to model data without errors. The metric I developed to solve this problem is called the optimal order function (OOF). By construction I designed the optimal order function to be a composite of two functions. The first function is a model-fit metric. For increasing order polylogarithmic fits to the beam, this model-fit metric decreases with order. The second component penalises models that overfit the data. This function increases with increasing order polylogarithmic fits to the beam. The combination of these two functions creates a local minima in the optimal order function. Therefore the minimisation of the optimal order function yields the optimal order fit to the log-beam response for a fixed (θ, ϕ) point in the sky.

Residual Sum of Squares

Since there are no errors the residual squared sum is used instead of using the χ^2 value:

$$RSS(p; \mathbf{x}) = \sum_{i=1}^{N} \big(f(p; x_i) - y_{\text{data}} \big)^2. \tag{5.6}$$

Equation 5.6 has almost the identical form to the χ^2 where $\sigma = 1$, effectively assigning all points with a uniform weight. This function will be kept general in its description, but in this case $f(p; x_i) = B_{\theta,\phi}(p, \nu_i)$. The highest value of p is defined by the number of data points N, where $p_{\text{max}} = N - 1$. A polylogarithmic function of this order can perfectly fit the points, but yields zero information.

As the order of the polylogarithmic function increases the $RSS(p; \mathbf{x}) \to 0$. The $RSS(p; \mathbf{x})$ is only defined for the vector of points $\mathbf{x}$ which has length N. This can have problematic consequences when $p \to N - 1$, especially if the points are uniformly spaced. This is the case for the coarse channels in the log-beam response. In this regime polynomial oscillations between points close to the edges of the bandwidth become apparent. This effect is known as the Runge phenomenon. This makes the interpolation of fine channels between coarse channels unreliable since the oscillation can vary by many orders of magnitude. These are indicative of over fitting the data; thus completely minimising the $RSS(p; \mathbf{x})$ is not desirable in determining the best fitting polylogarithmic order.

Degrees of Freedom

To penalise the over fitting from higher order polylogarithmic functions, an increasing function of the order p is required. This is performed by the term $\ln(n)k$ in the BIC equation 4.2, where $k = p + 1$ is the number of parameters. We compare the number of data points to the degrees of freedom for the fit. The degrees of freedom is defined here as $\text{dof}(p) = N - p - 1$. As the polylogarithmic fit increases, the degrees of freedom decreases. The increasing function takes the squared ratio of the number of data points N to the degrees of freedom, as defined below:

$$h(p) = \left(\frac{N}{N - p - 1} \right)^2 \tag{5.7}$$

Equation 5.7 was squared for consistency with Equation 5.6. Additionally by squaring the ratio the response to higher orders is not linear but quadratic. This makes Equation 5.7 less sensitive to higher order fits, which is preferable because the simplest model should be the best representation of the data.

OOF

I defined the OOF as the square root of the quadrature sum of Equations 5.6 and 5.7:

$$OOF(p; \mathbf{x}) = \sqrt{\left(\frac{RSS(p; \mathbf{x})}{RSS(1; \mathbf{x})} \right)^2 + \left(\frac{h(p)}{h(N - 2)} \right)^2}. \tag{5.8}$$

The components $RSS(p; \mathbf{x})$ and $h(p)$[11] are normalised so they can be added without one component dominating the other across all orders. It should be noted that

---

[11]It should be noted that $h(N - 2) = N^2$

(a) Polynomial Fit Plot   (b) OOF Plot
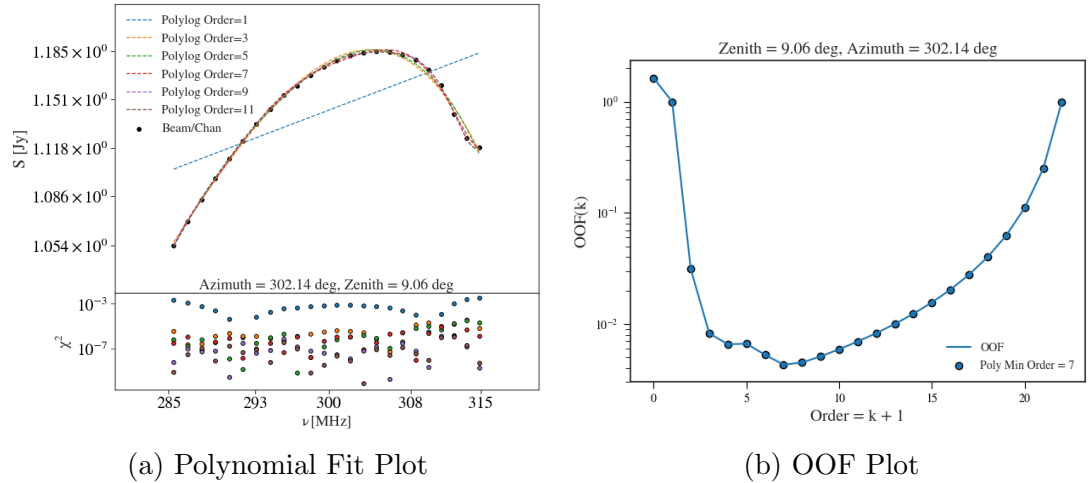
Figure 5.5: An example log-beam response for a zenith pointed observation. Here this fixed (θ, ϕ) point is located in the main lobe of the observation, and the Azimuth and Zenith values are given in the plot title. Like other plots of this format the blue filled circles are the coarse channels, and the coloured dashed lines are the polylogarithmic fits of increasing odd order. The residuals for the fit are given in the bottom panel which are colour coded according to their fit. The OOF plot for the polylogarithmic fits in Subfigure (a) is given in Subfigure (b). There is a clear minimum in Subfigure (b) at a polylogarithmic order of $p = 7$.

the normalisation of both of these functions is somewhat arbitrary. The choice of normalisation is what defines where the likely location of the OOF minimum occurs. For the $RSS(p; \mathbf{x})$ I chose the $RSS(1; \mathbf{x})$ for the first order polylogarithmic function. This is a power law in normal space, as previously specified. This choice is a logical one since the power law model is the base case of consideration for the beam model at fixed (θ, ϕ). Therefore it is natural to compare all higher order model $RSS(p; \mathbf{x})$ values to the first order polylogarithmic one $RSS(1; \mathbf{x})$. The normalisation for the function $h(p)$ is the order $p = N - 2$. This is the second highest order fit possible to the data. Since the highest order fit results in a singularity for the function $h(p)$ the second highest order fit was chosen. This stops the function $h(p)$ from dominating at lower orders.

Example:

An example of the polylogarithmic fits to a single point, and the OOF function, for a zenith pointed observation ObsZen can be found in Figure 5.5. In Subfigure 5.5a a fixed point located in the main lobe of the observation is represented with the same format as in Figure 5.4. This shows a more well behaved log-beam response than that found in Figure 5.4. This is expected because the primary beam response across the bandwidth in the main lobe, does not change as rapidly in than regions in between sidelobes. The second Subfigure 5.5b shows the OOF plot for the polylogarithmic fits in Subfigure 5.5a. Here the order that minimises the OOF is clearly found at $p = 7$, but $p = 6, 8$ also show good fits.

Figure 5.6 shows four Subfigures. The first two Subfigures 5.6a and 5.6b show the primary beam pattern of the first coarse channel at $285\,\mathrm{MHz}$ and the last

(a) 285 MHz Primary Beam (S_{315})

(b) 315 MHz Primary Beam (S_{315})

(c) $S_{315} - S_{285}$

(d) Polar Order
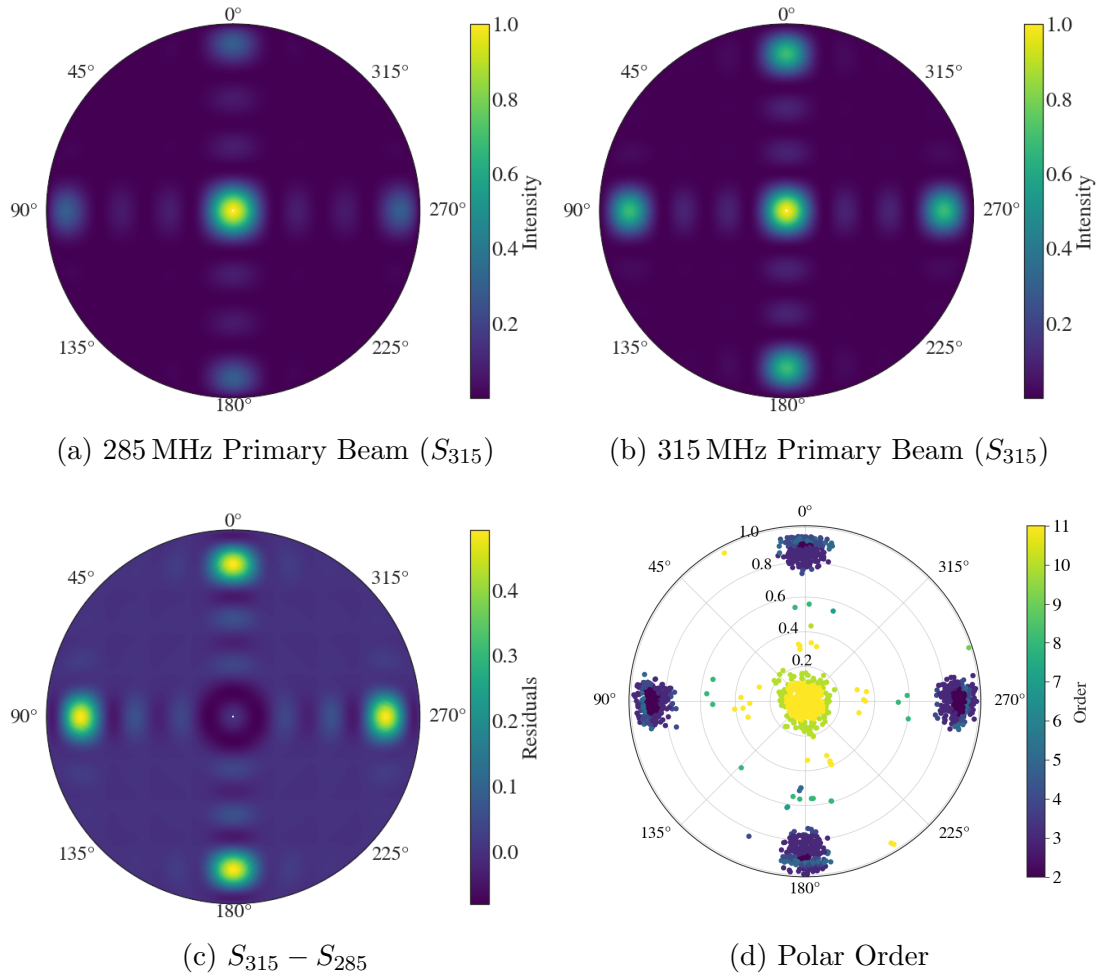
Figure 5.6: Subfigure (a) is the primary beam pattern for the 285 MHz coarse channel for ObsZen. Subfigure (b) is the primary beam pattern for the 315 MHz coarse channel for ObsZen. Both primary beam patterns were generated by the BEAM2016 model. The difference between the high and low coarse band primary beam patterns can be seen in Subfigure (c). Subfigure (d) shows the optimal order found by minimising the OOF for the brightest 1500 sources in the ObsZen apparent sky-model.

coarse channel at 315 MHz of the 300 MHz bandwidth. These two Subfigures are set to the same intensity scale, and the primary beam patterns were generated using the BEAM2016 model. It is clearly visible that the grating lobes are more prominent at the 315 MHz coarse channel than at the lower 285 MHz coarse channel. The difference between the highest and lowest coarse channels is displayed in Subfigure 5.6c. Subfigure 5.6c clearly shows the most rapid change occurs in the grating sidelobes. The last Subfigure 5.6d shows the optimal order determined by minimising the OOF for the brightest 1500 sources, in the zenith pointed MWA observation ObsZen. The colour bar indicates the optimal order polylogarithmic fit for each source. Clearly the grating sidelobes prefer lower order polylogarithmic fits than the main lobe, which prefers high order polylogarithmic fits. At first this appears counter intuitive, but referring back to Subfigure 5.5a there is a visible upturn towards the higher coarse channels. After observing hundreds of polylogarithmic plots similar to Figure 5.5a, this upturn is a common feature in the log-beam response across the main lobe. This occurs as the size of the main lobe reduces at higher frequencies and migrates inwards towards zenith. This creates a small local minimum across the log-beam response for points in the main lobe. These minima are not trivially fit by lower order polylogarithmic functions. In comparison, although the grating sidelobes experience the greatest change in intensity, the change in the log-beam response as a function of coarse channel is relatively constant. For the grating lobes this change is better described by lower order polylogarithmic functions, and can be reasonably fit in many cases by a power law with a steep spectral index.

OOF Summary

The OOF function as well as the polylogarithmic fitting routines that I defined are written in the python file `JOOF.py`. This is an importable python file that fits arbitrary order polynomials. It is capable of fitting the BIC as well as the OOF depending on whether errors are given for the data. It is also implemented for parallel polynomial fitting to reduce the time overhead; for example, fitting increasing order polylogarithmic functions to 1500 sources takes ~ 20 seconds for my laptop's 4-core 8th generation i5 Intel CPU.

Once the optimal polylogarithmic order fit is determined for the log-beam response, the coefficients for that fit are saved in an array for each source. This array of coefficients is output by `JOOF.py` and can be linearly combined with the Total300 source coefficients. In the appendix Section A.1 a method is presented to transform coefficients between reference frequencies, because the log-beam response is fitted relative to the centre of the 300 MHz bandwidth, and a common frame is required.

5.2.4 Observation Apparent Sky Algorithm

The process described in this Section is performed by the bash script `build-app-sky.sh`. This takes in the OBSID, and the Total300 sky model as input. This script then outputs an apparent sky catalogue, as well as a text file in a format readable by CALIBRATE. The step by step process is:

1. The total 300 MHz sky-model is subsetted for all sources above the horizon for the OBSID.

2. The 2016 beam model value B_ν is then determined at the central frequency for all sources above the horizon. This is then multiplied by the flux density of all of those sources. The brightest 1500 sources are selected.

3. The primary beam model for each coarse channel is generated for each fixed (θ, ϕ) value for all 1500 sources. The OOF is then determined for each of these sources, and the coefficients are outputted in an array. These beam coefficients are then added to the source coefficients for each source.

4. These sources are then written to a VOTable[12], with the apparent flux densities and apparent coefficients.

5. This table is then passed to the python script `vo2newmodel.py` which outputs a text file in a format readable by CALIBRATE. Here sources are separated into two categories; points sources and extended sources. Extended sources are those that have major axis values larger than the resolution (PSF major axis) of the observation. Since the local PSF for each source is not given in the original PUMA catalogue, the PSF at 300 MHz is estimated by scaling the Zenith PSF of the GLEAM extra-galactic first data release 200 MHz wideband image (Hurley-Walker et al., 2017). Sources with Major axis values larger than the estimated PSF are classified as Gaussian[13]. For all sources the RA, DEC, integrated flux density and the apparent coefficients are formatted. For the Gaussian sources the major, minor axes as well as the position angle are also formatted. CALIBRATE can accept and read both point source and Gaussian models.

An example can be seen in Figure 5.7 which shows the apparent sky model for the Pic A observation A. It is in a sine projected sky map, where the colour bar is the apparent flux for the 1500 brightest sources. The main lobe is located between declinations -60 deg and -30 deg, where Pic A (the large filled red circle) is visible near the centre. The prominent grating lobe can be seen close to a declination of 0 deg. Additionally two other grating lobes at a declination of -30 deg can be seen close to the horizon. With this model in hand it is now possible to calibrate observation A.

5.3   Calibrating the Observation

With an apparent sky-model it is now possible to apply the calibration method I discussed in Chapter 2 and implemented by Offringa et al. (2016) in the software CALIBRATE. Figure 5.8 shows a subset of tile phase versus frequency solutions for ObsA. The two components of the Stokes I (XX and YY) components are

---

[12]Virtual Observatory Table (VOTable) is a flexible format that makes use of the XML standard, which creates scalable and interoperable data. This is a common data format used by astronomers (Ochsenbein & Williams, 2009)

[13]In future this will consider the ratio of the integrated and peak flux densities as additional criteria.
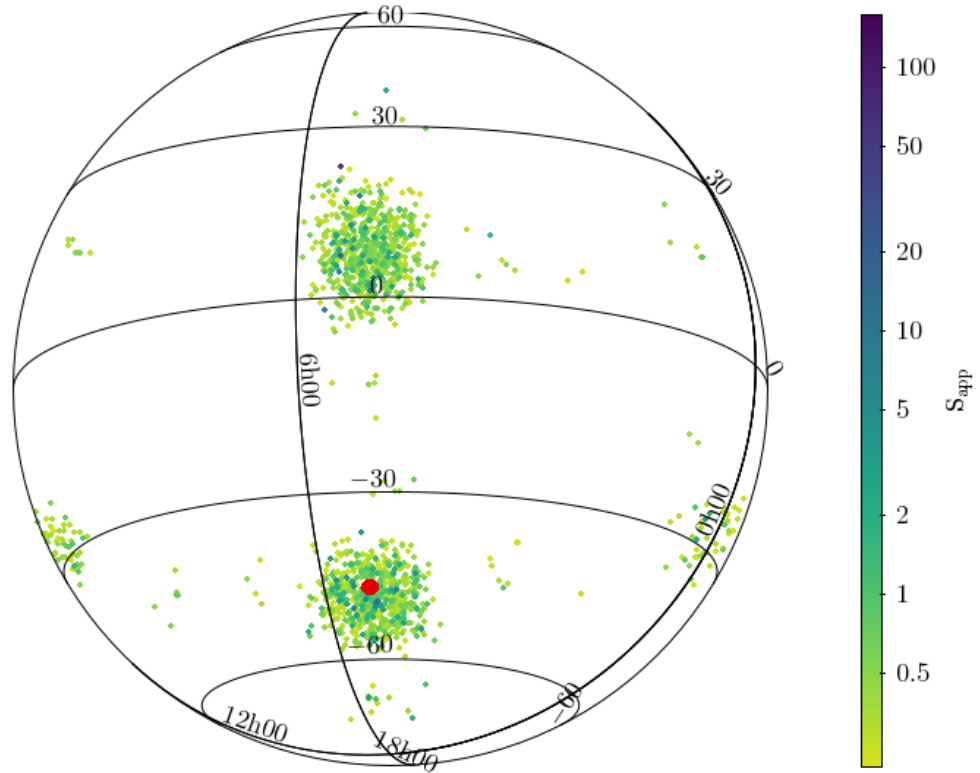
Figure 5.7: Sine projected map of the apparent sky model for ObsA. The colour bar is a log level of the apparent flux density for each of the brightest 1500 sources in the apparent sky model. The main lobe is present at low declination between -60 deg and -30 deg. The most prominent grating lobe is visible at declinations above 0 deg, and the lesser grating lobes are close to the horizon at declinations close to -30 deg. Pic A can be seen as the large filled red circle near the centre of the main lobe. Additional bright sources such as the Crab Nebula are visible towards the top of the prominent grating lobe. This models what we should expect to see for the whole sky with this observation.

shown in red and blue. Each of the points represents a different fine channel, where notably the missing chunk corresponds to flagged coarse channels. The phase solutions are stable with some scatter, which could be partially explained by the presence of RFI.

The amplitude versus frequency for the corrected data for all tiles can be found in Figure 5.9. In this Figure we see that there is still a lot of RFI present, and it is more apparent after calibration. In Figure 5.3 the first four coarse channels were flagged, but in Figure 5.9 only the first three have been flagged. This is to show the enormous amount of RFI contamination in the lower coarse channels. The effect of this is more pronounced in the corrected data. The corrected data are flagged using the script `flag-routine.sh` with the same parameters as for the uncorrected data. The resulting flagged corrected data are shown in Figure 5.10.

Here the fourth coarse channel is also flagged since it was highly contaminated with RFI[14]. There is an enormous improvement in the corrected solutions over the original corrected solutions. This improvement is seen in how the scale have

---

[14]Most MWA snapshot observations at 300 MHz have the first four coarse channels flagged
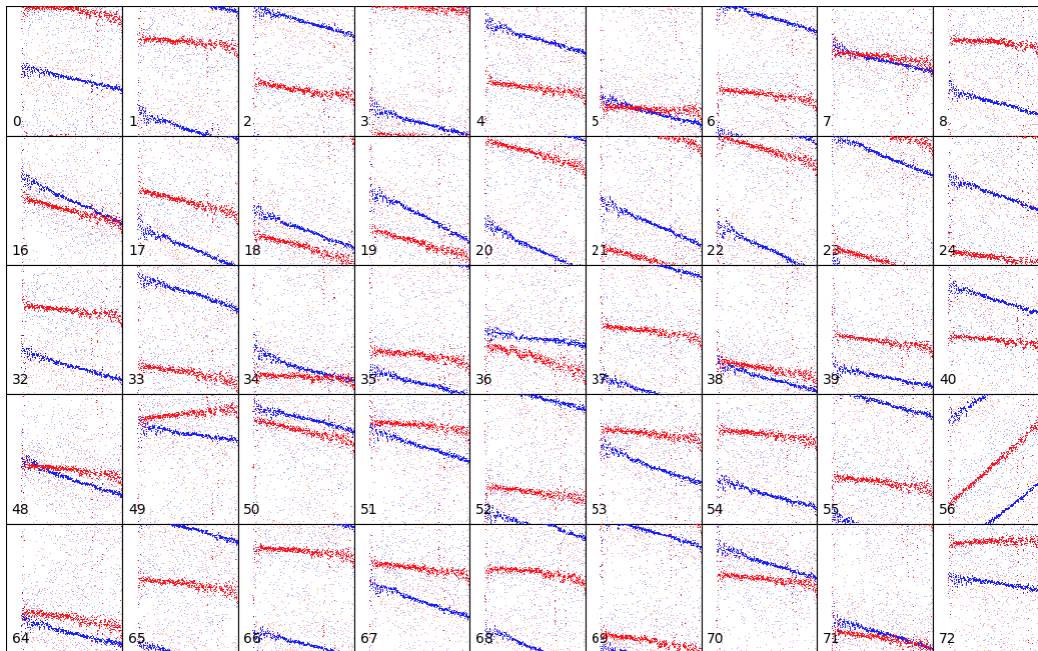
Figure 5.8: Phase (vertical) versus frequency (horizontal axis) plots for observation A of Pic A. This plot shows the full bandwidth of the observations, where each point is a single fine channel, and the fine channels of each tile are plotted. The red and blue lines are the Stokes I (XX) and (YY) polarisations for each dipole. Here we show the phase versus frequency plots for 45/128 tiles. The edges of each coarse channel are flagged due to aliasing effects as well as the centre of each coarse channel. RFI spikes are clearly present at multiple subbands across the full bandwidth.

been readjusted by several orders of magnitude. Here 47.94% of the total data has been flagged at this stage. There is still some RFI present in some of the bands. This will be further flagged in later processing Sections.

5.3.1   Observation Calibration Algorithm

This calibration strategy is encapsulated in the bash script `cal.sh`, the process for calibrating the data is described below:

1. Take the input sky-model format text document and observation measurement set.

2. Run CALIBRATE with the sky-model format text document to correct the observation measurement set.

3. Apply the calibration solutions to the measurement set. This creates a new corrected data column in the observation measurement set. This is done using the software APPLYSOLUTIONS. This is complimentary software that comes with CALIBRATE

4. Apply `flag-routine.sh` to the corrected data column of the measurement set. RFI should be more pronounced after calibration making it easier to flag.

---

as a default setting due to the consistent presence or RFI at these frequencies.
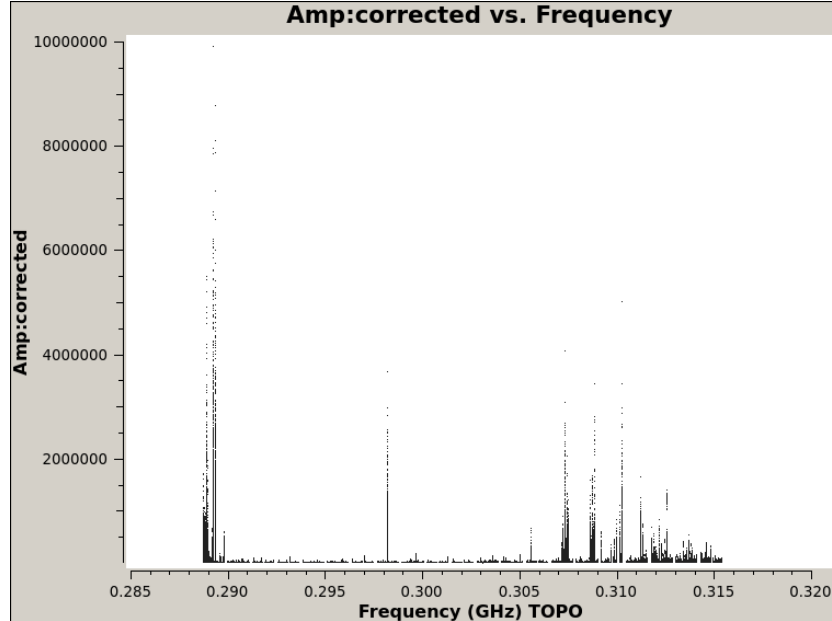
Figure 5.9: Corrected amplitude versus frequency plot for ObsA. This plot shows the full bandwidth of the observations, where each point is a single fine channel, and the fine channels of each tile are plotted. The edges of each coarse channel are flagged due to aliasing effects as well as the centre of each coarse channel. RFI spikes are clearly present at multiple subbands across the full bandwidth.

5.4 Self-Calibration & All-Sky Imaging With the MWA

With decent calibration solutions for ObsA, it is now possible to perform imaging. Since the sensitivity of the beam at these higher MWA frequencies is not limited to the PB, the visibilities contain significant information from the rest of the sky. Therefore the whole sky needs to be imaged. Imaging an observation is not simply applying an inverse Fourier transform to acquire the sky brightness map $I(l, m)$. The true sky is actually convolved with the point spread function (PSF) of the array $S(l, m)$ which is the Fourier transform of the baseline sampling. This convolution gives the dirty image $I^D(l, m)$:

$$I^D(l, m) = S(l, m) \otimes I(l, m). \tag{5.9}$$

The PSF has sidelobes which add noise to the background this is commonly referred to as sidelobe confusion. As a result deconvolution is an important step in removing the sidelobes and reducing the noise in the image. To deconvolve the PSF and acquire the true sky brightness, deconvolution algorithms such as CLEAN can be applied (Högbom, 1974). In a simple treatment, the basic CLEAN algorithm treats the sky as a collection of point sources, where these point sources are convolved with the PSF. It then iteratively subtracts a portion of the PSF from the brightest point sources in the image domain. The subtracted points are kept in a model image, and the residuals of the subtraction are stored in a residual image. This process is repeated until a specific threshold is reached, this threshold is usually some SNR above the rms noise. The model image points are then convolved with a Gaussian beam that has been fitted to the PSF. The
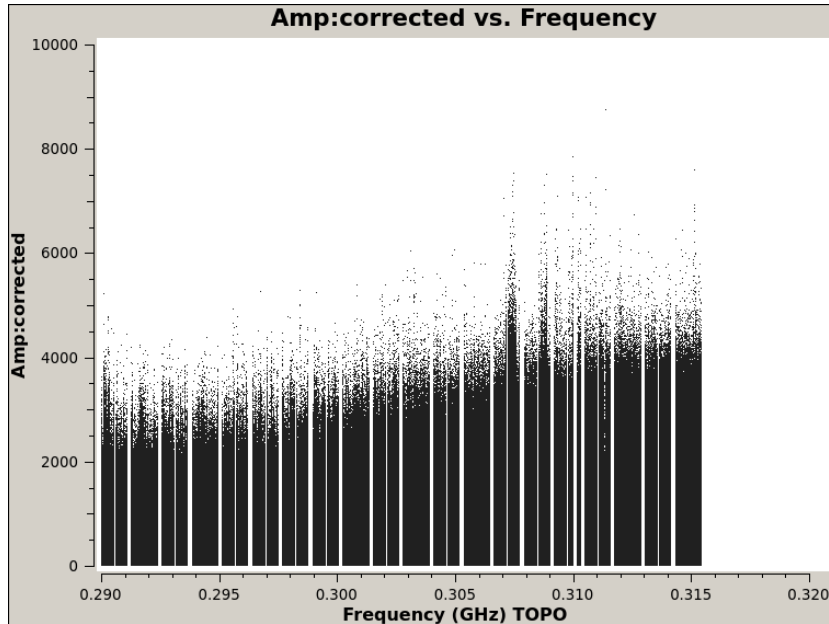
Figure 5.10: Corrected amplitude versus frequency plot for ObsA. This data has been filtered using `flag-routine.sh`. This plot shows the full bandwidth of the observations, where each point is a single fine channel, and the fine channels of each tile are plotted. The edges of each coarse channel are flagged due to aliasing effects as well as the centre of each coarse channel. RFI spikes are clearly present at multiple subbands across the full bandwidth.

residuals are then added to the model image, and the resulting product is the cleaned image

As mentioned in Chapter 2 arrays with wide fields of view cannot ignore the w-terms. The incorporation of the w-terms in the image processing makes the deconvolution process more complicated. In Section 2.2 I mentioned there are several methods to deal with the incorporation of the w-terms. In particular the w-stacking method which is used by the imaging and deconvolution software WSCLEAN[15], is widely used to image MWA observations, and as such is used in this thesis (Offringa et al., 2014).

W-Stacking

In Chapter 2 I introduced the visibility Equation 2.6 for a particular baseline projection. I then discussed Equation 2.7 which considered the Fourier transform of Equation 2.6 in the limit where the w-terms are negligible. The resulting Fourier transform retrieved the sky brightness $I(l, m)$ attenuated by the primary beam pattern $B(l, m)$ with additional denominator term $\sqrt{1 - l^2 - m^2}$ (which can be subsumed into the primary beam term). Considering instead the Fourier transform of Equation 2.6 in the regime where the w-terms are not negligible, we retrieve an expression similar to Equation 2.7 but which incorporates the w-terms:

$$\frac{B(l,m)I(l,m)}{\sqrt{1-l^2-m^2}} = e^{-2\pi i w \left(\sqrt{1-l^2-m^2}-1\right)} \int_{-\infty}^{\infty} \int_{-\infty}^{\infty} \mathcal{V}(u,v,w)$$
$$\times e^{2\pi i (ul+vm)} du\, dv. \tag{5.10}$$

---

[15]https://sourceforge.net/p/wsclean/wiki/Installation/

We can then integrate both sides of Equation 5.10, this results in a practically useable form given below:

$$
\frac{B(l,m)I(l,m)(w_{\max}-w_{\min})}{\sqrt{1-l^2-m^2}} = \int_{w_{\min}}^{w_{\max}} e^{-2\pi i w\left(\sqrt{1-l^2-m^2}-1\right)} \int_{-\infty}^{\infty} \int_{-\infty}^{\infty} \mathcal{V}(u,v,w)
$$
$$
\times\, e^{2\pi i(ul+vm)} du\, dv\, dw.
$$

(5.11)

With Equation 5.11 the variables u, v, and w can be made discrete. This converts the Fourier transform of the visibilities with respect to the variables u, and v into a Fast Fourier Transform (FFT). The integral over the w-terms also reduces to a summation. This is similar to the case where w-terms can be ignored, where in this situation the FFT is computed for each w-layer. The FFT results of each layer are then summed together to produce the right hand side of Equation 5.11. This is essentially the method employed by Offringa et al. (2014) to deal with the w-terms. For further details on the technical aspects of the software refer to the paper (Offringa et al., 2014).

5.4.1 All-Sky Images

To create the all-sky image I had to phase-shift the visibilities to a zenith phase centre. This is done for two reasons, firstly this reduces the number of w-terms required to create the image, and secondly this allows for creating a symmetric all-sky image. A similar process for creating all-sky images is described in Offringa et al. (2014). The visibilities were phase shifted using the software CHGCENTRE[16] with the option `-zenith`. This software is available with the WSCLEAN software in the given SourceForge link. Once the phase centre of the visibilities has been shifted they can be imaged after a shallow clean has been performed. The image size I chose was 7000×7000 pixels. This allowed for a pixel scale of 59 arcsec, where the visibilities were Gaussian tapered for a PSF of size 2.4 arcmin. This meant that the PSF was sampled over approximately 2.5 pixels. The PSF was under sampled due to computational memory constraints on processing large images. Additionally the all-sky imaging step is primarily used for self-calibration not for science, higher resolution images are made later in Chapter 6. The weighting I applied for the all-sky imaging was a uniform weighting; natural weighting only increased the size of the PSF. Additionally, baselines shorter than 60 m were flagged. These baselines are sensitive to large scale diffuse synchrotron emission which is difficult to clean. I imaged the full bandwidth, and only the Stokes I images were output. Cutouts of the resulting all-sky image can be seen in Figure 5.11, where only the main lobe and prominent grating lobe (DEC > +0) are shown. The full image is very large and it is difficult to see individual sources, there is also striping due to remaining RFI.

Subfigure 5.11a shows the main lobe of ObsA where Pic A is at the centre. The main lobe has an rms flux density of 86 mJy/beam. There are large PSF sidelobes still present, due to the fact that Pic A has not been fully cleaned. Only a shallow clean was applied for the all-sky imaging. The large sidelobes and RFI are most likely responsible for the high noise level. In comparison the expected noise level

---

[16]https://sourceforge.net/p/wsclean/wiki/Installation/
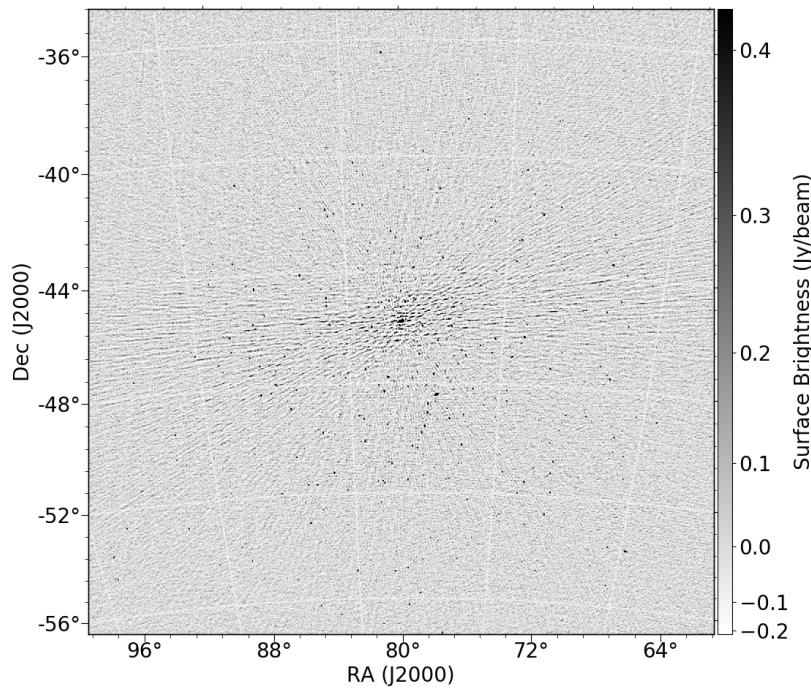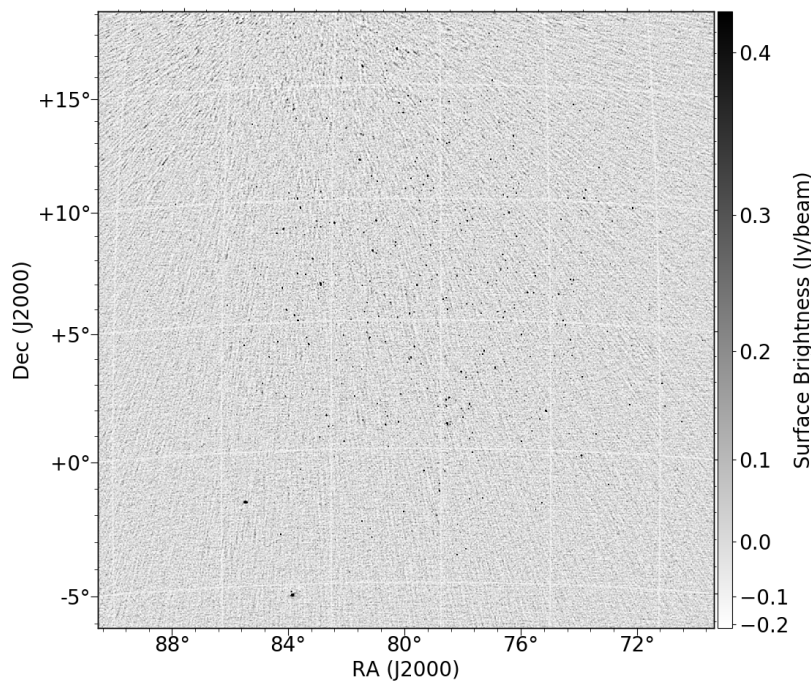
(a) ObsA Main Lobe

(b) ObsA Grating Lobe

Figure 5.11: The all-sky image of the Pic A observation ObsA was split into two main regions. The first region is the main lobe centred at RAJ2000 = 79.95 deg, DEJ2000 = −45.79deg with an rms of 86 mJy. The second region is the most prominent grating lobe centred at RAJ2000 = 79.95 deg, DEJ2000 = 5.00deg with an rms of 68 mJy. There are additional grating lobes to the left and right of the main lobe which contain additional sources. Since the projection of this observation is significantly away from zenith it these grating lobes are not as prominent as the second grating lobe. As such they were not included.

for naturally weighted visibilities determined from the radiometer equation in Section B.2 is 25 mJy/beam. This expected noise level (with assumed T_{sys} and A_{eff} see Appendix B.2) accounts for the flagged data. This is the best theoretical sensitivity that can be achieved with the available set of data. [17]

Subfigure 5.11b shows the prominent grating lobe which has a flux density rms of 68 mJy/beam. The sidelobe artefacts present in the top of the image originate from the Crab Nebula, which is located above the top edge of the image. To the south of the grating lobe is the Orion Nebula which can be seen as the diffuse bright blob. There are additional regions and less prominent grating lobes but these are not shown. Many sources are clearly present in the shown regions. Importantly only the apparent images are shown; these have not been primary beam corrected. The reason for this is the all-sky image contains pixels which do not map to the sky, and these are essentially just noise. The absolute beam values determined for these pixels are many orders of magnitude higher than what is found in the sky. As a result the global intensity scale of the all-sky image becomes biased towards very large absolute numbers at both ends of the intensity scale. This makes it difficult to see anything in the actual image apart from scaled noise.

Once the all-sky image is made, WSCLEAN adds a model column to the observation measurement set. This column is the visibilities of the CLEAN components. Essentially the CLEAN components form a sky-model. The self-calibration process as applied by CALIBRATE, uses this new model set of visibilities as a new apparent sky-model that reflects the actual distribution of apparent flux density in the observation. This then applies the same sky-model calibration process as described in Chapter 2. Generally this does provide better calibration solutions, but this can introduce systematics in regards to the phase offset and flux density scale. The new calibration solutions are then applied with the software APPLYSOLUTIONS. These yield similar solutions to the previous calibration solutions in Figure 5.8 but with less variation. Additionally the RFI flagging routine is applied again to catch any RFI and outliers[18] that might still be present.

5.4.2 Observation Self-Cal Algorithm

This method of self-calibration is implemented in the bash script `selfcal.sh`. The process applied in this script is described below:

1. Takes the input corrected measurement set, calls CHGCENTRE to change the phase centre to zenith.

2. Once the phase centre has been changed, WSCLEAN is called and an all-sky image is produced.

---

[17]There are some caveats here. Primarily the weightings applied to the all-sky images scale the naturally weighted sensitivity estimate by the ratio of the mean weight to the rms weight. This is covered in Section B.2. The proper estimation is performed by WSCLEAN but these values were not recorded. Reprocessing of the data would be required to retrieve these values, and the pipeline has since changed.

[18]Failed calibration solutions for some fine channels can also introduce extreme outliers in the data.

3. Once the all-sky image is made CALIBRATE is run with the new model column to generate the new corrected solutions. These are then applied to the data using APPLYSOLUTIONS.

4. The new corrected data are then further flagged for RFI using the bash script `flag-routine.sh`. Resulting amplitude versus frequency plots for each MWA tile is then produced.

5.5   Transferring Calibration Solutions

For some observations which are not dominated by a bright (10's to 1000's of Janksy's) partially resolved or unresolved calibrators like Pic A, it may not be possible to employ the sky-model calibration approach directly. This is especially the case when considering the compounding effects of low signal to noise in the fine channels across the bandwidth, inaccuracies in the fit to some source SED's, inaccuracies in the primary beam model, and the pernicious effect of RFI. The effects of the latter in particular can be hard to separate until the data are actually calibrated. In these cases transferring calibration solutions from observations like ObsA where there is a bright calibrator at the same pointing may be the best strategy. Importantly this strategy hinges on the assumption that the DDE effects of the ionosphere are stable over the course of the night. This calibration solution transfer strategy was employed to calibrate ObsB which was taken at the same night and with the same pointing as ObsA. Calibration solutions from ObsA were applied to ObsB by using APPLYSOLUTIONS. This process is encapsulated in the bash script `cal-transfer.sh`. After transferring the calibration solutions an all-sky image for ObsB was produced and this can be seen in Figure 5.12. This is the same format as Figure 5.11. The rms in Subfigure 5.12b is 48 mJy compared to an rms of 44 mJy in the main lobe image as shown in Subfigure 5.12a. These are both lower than their calibrator observation counterparts. This could in part be due to Pic A sidelobe noise being less dominant since it is close to a sidelobe minima.

After all-sky imaging self-calibration can be performed on these types of observations, but in general it is not recommended. Since CALIBRATE treats each fine channel independently, for observations like ObsB with relatively low amounts of apparent flux density, the signal to noise for each fine channel may be too low to constrain the gain amplitude and phase solutions. This can lead to worse calibration solutions than the transferred ones. In these cases instead of performing self-calibration on these observations, it is recommended that only the self-calibrated solutions, or calibration solutions from a calibrator observation (in this case ObsA) be used.

5.6   Summary

In this Chapter two calibration methods are presented. The first method applies sky-model calibration to an observation of a bright calibrator source such as Pic A. This was shown to be possible and could be improved with self calibration after all-sky imaging. The second method was for observations not dominated by
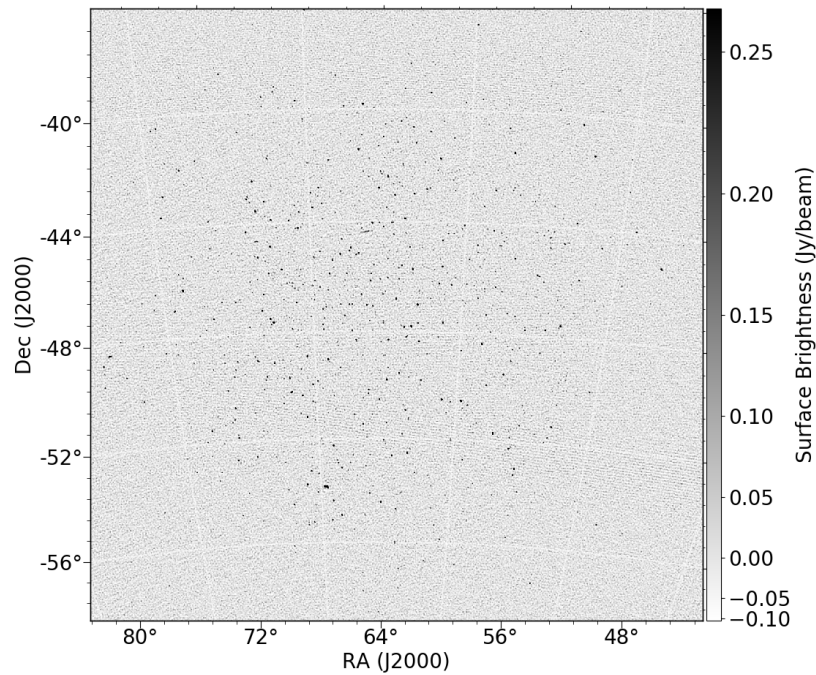
(a) ObsB Main Lobe
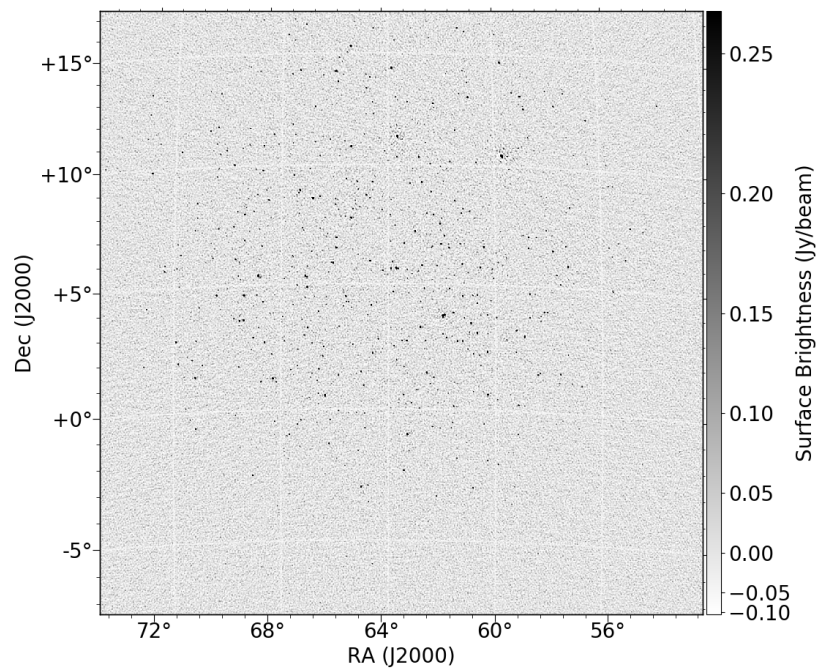
(b) ObsB Grating Lobe

Figure 5.12: For simplicity the all-sky image of ObsB was split into two main regions. The first region is the main lobe centred at RAJ2000 = 63.3 deg, DEJ2000 = −47.38 deg, the second region is the most prominent grating lobe centred at RAJ2000 = 63.3 deg, DEJ2000 = 3.8 deg. There are additional grating lobes to the left and right of the main lobe which contain additional sources. Since the projection of this observation is significantly away from zenith it these grating lobes are not as prominent as the second grating lobe. As such they were not included.

a bright calibrator source. This method was to transfer calibration solutions from the calibrator observation. This was shown to work also, but this method only works with observations at the same pointing. In Hurley-Walker et al. (2017) they mention that to transfer calibration solutions to different pointings, a normalisation needs to be applied since the beam is normalised to zenith for the different pointing. This lack of normalisation could explain the difference in the image rms values for ObsA and ObsB. This method could be tried in future work. Both methods are affected by RFI, where an RFI flagging strategy was developed to reduce the effect of the RFI. It was found that RFI flagging had to be performed at each processing step to get the best results. With corrected data the next challenge is making a deep image of the main lobe. This will involve removing the contribution of the other parts of the sky.

Chapter 6

Imaging Strategy

In this Chapter I use the model generated from the deconvolution process (clean) in Chapter 5 to subtract away the sources from the grating sidelobe regions. This subtraction process attempts to remove the contribution the grating sidelobes have to the observation visibilities. As a result the sidelobe confusion noise in the final image is reduced and the dynamic range in the main lobe is increased.

The clean components generated from the all-sky imaging are stored in a model image as output from WSCLEAN. The main lobe, or any region of interest for imaging can be masked from the all-sky model image. This then leaves a model image of the rest of the sky minus the main lobe. WSCLEAN can then be used to predict the visibilities of this masked model image through a Fourier transform. These visibilities are then saved by WSCLEAN to the model column of the observation measurement set. Once here they can be subtracted from the corrected data column, in theory leaving only the masked regions' contributions to the visibilities.

Before I can subtract the masked model images from the observation visibilities there are some pre-processing steps that need to be accomplished. First the centre and size of the main lobe have to be determined. I discuss the generalised algorithm for this approach in Section 6.1. Once the lobes have been identified, the main lobe needs to be subsetted from the model image. I describe this process in Section 6.2. Section 6.3 describes the iterative sky-model subtraction. In Section 6.4 I detail the deep imaging and the results as applied to the example observations. As in the previous Chapters there are two example MWA observations at 300 MHz. To review, the first observation ObsA is dominated by the calibrator source Pic A; the second observation ObsB is taken from the same night and at the same pointing as the Pic A observation. This observation is not dominated by any exceptionally bright sources.

6.1   Lobe-Finder Algorithm

In order to subset the model image and subtract the sky from the visibilities, I created an algorithm that generically identifies the centre and size of lobes in an apparent sky model. This algorithm is encapsulated in the PYTHON script `lobe-finder.py`, this script is available along with the other scripts in this work

at the github repository S300-PIPELINE[1]. This script works with any model of the apparent sky for a particular observation.

Chapter 4 describes the apparent-sky model created from the Total300 sky-model and the 2016 MWA tile beam model. This model of the apparent-sky is a prediction used to create a first pass calibration for 300 MHz MWA observations. The apparent-sky model of interest for the lobe-finding algorithm is one made from all-sky images I created for ObsA and ObsB in Chapter 5. Apparent-sky models constructed from all-sky images can be made by applying a source finding algorithm to the image. Source finding algorithms identify the RA and DEC of potential radio sources, and measure their flux densities. Apparent-sky models generated from the images themselves are useful because they reveal the locations of measured apparent flux density in the sky. Thus the lobe-finding algorithm can be applied to a model of the real data not a prediction of what we would expect to see.

The source finder AEGEAN as described in Hancock et al. (2012) and Hancock et al. (2018) was used to develop these updated apparent sky models. This algorithm determines the background and rms across the image. These are stored in images that match the input image dimensions. It then finds pixels that deviate significantly away from the background. Groups of pixels are identified in structures called islands. These islands are then fitted with two dimensional Gaussians. This process then outputs the integrated total flux density, the peak flux, the semi minor and semi major axes of the Gaussian fit, and the position angle of the fitted Gaussian. The output of this data can be specified in a FITS[2] table format similar to the structure of Total300 catalogue.

There are two important considerations that should be mentioned in relation to AEGEAN. The first is that it is not sensitive to large scale diffuse radio emission. So sources with extended profiles like Fornax A may not be detected or properly fitted. This means that the sky is assumed to be a collection of point sources and Gaussian blobs. The second consideration is the more important one. Here I use the uncorrected all-sky images. The source finder is usually applied to a corrected image. Since I have imaged the whole sky, regions in which there are minima between sidelobes create discontinuities in the rms maps produced by AEGEAN. This can lead to AEGEAN incorrectly identifying noise peaks in these minima regions as sources. However this is not important for the lobe finding algorithm, since I only want to know where approximately most of the apparent flux density is. So in this case AEGEAN is a useful tool for determining where most of the apparent flux density is located on the sky.

---

[1]https://github.com/JaidenCook/300-MHz-Pipeline-Scripts

[2]The Flexible Image Transport System (FITS) is a common digital file format designed specifically for Astronomy. The file format allows for data to be formatted in multi-dimensional arrays as well as tables. This makes it useful for storing, transmitting and processing astronomical data. The FITS metadata is highly flexible, and can contain information on the table or image, including the image world coordinate system, and/or the spectral information. This can be the image astronomical coordinate origin, spectral information for example (Wells et al., 1981).

6.1.1 Lobe Centre and Size Determination

Before I can identify the grating sidelobes the main lobe needs to be removed from the data. This is more important in the case of observations close to a zenith pointing[3]. The method for determining the size and centre of the main lobe is the same as that used for the grating sidelobes. So I will discuss this sub-routine first before the method used to determine the grating sidelobe positions.

The script `lobe-finder.py` requires input in the form of the observations metafits file, and the source catalogue determined from AEGEAN. The metafits file contains information on the pointing RA and DEC for the centre of the observation. This corresponds to the preliminary centre of the main lobe. I also use the OBSID to determine the Altitude and Azimuth for each of the sources in the source catalogue. This allows for the projection of these sources onto a polar plot, where the Altitude is transformed to a radius value through $r = \cos(\theta_{\mathrm{alt}})$. The lobe finding algorithm operates in the polar projected space.

Once the data have been transformed into a polar projection, the size and adjusted main lobe centre is determined using the method outlined below:

1. Draw a circle of radius $R = 0.1$ around the preliminary lobe centre. Determine the number of sources within the circle.

2. Iterate this process again. This time the circle radius has grown by $\delta r = 0.01$. Count the number of sources within the circle. If the number of sources has increased from the previous iteration repeat this process. If the number of sources is the same as the previous iteration, the loop stops. These sources are then subsetted from the main catalogue.

3. The centre of mass RA and DEC for the subsetted sources is determined. This is the centre of the identified lobe.

4. Using the max RA and DEC for these sources the algorithm then determines the size of the subsetted region using the Haversine formula[4].

5. Store the lobe size in degrees, the number of lobe sources, the RA and DEC centre in degrees and hh:mm:ss±dd:mm:ss format in a python dictionary.

I employ this same method for identifying the size and centre of other lobe regions. A special case should be noted for lobes that are identified at the wrapping boundary of the polar plot where $\theta = 0 = 2\pi$. In order to properly determine the size and the centre of these lobes, I perform a coordinate transform which reflects the sources in that lobe into the polar segment $\theta \in [\pi/2, 3\pi/2]$. The same calculations to determine the size and the centre of the lobe are performed. These are then transformed back to the original polar segment, and the step 5 from the above process is performed.

---

[3]For observations close to zenith the main lobe takes up a large azimuthal range. I identify grating sidelobes by which polar projection sections have the largest number of sources. The large azimuthal range of the main lobe makes this more difficult so it is subtracted first.

[4]This formula determines the great circle distance between two points in a spherical projection.

Grating sidelobe Identification Algorithm

Once the sources in the main lobe have been subsetted from the main catalogue
the probable centre of the grating sidelobes can be identified. The iterative pro-
cess I developed to do this is described below:

1. The polar projected data is broken into 8 segments relative to the origin.
   The angular size of each region is 45 deg. The number of sources for each
   segment is determined.

2. The segment with the most number of sources is selected and the average
   source position is determined. This becomes the preliminary lobe centre.

3. The lobe centre and size sub-routine is applied to this region. Once the
   lobe has been identified the lobe data is subset from the main catalogue.
   The lobe meta data python dictionary is then updated with the same in-
   formation as the main lobe.

4. Steps 2 and 3 are repeated until 95% of the apparent flux density has been
   subset from the original total source catalogue. This threshold value can
   optionally be increased by the user input.

5. Once the threshold is reached the lobe meta data dictionary is written to a
   text file.

An example of the lobe finding can be seen in Figure 6.1. This shows the
observation ObsA of Pic A. The prominent grating sidelobe is circled by the lobe
finding region, and the centre is the red dot. This same process is applied for the
main lobe and the other grating sidelobes. The colour bar scale is the logarithm
of the apparent flux density.

6.2   Model Masking Algorithm

Once the lobes have been identified by the script `lobe-finder.py` the imaged
region of interest can now be masked in the model all-sky image. This is done
by the script `model-subset.py`. This script takes in a few inputs: the lobe that
is to be imaged, the OBSID, the lobe-metafits file output by `lobe-finder.py`,
and the pixel scale for the deep image. The method employed by this script is
described below:

1. Load in the lobe-meta data dictionary. Subset this dictionary for the lobe
   of interest. Load in the lobe size in degrees, and the lobe RA and DEC
   centre in degrees.

2. Determine the max and min RA and DEC is determined for the lobe of
   interest. This is done by subtracting a $\delta\theta$ value of $\theta_{\text{size}}/\sqrt{2}$ from the centre
   RA and DEC, where θ_{size} is the size indexed from the lobe-meta data.

3. Load in the model image. Using the PYTHON package ASTROPY determine
   the world coordinate system (wsc) from the model image file header. This
   converts the image pixel values to RA and DEC values based on the image
   projection.
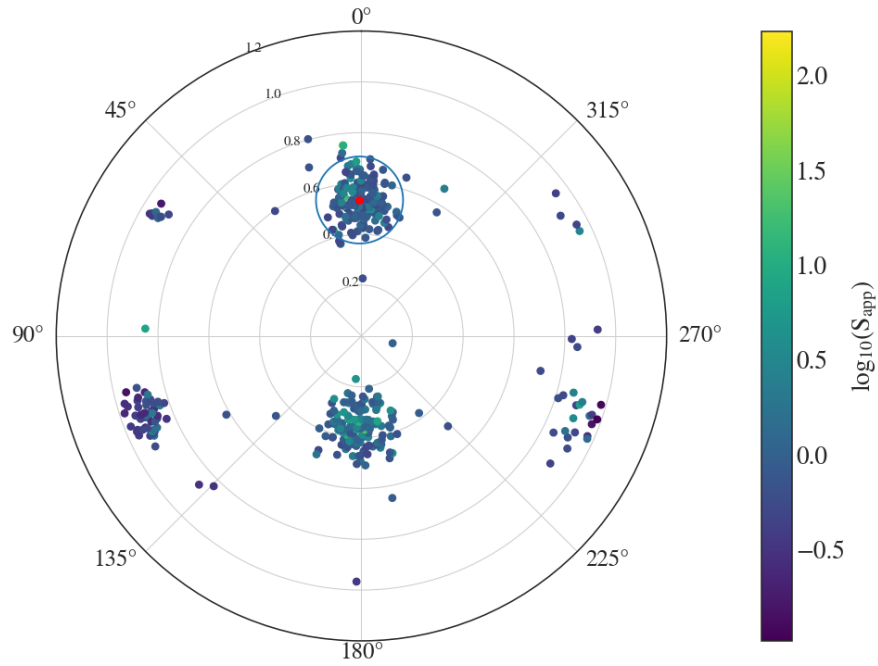
Figure 6.1: Orthographic projection of the sources found in the Pic A observation ObsA all-sky image. The circular region is the grating sidelobe region found by the script `lobe-finder.py`. The red dot denotes the centre of the lobe.

4. Using the wsc the range of pixel values that corresponds to the max RA and max DEC values is determined. Set the pixels in this range to a value of zero. This effectively applies a mask to the lobe region in the model image. Save the updated model image.

5. Using the input scale size, determine the number of pixels required to image the masked lobe. The WSCLEAN imaging parameters are written to a text file. These parameters include the centre of the image in RA and DEC with a hh:mm:ss±dd:mm:ss format. It also includes the image size in pixels, the pixel scale size in arcseconds, and the image resolution. The resolution is determined to be 4.5 times the pixel scale, this is given in arcminutes.

With the successful running of `model-subset.py` the masked model visibilities can now be determined. The WSCLEAN imaging parameters also will allow the creation of the deep lobe image.

6.3 Sky Subtraction

In this Section I outline the sky subtraction process. This process can be iteratively run. I have observed that multiple iterations of sky subtraction appear to be necessary in order to eliminate as much of the sky contribution from the visibilities as possible. The list below details the applied process:

1. Run `model-subset.py` to develop a subsetted model image. Once the new masked model image is created call WSCLEAN with the PREDICT function. This determines the visibilities of the masked model image. It then writes these visibilities to the model column of the observation measurement set.

2. Subtract the model visibilities from the corrected data visibilities. This is done using the CASACORE function TAQL. This function allows for accessing and manipulating measurement set data tables.

3. Run `flag-routine.sh` on the corrected data after model subtraction.

4. If multiple iterations of sky subtraction are required, perform all-sky imaging again using the same parameters as those supplied in `selfcal.sh`. This will produce a new model image.

5. Repeat steps 1-4 for the number of sky subtraction iterations. The default number of iterations is two. Each additional iteration requires imaging the whole sky, this process takes approximately an hour.

This process is encapsulated in the bash script `deep-image.sh`. The number of sky subtraction iterations is given as user input. Once I have separated the non-masked regions contributions to the visibilities the deep imaging can be performed.

6.4   Deep Imaging

Once the sky subtraction is complete the visibilities should be primarily dominated by the masked region. After subtraction I shift the phase centre to the masked region using CHGCENTRE. I then call WSCLEAN using the parameters output from `model-subset.py`. For the deep imaging I use a multi-scale CLEAN with a total number of $500,000$ iterations and a Briggs weighting of 0 (Briggs, 1995). I additionally apply the `-local-rms` option with an `-auto-threshold` of 1.0 sigma and an `-auto-mask` of 3.0 sigma. For each major CLEAN iteration I used an `-mgain` of 0.5. After some experimentation I found these imaging parameters to be a good trade-off in resolution for increase in sensitivity. The result of the process applied in `deep-image.sh` to the two example observations can be seen in Figure 6.2 and 6.3.

Figure 6.2 shows the main lobe of the observation ObsA. This image has been corrected for the primary beam effects. Pic A can be seen in the centre of the image as the bright partially resolved source. There are some sidelobe artefacts still present in the image. Close inspection of the image reveals that there is still some RFI present but it is not to the same magnitude as seen in the all-sky images. The rms close to the centre of this image is $56\,\mathrm{mJy/beam}$ which is an improvement of $\sim 34\%$ over the all-sky imaging rms of $86\,\mathrm{mJy/beam}$. This is likely due to the Briggs weighting, as well as the deeper cleaned Pic A. The deeper cleaning removes the sidelobe confusion from the PSF. Additionally the removal of the grating sidelobes and RFI would have also contributed to a reduction in the rms. Further iterations of sky-subtraction will further reduce the PSF sidelobe confusion but at a large computational cost. Additionally more data is flagged
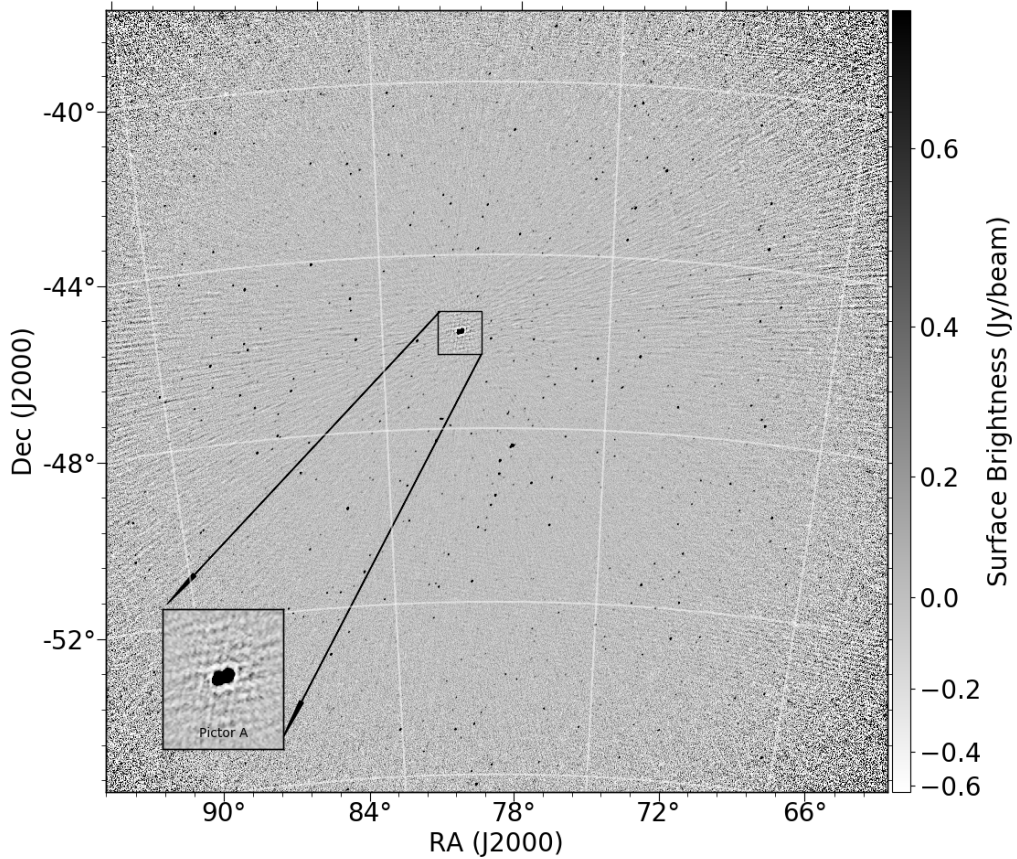
Figure 6.2: Primary beam corrected main lobe image of the observation ObsA. Pic A can be found near the centre of the image, inside the small rectangle. An enlarged version of the rectangle can be found in the overlaid Subfigure in the bottom left corner. This shows and enlarged image of Pic A. It is clearly partially resolved. Sidelobe artefacts from Pic A can be seen across the image. The rms of this image is 56 mJy. The pixel scale of the image is 18 arcseonds.

with each iteration as a result of `flag-routine.sh`, so the optimal sensitivity also decreases. This is why a default of two iterations is used.

Figure 6.3 shows the primary beam corrected main lobe image of observation ObsB. This observation is not dominated by a bright source such as Pic A, so the rms close to the centre of the image is approximately 31 mJy/beam compared to 48 mJy/beam for the all-sky image. This is an improvement of $\sim 35\%$ similar to ObsA. As a result of the lower rms more sources are present. Close inspection of this image shows artefacts originating from the leftmost side of the image. These are from Pic A which has been cropped out. Pic A in this observation is close to the minima between the main lobe and the neighbouring grating sidelobe. There is also RFI in this image in the same locations as Figure 6.2.

6.5   Summary

The imaging strategy and sky subtraction method I described in this Chapter has produced relatively deep images with low rms. With the culmination of this
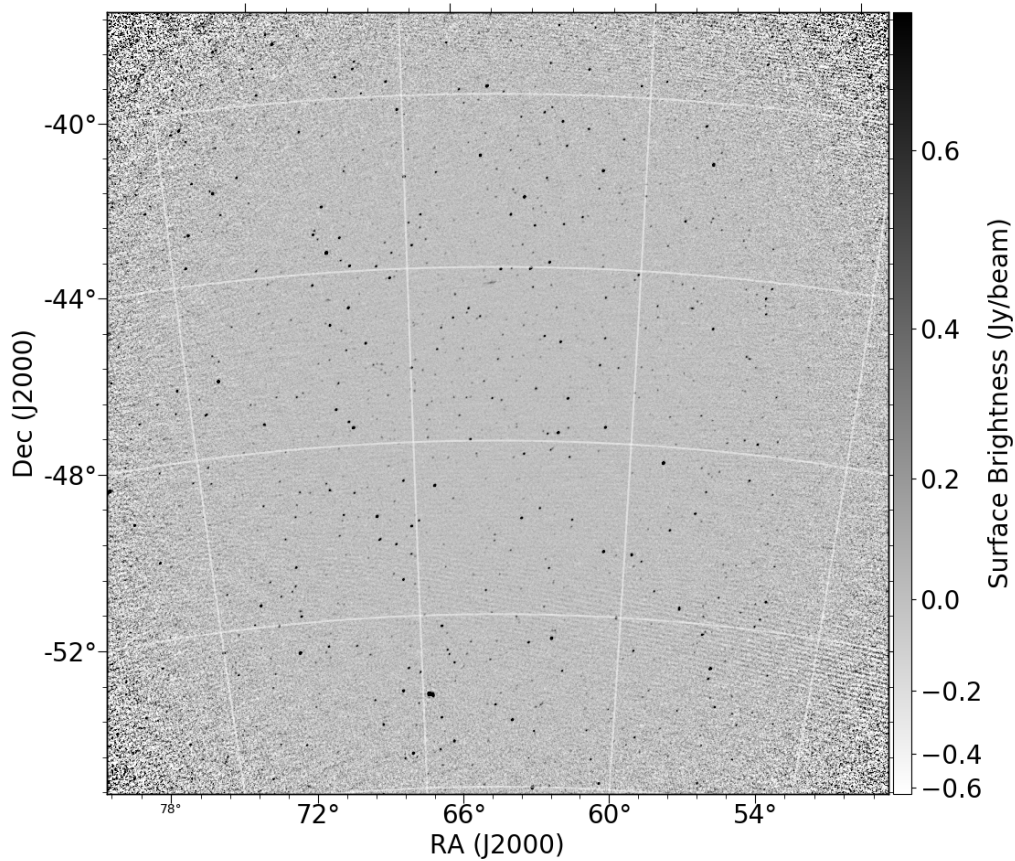
Figure 6.3: Primary beam corrected main lobe image of the observation ObsB. The rms of this image is 31 mJy which is much lower than the Pic A image. The higher rms in the other image may be due to the sidelobes of Pic A. As a result of the lower rms many more sources are visible. The pixel scale of the image is 18 arcseonds.

imaging strategy the full method for processing and imaging MWA observations at 300 MHz is now complete. This method is now ready to be applied to further MWA 300 MHz snapshot observations.

Chapter 7

Results & Discussion

In this Chapter I will focus on the results and analysis of the image products from the two example observations, and an additional set of three observations that I processed with the 300 MHz pipeline. In Section 7.3 I compute the astrometry and flux scales of the five observations as compared to the Total300 sky-model. Section 7.4 will detail the discussion and the proposed future work. Section 7.5 will conclude the findings of this project, and thus the thesis.

7.1 300 MHz Processing Pipeline

The various bash and PYTHON scripts which perform the myriad of processing tasks described in the previous Chapters, were consolidated in the MWA 300 MHz processing pipeline (S300-PIPELINE). This pipeline is available at the github repository S300-PIPELINE[1]. The work flow of the pipeline is shown in Figure 7.1, describing the processing of an observation from the downloading of the raw data to the final image product.

   I split each phase into one or several bash scripts. Each script manages the flow of processed data through input arguments. In the list below I detail the scripts for each phase, and the subsidiary PYTHON scripts that were written for each main script:

1. `obs-download.sh`

    (a) `flag-routine.sh`

2. `S300-processing-pipeline.sh`

    (a) `build-appsky.sh`

        i. `Model_format.py`
        ii. `vo2newmodel.py`

    (b) `cal.sh`

        i. `flag-routine.sh`

    (c) `selfcal.sh`

---

[1]https://github.com/JaidenCook/300-MHz-Pipeline-Scripts
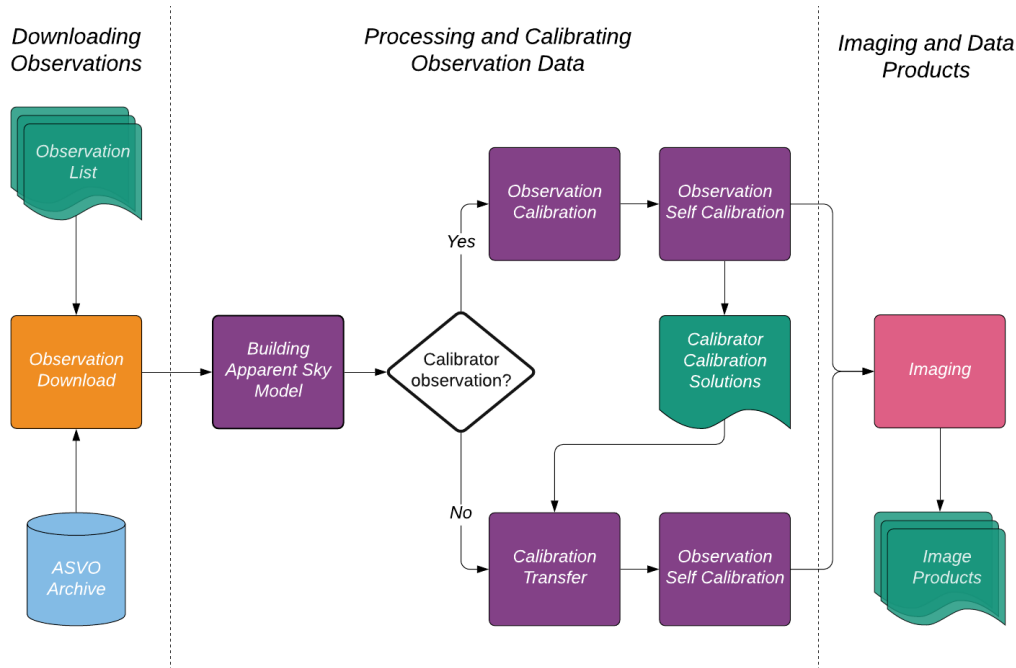
Figure 7.1: The data processing and imaging pipeline developed for MWA observations at 300 MHz. This flow chart is split into three main sections, the first Section details the flow for downloading observations. The second Section details the processing of the data, this is the calibration and self calibration. The third Section details the imaging.

      i. `flag-routine.sh`

   (d) `cal-transfer.sh`

      i. `flag-routine.sh`

3. `deep-image.sh`

   (a) `flag-routine.sh`

   (b) `lobe-finder.py`

   (c) `model-subset.py`

Phase 1 (Downloading Observations):   This phase is the initial downloading of the raw observation data, which are then flagged and consolidated into a measurement set. Further flagging is then applied to remove as much RFI as possible.

Phase 2 (Processing and Calibrating Observation Data):   This phase is split into 4 main parts; the parts applied to an observation depend on whether that observation is a calibrator observation or a non-calibrator observation. This is determined by input into the pipeline. In part (a) the input observation regardless of whether it is a calibrator observation or a non-calibrator observation has an apparent sky-model constructed for it. In this phase an apparent sky-model is build for every observation (part (a)). The second part (b) is the sky-model calibration Section. This is only applied to the calibrator observations. Part (c) is the self calibration step; this is where the all-sky image is created. Non-calibrator

observations are processed in part (d) where the calibrator solutions are transferred to these observations. For the non-calibrator observations part (c) can be called with optional self-calibration. The important product here is the all-sky image which is needed for the deep imaging.

Phase 3 (Imaging and Data Products):   This is the final data product and imaging phase. This process is the deep imaging and the resulting sky subtraction algorithm applied in Chapter 6. The final result is a relatively deep image of the lobe of choice.

Examples of the data structure of the pipeline and how to run the pipeline and the individual scripts can be found in the github repository S300-PIPELINE[2].

7.2   Processed Observations

Using the S300-PIPELINE a total of five deep primary beam corrected main lobe images were made. The first two images from the example observations are given in Chapter 6 Figures 6.2 and 6.3. The three additional observations are (1) ObsG23, which is of the GAMA23 field first mentioned in Chapter 5; (2) observation 1126709848 of the bright radio galaxy 3C444 (3C444); and (3) the observation 1139931552 of the bright partially resolved extended radio galaxy Hydra A (HydA). All of these are calibrator observations except for GAMA23. This observation is not dominated by a bright calibrator source, but was successfully processed without calibration solution transfer. There are also an additional 12 observations that have calibrated visibilities and apparent all-sky images. These 12 observations will be processed in future work. The deep main lobe images of the additional three observations are presented in Figure **??**.

Figure 7.2 is the main lobe image of the GAMA 23 field; this observation has an rms of 32 mJy/beam near the centre of the image. The resolution for this image is approximately $\theta_a = 2.56$ arcmin and $\theta_b = 2.07$ arcmin. Figure 7.3 shows the primary beam corrected main lobe image of the 3C444 observation, this has an rms of 54 mJy/beam near the centre of the image. 3C444 is a bright point source which at uniform weighting should be a partially resolved source. The total flux density of 3C444 is approximately 30 Jy. The sidelobe confusion from 3C444 could explain the higher rms.

The image of the HydA main lobe is shown in Figure 7.4. This image has an rms of 15 mJy/beam near the centre of the image. HydA sidelobe artefacts are clearly emanating outwards from the source, so the rms is likely sidelobe confusion dominated. The rms is much lower than expected, especially for an observation that should be sidelobe confusion limited. I estimate the thermal noise for a snapshot MWA 300 MHz observation to be 12.7 mJy/beam[3]. This estimate considers a zenith pointing with no flagging and natural weighting. The more likely explanation is that there was a calibration error for this observation, which will be discussed in further detail in the next Section.

---

[2]https://github.com/JaidenCook/300-MHz-Pipeline-Scripts
[3]The calculation for this is determined in the Appendix Section B.2

Figure 7.2: Contains the 18×18 deg primary beam corrected main lobe image for the observations of the GAMA 23 field. This image was produced after subtracting a model of the rest of the sky as described in Chapter 6.

7.3   Astrometry & Flux Scale

With the five processed observations, it is now possible to perform a preliminary analysis of the flux scale and astrometry of MWA observations at 300 MHz. Source finding was performed with AEGEAN, the same process as applied in Chapter 6. This was applied to each of the observations. These catalogues were then concatenated into a total source catalogue, where each source was given a flag ID that matched its OBSID. This makes it possible to subset out the particular sources for each observations. The total number of sources in this composite catalogue was $2,684$. This was then cross-matched to the Total300 model with a separation of 2 arcminutes. The total number of cross-matches found was $2,508$, constituting 93% of the total source catalogue. The 176 sources without a match will be discussed in the following Subsection 7.3.1.

After I cross-matched the Total300 catalogue with the source catalogue, I determined the error in the RA $\delta\theta_{\mathrm{RA}}$ and the error in the DEC $\delta\theta_{\mathrm{DEC}}$ for each source. I also calculated the flux density ratio of the measured integrated flux to the predicted Total300 model integrated flux. The median, and standard deviation for these three quantities is shown for each of the five observations in Table 7.1.

Figure 7.3: Contains the $18 \times 18 \, \mathrm{deg}$ primary beam corrected main lobe image for the observations of 3C444. This image was produced after subtracting a model of the rest of the sky as described in Chapter 6.

7.3.1   Flux Scale

The median flux density ratio for all observations with the exception of HydA is $\langle S_{\mathrm{ratio}} \rangle \geq 1$. The median value may be greater than one because the self-calibration process may be overestimating the flux density. The HydA observation has a median flux ratio of 0.37. This is far below the predicted values. As previously mentioned this result is potentially due to amplitude calibration errors for this observation. Hydra A is a partially resolved radio galaxy with an extended profile. As such the model selected from GLEAM_Sup was a multi-component Gaussian model. Due to the extended nature of the source the total flux may not be properly determined by the model. This may have led to some constant factor decrease in the amplitude across the entire observation bandwidth. In theory it should be easy to correct for this, but the flux scale at this frequency needs to first be determined before the correct scaling factor can be applied. A histogram of the flux scale without the sources from the HydA observation can be seen in Figure 7.5.

The median flux density ratio for the total source catalogue minus the HydA sources is $\langle S_\nu \rangle = 1.36 \pm 0.3$. This median represents a significant deviation from a ratio of one. The total deviation may not be indicative of the cause for the
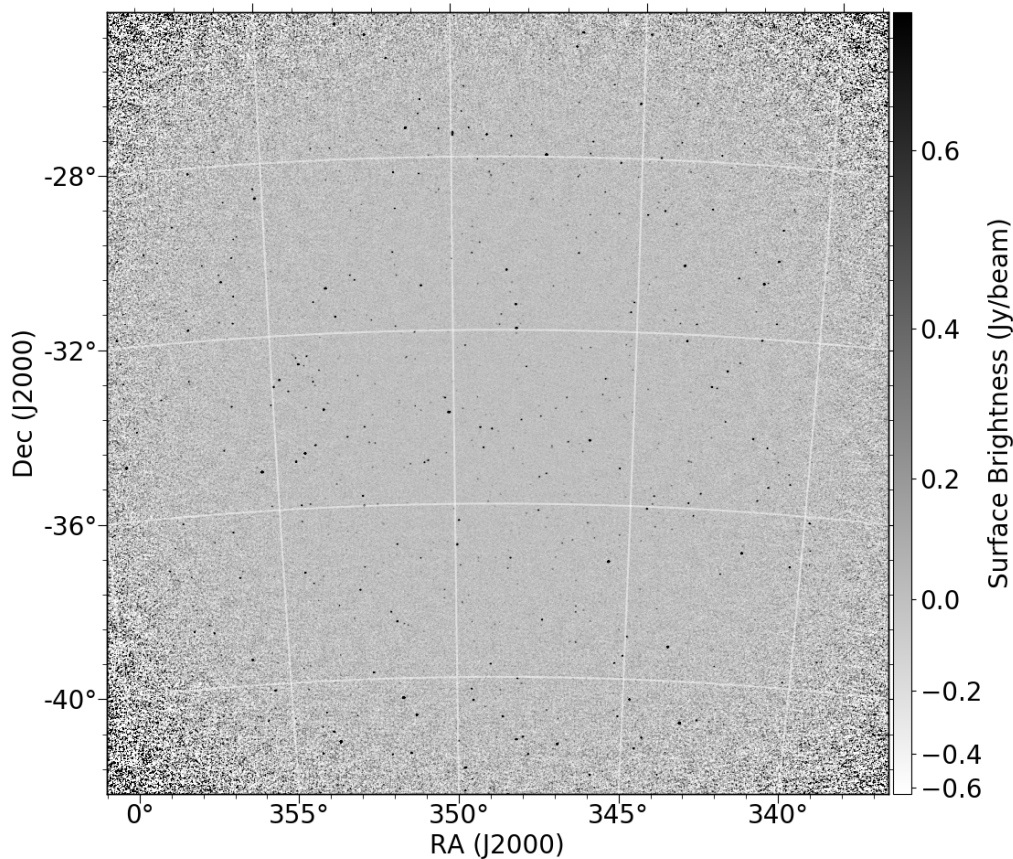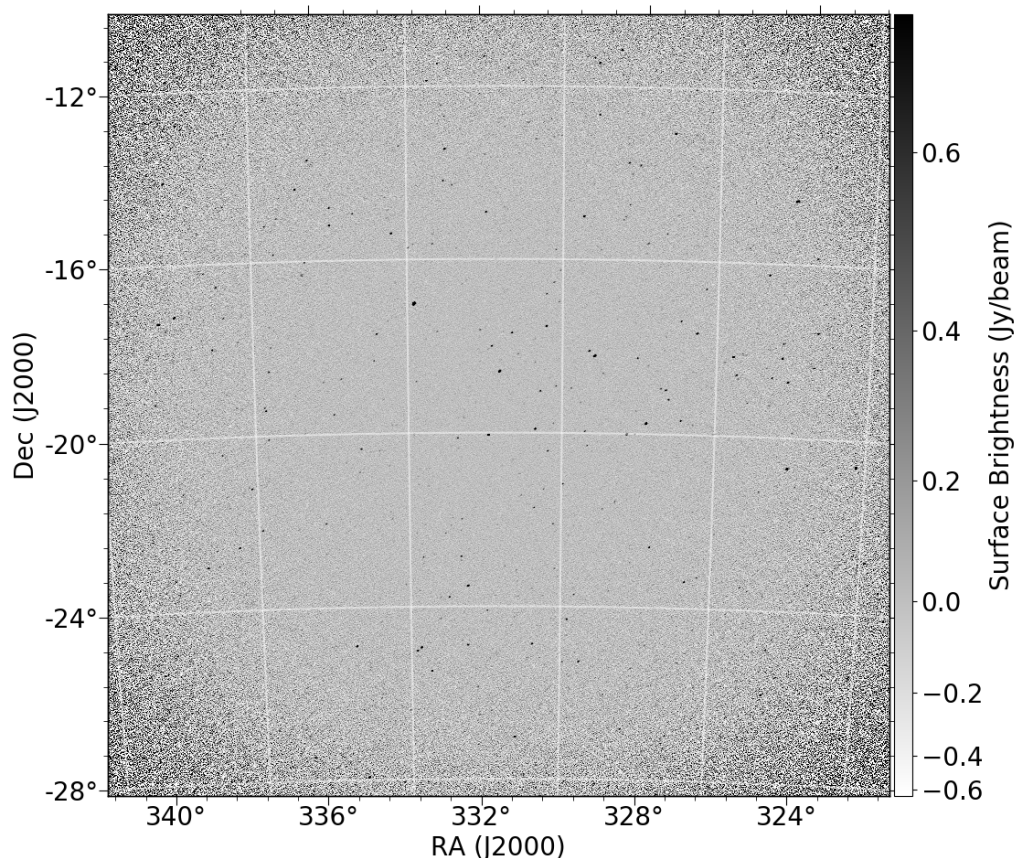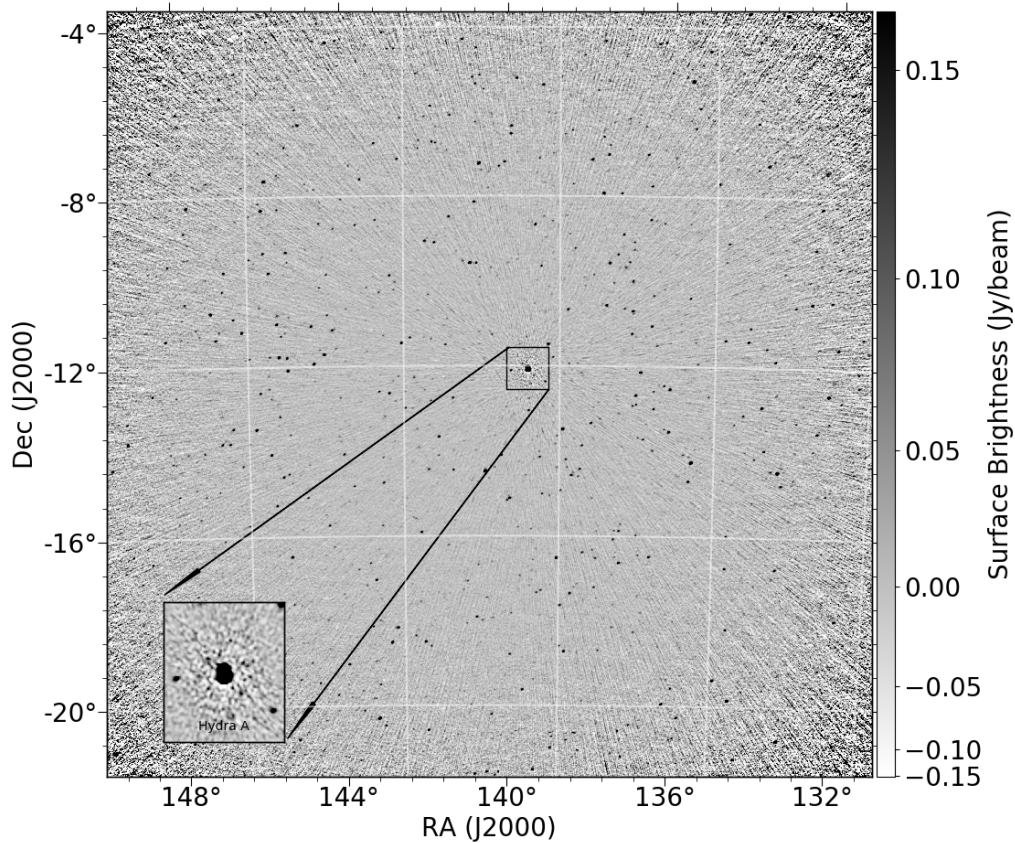
Figure 7.4: Contains the 18×18 deg primary beam corrected main lobe image for the observations of Hydra A. This image was produced after subtracting a model of the rest of the sky as described in Chapter 6. Hydra A can be seen near the centre of the image, where it is surrounded by a black box. The overlaid Subfigure in the bottom left corner is the enlarged 1×1 degree box around Hydra A.

deviation. If we look at the median deviations from Table 7.1 for ObsA and ObsB these match the median deviation of the GAMA23 observations. The GAMA23 observation was not calibrated on the bright source Pic A unlike the other two observations. Therefore these deviations may not be due to amplitude calibration errors in Pic A. The source of the errors is likely due to inaccuracies in the sky model and the MWA tile beam model. More observations need to be processed with different calibrators to determine the root cause of the deviation.

In another consideration of the potential source of this deviation, in Section 4.5 of Chapter 4 I compare the median flux densities for the three main model components of the Total300 sky model. Here I found that the GLEAM_Sup and PUMA300 components deviated from one another. The deviation in their median flux density values was approximately a factor of 1.4, with the GLEAM_Sup model having a higher median flux density. I suggested the deviation was caused by the over estimate of the 300 MHz flux density by extrapolation from the GLEAM sky-model. I also suggested the variation in the two flux scales was caused by the inclusion of higher frequency data from NVSS in the PUMA300 model. It is important to note that all the sources from the five observations cross-matched

OBSID	Observation	N	$\langle S_\nu/S_\mathrm{mod}\rangle \pm \sigma_S$	$\langle \delta\theta_\mathrm{RA}\rangle \pm \sigma_\mathrm{RA}$ arcminutes	$\langle \delta\theta_\mathrm{DEC}\rangle \pm \sigma_\mathrm{DEC}$ arcminutes
1131042024	ObsA	457	1.48 ± 0.26	-0.14 ± 0.13	0.21 ± 0.09
1131038424	ObsB	656	1.33 ± 0.25	-0.09 ± 0.17	0.22 ± 0.12
1121285808	ObsG23	624	1.40 ± 0.27	0.09 ± 0.15	0.03 ± 0.12
1126709848	3C444	193	1.00 ± 0.16	-0.20 ± 0.09	0.17 ± 0.09
1139931552	HydA	578	0.37 ± 0.07	0.015 ± 0.24	-0.01 ± 0.21

Table 7.1: Breakdown of the statistics for the five presented deep primary beam corrected main lobe images. This table presents the median flux density ratio between the observations measured flux density and the Total300 model flux density. It also presents the median 1σ error in the RA and DEC.

with the Total300 sky-model are from PUMA300, not GLEAM_Sup. As with the previous hypothesis more investigation is required to determine the cause. This will be discussed further in Section 7.4.

7.3.2 Astrometry

Figure 7.6 shows the distribution of error in the RA ($\delta\theta_\mathrm{RA}$) and the error in the DEC ($\delta\theta_\mathrm{DEC}$) for each of the five observations. The median and IQR derived standard deviations values for each observation are presented in Table 7.1.

The error in the RA and the error in the DEC appears to have some systematic offset for all observations in Figure 7.6, with the exception of the HydA observation. The median offsets as seen in Table 7.1 appear to be on the order of $\delta\theta \sim 0.2$ arcmin. This corresponds to an offset of $\delta\theta \sim 12$ arcsec; this is less than the pixel scale which on average is approximately 18 arcsec[4]. This offset is still large enough that it can be used to correct the Total300 sky model. The standard deviation in the RA and DEC error is on a similar magnitude as the offset. The offset seen at lower frequency MWA observations has a larger magnitude than those seen in 300 MHz observations. This is what I expected since observations at 300 MHz should be less affected by ionospheric effects than other lower frequency MWA observations. This is due to the λ^2 dependence on ionospheric effects. This offset could additionally be the result of systematic errors introduced by the self-calibration process.

The HydA observation shows some correlation in the RA and DEC errors. I determined the Pearson's correlation coefficient for these values to be $\rho = -0.56$. This covariance could be related to errors in the model position. Incorrect position could cause phase offsets. The errors in the RA, the DEC and the flux calibration for Hydra A have been observed with MWA data at lower frequencies by other collaborators.

7.3.3 Sources Without Matches

As in Section 7.3 I cross-matched the sources in the five observations with the Total300 sky-model catalogue and found 174 sources without matches. The ob-

---

[4]The PSF is approximately 4.5 times the pixel scale as mentioned in Section 6.2
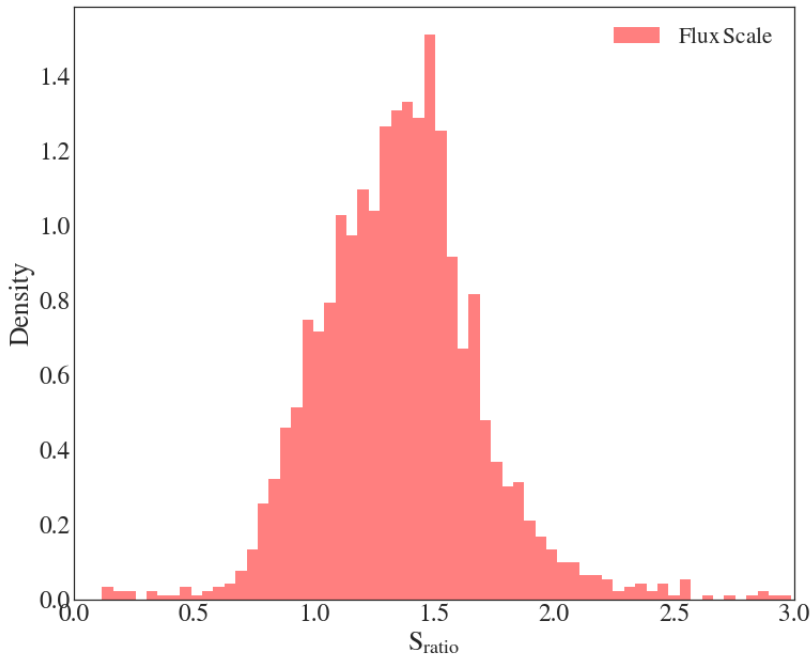
Figure 7.5: This histogram shows the ratio of the integrated flux density to the model flux density for four of the five presented observations. The missing observation HydA is not included because the flux scale here is not consistent with the other observations. This is likely due to an amplitude calibration error.

servations ObsA and ObsB have considerable overlap in the regions of the sky they observed. These two observations were taken during the same observing night with the same beam projection. This means the joint five observation catalogue I used to cross-match with the Total300 sky-model had double detections in these overlapping regions. Therefore when I cross-matched the two catalogues, the matches with the closest separation to the Total300 were recorded. Those double detection sources with worse separations constitute the vast majority of the 174 sources without matches. Eliminating sources in the overlapping regions leaves 19 sources without detections. The remaining 19 detections require further follow up. In future work I plan to cross-match these sources with a higher frequency catalogue such as NVSS. Sources without cross-matches could be artefacts or transient objects such as satellites. I have observed satellites in several observations at 300 MHz throughout this project, even after RFI flagging.[5] Potentially these could be sources with positive spectral indices, which would explain why they may not be detected at the lower frequency ranges of the MWA.

---

[5]It can be hard to determine what channels are affected by RFI from satellites. Some satellites can be identified which can be useful in excising the resulting RFI. This is an ongoing area of study by members of the MWA community. Unidentifiable satellites can be flagged with the flagging strategy but this might not eliminate all the RFI. Alternately images of coarse channels can be made to narrow down the frequency range in which unidentifiable satellites reflect or emit RFI. This is a time consuming process and was not considered during this project.

(a) ObsA Observation

(b) ObsB Observation

(c) Hydra A Observation

(d) GAMA23 Observation

(e) 3C444 Observation

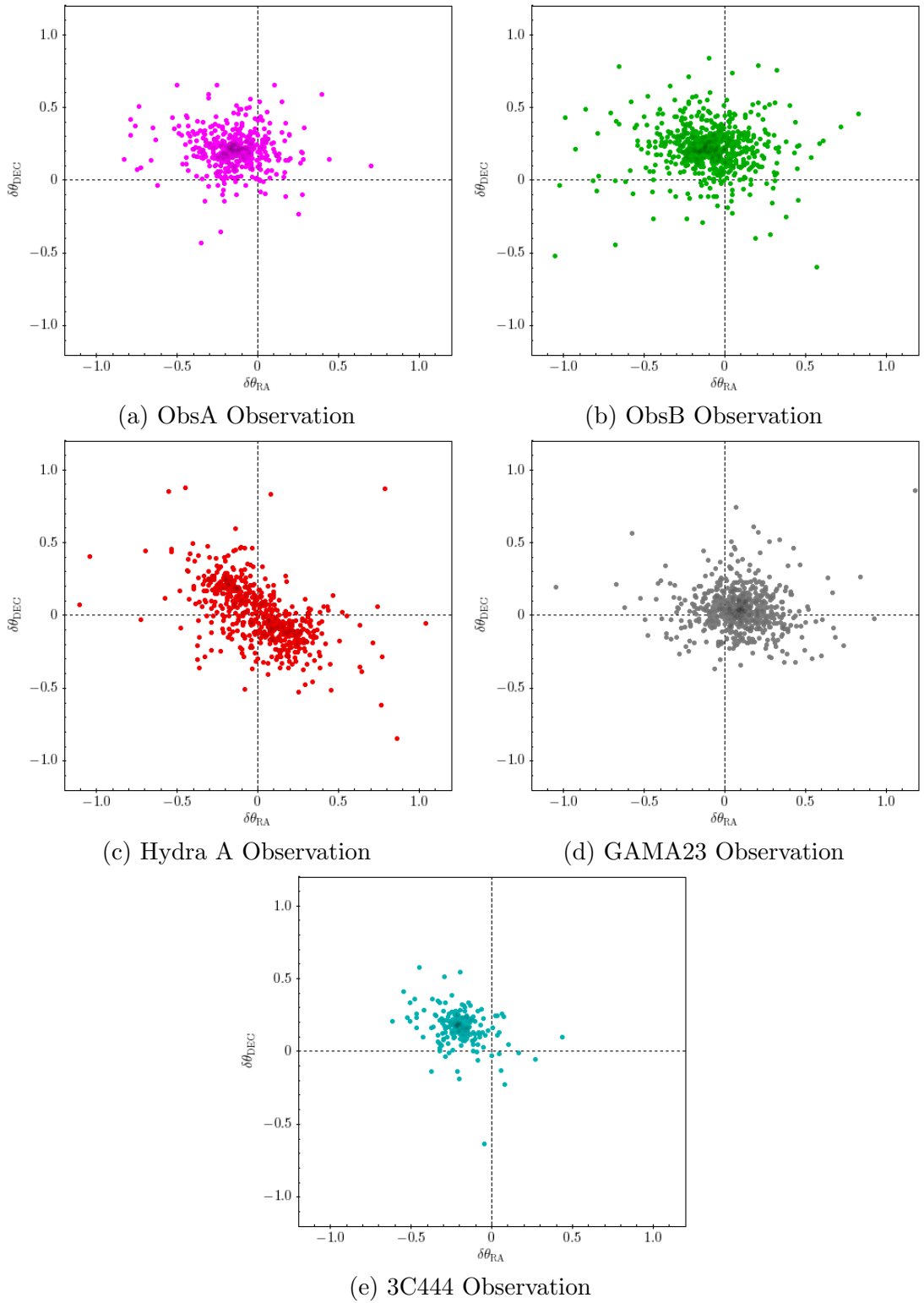Figure 7.6: Difference in the RA and DEC between the model and the measured sources for the five presented observations. Most of deviations are offset in RA and DEC. The Hydra A observation displays a level of correlation between the error in the RA and DEC. The scale for the axes is in arcminutes. Theoretically I can determine what $\Delta\theta$ should be using the Cramer Rao-Bound, and this will be considered in future work.

7.4   Discussion

The aim of my project was to create a model at 300 MHz which could be used in conjunction with the 2016 MWA beam model to calibrate and image MWA observations at 300 MHz. The model in conjunction with the proposed calibration and imaging strategy have been successfully demonstrated to image observations at 300 MHz. The images of the five observations presented in this thesis are the best images made to date at 300 MHz with the MWA. Some of these observations display deviations in their flux scales away from the predicted model 300 MHz flux densities. The root cause of these deviations is yet unknown. It should be noted that the issue of the correct flux scale in the low frequency regime is one that is still debated (Hurley-Walker, 2017). The astrometric errors with exception of the HydA observation presented in this thesis are within the range of the image pixel scale. These offsets therefore are straight forward to fix in post processing of the data. The results of this work are planned to be published in future work. The following Subsection will investigate some of the future work that will be undertaken in the planned publication as well as longer term future work proposals.

7.4.1   Future Work

Determining the flux scale for the observations is the biggest issue presented with the final data products. The flux scale is important because it determines the flux density of the radio sources measured in the observation. It is with the flux density measurements that science is primarily conducted in radio astronomy. Therefore it is critical that the scale is properly calibrated. In Section 7.3 two hypotheses were proposed to explain the deviation away from the predicted model flux densities. Here I present a method for further investigating the preliminary results in this project.

Flux Scale

More data are needed to determine whether the deviations are related to the calibration solutions or if there is a mean systematic offset between the model and observations. Observations of other calibrators that are preferably not extended like HydA should be carried out. A list of calibrator sources used for the GLEAM observations is given in Wayth et al. (2015). Since the whole sky was observed at 300 MHz with the Phase I MWA configuration there exists a large cache of observations at 300 MHz. These observations will include various calibrator sources. This will also have the added benefit of developing a reliable list of calibrator sources. Additionally more general non-calibrator dominated observations should be processed like the GAMA23 observation. By processing these two types of observations it should become more clear if there is an independent effect that affects both types of observations, or if the observed offset is due just to calibration error.

   Systematic errors may also exist in the primary beam model. Imaging the grating sidelobes and comparing their flux scale to the main lobe is important in determining if the primary beam is correct in these regions. Systematic errors in

the primary beam model may manifest themselves as a function of distance from the pointing centre. Additionally further investigation can be done by processing subsequent snapshot observations at the same pointing. These can be used to determine whether the flux density of sources changes as they move through different parts of the primary beam. These systematic effects are important to understand because they will affect the flux scale.

In Hurley-Walker et al. (2017) it is mentioned that there is covariance in the flux density for the subbands for the GLEAM observations. When fitting the SED's for sources in this project it was assumed there was no covariance. In Hurley-Walker et al. (2017) they use a Matern covariance function to characterise the covariance in the subbands when fitting the SED's. The Matern covariance function models the covariance as a function of distance. In this instance distance is characterised by frequency. This should be applied to the PUMA300 source, and the fit performed again. This will provide more accurate fits at the lower frequency end of the spectrum.

A final important consideration on the flux scale is required. The flux densities for the bright calibrator sources in the Total300 model were determined from Perley & Butler (2017). The flux scale presented in this paper were purported to be reliable down to $\sim 250\,\mathrm{MHz}$. The measured total integrated flux densities for these sources should then be in agreement with the flux scale in Perley & Butler (2017). If they are not in agreement this could indicate a systematic offset in the MWA flux scale at $300\,\mathrm{MHz}$. Alternatively this difference could be due to instrumental systematics with the Perley & Butler (2017) flux scale, since this was obtained with the VLA.

Long Term Goals

There are two important long term goals to achieve with observations at $300\,\mathrm{MHz}$. The first goal is to extend the method to MWA phase II data. Since there is a large volume of data with the Phase II observations, this will require adjusting some of the parameters of the method. Additionally the model is built on a lower resolution MWA catalogue, so it will be necessary to calibrate the data with a restricted set of visibilities. Observations of the GAMA 23 field and of 3C444 have already been procured as a stretch goal for this project. These will provide the highest resolution images possible with the MWA. With uniform weighted images the long baseline MWA Phase II configuration can achieve resolutions similar to the NVSS survey.

Another proof of concept will be creating images of the grating sidelobes. For this project I focused on making images of the main lobe, since this determines the field of view of radio interferometer observations. At $300\,\mathrm{MHz}$ due to the high frequency regime the main lobe reflections in the primary beam pattern basically act as multiple fields of view. It should be possible to image the grating sidelobes since the sensitivity in these regions is on the order of the main lobe. What was thought to be the greatest weakness at $300\,\mathrm{MHz}$ could become its greatest strength. It may then be possible to utilise this feature when observing. A good example of this is the case of ObsA. The primary beam pattern of this observation has the main lobe and a prominent grating sidelobe, both almost

equidistant from zenith. The other grating sidelobes are far less sensitive than these two regions. The main lobe in this case is actually further from zenith than the prominent grating sidelobe. It should then be possible to image the prominent grating sidelobe. The method outlined in Chapter 6 is sufficiently general to allow this to be easily tested.

7.5   Conclusion

The aim of this project was to develop a method for processing and imaging MWA observations at 300 MHz. I have created a working pipeline for calibrating and imaging MWA 300 MHz observations. This pipeline is available to the community through the github repository S300-PIPELINE[6]. Prior to this work observations were not processed due to the highly sensitive grating sidelobes present at 300 MHz. These grating sidelobes have sensitivities on the order of the main lobe. This posed a challenge for calibration and thus data processing. This work combined the efforts of several MWA science and technical achievements. In doing so I created a working method for processing and imaging MWA observations in the 300 MHz high frequency regime. The aforementioned achievements in particular include the all sky survey GLEAM, and the 2016 beam model, without either of which this project would not have been feasible. Combining that work together with my own work I have managed to accomplish the main goal of the project. With further work the method can be refined and the systematics better understood. With these future goals accomplished, this method should make a useful contribution to the science conducted by the MWA.

7.6   Acknowledgements

---

[6]https://github.com/JaidenCook/300-MHz-Pipeline-Scripts

Appendix A

Polylogarithmic Coefficient Transformation Function

A.1 Formalising the Polylogarithmic Transformation:

Consider the problem where you have two polylogarithmic functions of arbitrary order p:

$$f(\nu) = \sum_{i=0}^{p} a_i \left(\log\left(\frac{\nu}{\nu_a} \right) \right)^i \tag{A.1}$$

$$g(\nu) = \sum_{i=0}^{p} b_i \left(\log\left(\frac{\nu}{\nu_b} \right) \right)^i \tag{A.2}$$

In the above equations ν_a and ν_b are the normalisation constants for their respective polylogarithmic functions. Now consider the scenario where $f(\nu) = g(\nu) \; \forall \; \nu \in \mathbf{R}$, but $\nu_a \neq \nu_b$ and $a_i \neq b_i \; \forall \; i$.

Proposition: There should exist a transform of the vector of polylogarithmic coefficients denoted by $\mathbf{a}$ from the space ν/ν_a to the space ν/ν_b, where the transformation vector is given by $\mathbf{b}$. Each coefficient element $b_l \in \mathbf{b}$, is expressible as the linear combination of the product of coefficients $a_i \in \mathbf{a}$, $\log(\nu_b/\nu_a)$, and the binomial coefficients:

$$b_l = \sum_{i=l}^{p} a_i \binom{i}{i-l} \left(\log\left(\frac{\nu_b}{\nu_a} \right) \right)^{i-l} \tag{A.3}$$

Proof: Here we will show through induction how to express Equation A.1 as a linear combination of the terms $\log(\nu/\nu_b)$ and hence derive an expression for each of the coefficients b_i. First we let $\log(\nu/\nu_a) = \log(\nu/\nu_b) + \log(\nu_b/\nu_a) = x + y$, we can then rewrite Equation A.1:

$$f(x(\nu)) = \sum_{i=0}^{p} a_i \left(x + y\right)^i = a_0 + a_1 \left(x + y\right) + \cdots + a_{p-1} \left(x + y\right)^{p-1} + a_p \left(x + y\right)^p$$

(A.4)

We can expand each term in the sum $(x + y)^i$ through a binomial expansion, and hence rewrite each $(x + y)^i$ term as a sum:

$$f(x(\nu)) = \sum_{i=0}^{p} a_i \left[\binom{i}{0} x^i + \binom{i}{1} x^{i-1} y + \cdots + \binom{i}{i-1} x y^{i-1} + \binom{i}{i} y^i \right] \quad \text{(A.5)}$$

$$= \sum_{i=0}^{p} a_i \sum_{j=0}^{i} \binom{i}{j} x^{i-j} y^j \quad \text{(A.6)}$$

By factoring out the zeroth x terms we can rewrite the expression in Equation A.5:

$$f(x(\nu)) = \sum_{i=0}^{p} a_i \left[\sum_{j=0}^{i-1} \binom{i}{j} x^{i-j} y^j + \binom{i}{i} y^i \right] \quad \text{(A.7)}$$

$$= \sum_{i=0}^{p} a_i \binom{i}{i} y^i + \sum_{i=1}^{p} a_i \sum_{j=0}^{i-1} \binom{i}{j} x^{i-j} y^j \quad \text{(A.8)}$$

Since all the zeroth order x terms have been factored out, the new inner sum reduces by 1, and the outer sum subsequently increments by 1 since the inner sum cannot start at -1. This factorisation process can be extended to each successive lowest order x term, to generally prove this, consider the arbitrary step k which is defined below:

$$\sum_{i=k}^{p} a_i \sum_{j=0}^{i-k} \binom{i}{j} x^{i-j} y^j = \sum_{i=k}^{p} a_i \left[\binom{i}{0} x^i + \binom{i}{1} x^{i-1} y + \cdots + \binom{i}{i-k} x^k y^{i-k} \right].$$

(A.9)

We see in Equation A.9 that similar to the form written in Equation A.5, that if we let $k = 0$ we reduce to the entire sum. Now we factor out the kth order x term from Equation A.9:

$$\sum_{i=k}^{p} a_i \sum_{j=0}^{i-k} \binom{i}{j} x^{i-j} y^j = \sum_{i=k}^{p} a_i \left[\sum_{j=0}^{i-k-1} \binom{i}{j} x^{i-j} y^j + \binom{i}{i-k} x^k y^{i-k} \right] \quad \text{(A.10)}$$

$$= \left(\sum_{i=k}^{p} a_i \binom{i}{i-k} y^{i-k} \right) x^k + \sum_{i=k+1}^{p} a_i \sum_{j=0}^{i-k-1} \binom{i}{j} x^{i-j} y^j$$

(A.11)

Again we see that this factorisation reflects that of the zeroth order term. If we let $p = k + 1$, hence $k = p - 1$, then we retrieve the last two terms of the factorisation, for the highest and second highest orders of x:

$$\sum_{i=k}^{p} a_i \sum_{j=0}^{i-k} \binom{i}{j} x^{i-j} y^j = \left(\sum_{i=p-1}^{p} a_i \binom{i}{i-(p-1)} y^{i-(p-1)} \right) x^{p-1} + a_p \binom{p}{0} x^p \quad \text{(A.12)}$$

We are now in a position to express Equation A.4 as a linear combination of x:

$$f(x(\nu)) = \sum_{i=0}^{p} a_i \binom{i}{i} y^i + \cdots + \left(\sum_{i=l}^{p} a_i \binom{i}{i-l} y^{i-l} \right) x^l + \cdots + a_p \binom{p}{0} x^p \quad \text{(A.13)}$$

$$= b_0 + \cdots + b_l x^l + \cdots + b_p x^p = g(x(\nu)) \quad \text{(A.14)}$$

It is clear to see how the coefficients of $f(x(\nu))$ map to the coefficients of $g(x(\nu))$, specifically the total sum can be expressed as:

$$g(x(\nu)) = \sum_{l=0}^{p} \left(\sum_{i=l}^{n} a_i \binom{i}{i-l} y^{i-l} \right) x^l \quad \text{(A.15)}$$

$$= \sum_{l=0}^{p} \left(\sum_{i=l}^{p} a_i \binom{i}{i-l} \log^{i-l}\left(\frac{\nu_b}{\nu_a}\right) \right) \log^l\left(\frac{\nu}{\nu_b}\right) \quad \text{(A.16)}$$

And hence for an arbitrary coefficient b_l we can express the transformation as:

$$\therefore b_l = \sum_{i=l}^{p} a_i \binom{i}{i-l} \log^{i-l}\left(\frac{\nu_b}{\nu_a}\right) \quad \text{(A.17)}$$

A.2 Matrix Representation of the Polylogarithmic Coefficient Transformation Function

We can see the emergent pattern where the sum of binomial coefficients in Equation A.17 is the linear combination of the right diagonals on Pascal's triangle, where l is the order.

$$
\begin{array}{lccccc}
p = 0 & & & 1 & & \\
p = 1 & & & 1 & 1 & \\
p = 2 & & 1 & 2 & 1 & \\
p = 3 & & 1 & 3 & 3 & 1 \\
p = 4 & 1 & 4 & 6 & 4 & 1 \\
\hline
& 0 & 1 & 2 & 3 & 4
\end{array}
$$

We can use this pattern to define a transformation matrix that will operate on the vector of coefficients:

$$\mathbf{a} = \begin{pmatrix} a_0 & a_1 & \cdots & a_p \end{pmatrix}$$

Thus transforming vector $\mathbf{a}$ into vector $\mathbf{b}$:

$$\mathbf{b} = \begin{pmatrix} b_0 & b_1 & \cdots & b_p. \end{pmatrix}$$

Consider the upper triangular matrix $\mathbf{P}_{n,n}$ where the dimensions of the triangular matrix n are defined as the order $p + 1$, this is equal to the number of coefficients in an arbitrary polynomial:

$$
\mathbf{P}_{n,n} =
\begin{pmatrix}
\binom{0}{0} & \binom{1}{0} & \binom{2}{0} & \cdots & \binom{p}{0} \\
 & \binom{1}{1} & \binom{2}{1} & \cdots & \binom{p}{1} \\
 & & \ddots & \ddots & \vdots \\
 & & & \ddots & \binom{p}{p-1} \\
0 & & & & \binom{p}{p}
\end{pmatrix}
$$

In this matrix rows consist of the diagonal elements of pascals triangle filling in from right to left, with nill entries being represented by zeros. The next important matrix is the polynomial matrix, which is also an upper triangular matrix, this is represented below:

$$
\mathbf{T}_{n,n} =
\begin{pmatrix}
1 & y & y^2 & \cdots & y^p \\
 & 1 & y & \cdots & y^{p-1} \\
 & & \ddots & \ddots & \vdots \\
 & & & \ddots & y \\
0 & & & & 1
\end{pmatrix}
$$

In the matrix $\mathbf{T}_{n,n}$, the variable y takes on the same value as it did in the previous section. The Hadmard product (element by element product) of the matrices $\mathbf{P}$ and $\mathbf{T}$, produces the polylogarithmic coefficient transformation matrix:

$$
\mathbf{A}_{n,n} =
\begin{pmatrix}
\binom{0}{0} & \binom{1}{0}y & \binom{2}{0}y^2 & \cdots & \binom{p}{0}y^p \\
 & \binom{1}{1} & \binom{2}{1}y & \cdots & \binom{p}{1}y^{p-1} \\
 & & \ddots & \ddots & \vdots \\
 & & & \ddots & \binom{p}{p-1}y \\
0 & & & & \binom{p}{p}
\end{pmatrix}
$$

Thus the transformation can be represented by:

$$
(\mathbf{P} \circ \mathbf{T})\,\mathbf{a}^\top = \mathbf{b}^\top \tag{A.18}
$$

$$
\therefore \mathbf{A}\mathbf{a}^\top = \mathbf{b}^\top \tag{A.19}
$$

Example (Second order Polylogarithmic Functions): Consider the pair of second order polylogarithmic functions:

$$
f(\nu) = a_0 + a_1\left(\log\left(\frac{\nu}{\nu_a}\right)\right) + a_2\left(\log\left(\frac{\nu}{\nu_a}\right)\right)^2 \tag{A.20}
$$

$$
g(\nu) = b_0 + b_1\left(\log\left(\frac{\nu}{\nu_b}\right)\right) + b_2\left(\log\left(\frac{\nu}{\nu_b}\right)\right)^2 \tag{A.21}
$$

Therefore the Pascal's upper triangular matrix $\mathbf{P}_{n,n}$ for this transformation is given below:

$$
\mathbf{P}_{n,n} =
\begin{pmatrix}
1 & 1 & 1 \\
0 & 1 & 2 \\
0 & 0 & 1
\end{pmatrix}
$$

We then have the polynomial matrix $\mathbf{T}_{n,n}$:

$$\mathbf{T}_{n,n} = \begin{pmatrix} 1 & \left(\log\left(\frac{\nu}{\nu_a}\right)\right) & \left(\log\left(\frac{\nu}{\nu_a}\right)\right)^2 \\ 0 & 1 & \left(\log\left(\frac{\nu}{\nu_a}\right)\right) \\ 0 & 0 & 1 \end{pmatrix}$$

Thus the polylogarithmic coefficient transformation matrix is $\mathbf{A}_{n,n}$:

$$\mathbf{A}_{n,n} = \begin{pmatrix} 1 & \left(\log\left(\frac{\nu}{\nu_a}\right)\right) & \left(\log\left(\frac{\nu}{\nu_a}\right)\right)^2 \\ 0 & 1 & 2\left(\log\left(\frac{\nu}{\nu_a}\right)\right) \\ 0 & 0 & 1 \end{pmatrix}$$

Substituting in the values:

$$\begin{pmatrix} 1 & \left(\log\left(\frac{\nu}{\nu_a}\right)\right) & \left(\log\left(\frac{\nu}{\nu_a}\right)\right)^2 \\ 0 & 1 & 2\left(\log\left(\frac{\nu}{\nu_a}\right)\right) \\ 0 & 0 & 1 \end{pmatrix} \begin{pmatrix} a_0 \\ a_1 \\ a_2 \end{pmatrix} = \begin{pmatrix} b_0 \\ b_1 \\ b_2 \end{pmatrix}$$

Multiplying the matrices we arrive at the final expression:

$$\begin{pmatrix} a_0 + a_1\left(\log\left(\frac{\nu}{\nu_a}\right)\right) + a_2\left(\log\left(\frac{\nu}{\nu_a}\right)\right)^2 \\ a_0 + 2a_1\left(\log\left(\frac{\nu}{\nu_a}\right)\right) \\ a_2 \end{pmatrix} = \begin{pmatrix} b_0 \\ b_1 \\ b_2 \end{pmatrix}$$

Appendix B

Stokes Parameters & Error Propagation

B.1 Stokes Parameters

The Stokes parameters are a group of four values I, Q, U, and V, that describe the state of polarisation for electromagnetic radiation (McMaster, 1954). As a result they have uses in both optical and radio astronomy. In particular the Stokes parameters form the mathematical foundation for the Measurement Equation described in Chapter 2. This equation is used to describe the detection of incident radiation on a pair of radio antennas. These four values are typically found in the vector form given below:

$$\mathbf{S} = (I, Q, U, V) \tag{B.1}$$

To describe each of the components of the Stokes vector $\mathbf{S}$, first we consider the properties of propagating plane wave electromagnetic radiation. Following the conventions used in Chapter 2, the incident plane wave propagates in the z-direction, and the electric field oscillates in the (x, y) plane in a Cartesian coordinate system. This means that the electric field of the plane wave radiation can be split into the linearly independent components E_x and E_y. Using these two components we can mathematically describe the four Stokes parameters:

$$I = \langle E_x^2 \rangle + \langle E_y^2 \rangle \tag{B.2}$$
$$Q = \langle E_x^2 \rangle - \langle E_y^2 \rangle \tag{B.3}$$
$$U = 2Re(E_x E_y^\dagger) \tag{B.4}$$
$$V = -2Im(E_x E_y^\dagger) \tag{B.5}$$

In the above equations the angular brackets denote the expectation values for the linearly independent components, and the superscript dagger represents the conjugate transpose. The Stokes I component describes the total intensity of the radiation, this is often the quantity of interest in radio astronomy. The Stokes Q and U describe different forms of linear polarisation states. In particular Q describe vertical or horizontal polarisation states when $U = 0$ and U describes the $45\,\mathrm{deg}$ rotated polarisation state when $Q = 0$. V describes the circular polarisation and this can either be clockwise or anti-clockwise. The combination of these parameters describes the state of radiation, and can also be used to describe the effects of instruments on incident radiation, as demonstrated in Chapter 2.

B.2   Theoretical 300 MHz Sensitivity Limit

The radiometer equation can be used to estimate the sensitivity limit for an MWA snapshot observations at 300 MHz:

$$\sigma_{S_{300}} = \frac{2k_b T}{A_{\text{eff}}} \sqrt{\frac{1}{N(N-1)\Delta\nu\tau_0}} \tag{B.6}$$

Where $\tau_0 = 120$ is the snapshot observation time in seconds, $T_{\text{sys}} = T_{\text{sky}} + T_{Rc}$ the sky temperature at 300 MHz summed with the receiver temperature, $A_{\text{eff}} = 4.75\,\text{m}^2$ is the effective tile area (Ung, 2019), $N = 128$ is the number of tiles, k_b is Boltzmann's constant, and $\Delta\nu = 30.72\,\text{MHz}$ is the bandwidth. The sky temperature is given by $T_{\text{sky}} = 60\lambda^{2.25}\,\text{K}$ (Tingay et al., 2013), hence at 300 MHz, $T_{\text{sky}} = 60\,\text{K}$. Finally $T_{Rc} = 180\,\text{K}$, therefore $T_{\text{sys}} = 240\,\text{K}$. Using these values the sensitivity is estimated to be $\sigma_{S_{300}} \approx 19\,\text{mJy}$. This is the best case scenario assuming that no fine channels are flagged.

Equation B.6 is the estimated RMS for a naturally weighted set of visibilities. In reality there are many kinds of weighting schemes that can be applied to the data, these affect the sensitivity. An in depth derivation of interferometric sensitivity and how weighting schemes can affect the RMS can be found in section 6.2.3 of (Thompson, 2017).

$$\sigma_{S_{300}} = \frac{2k_b T}{A_{\text{eff}}} \sqrt{\frac{1}{N(N-1)\Delta\nu\tau_0}} \frac{w_{\text{mean}}}{w_{\text{rms}}} \tag{B.7}$$

Equation B.7 represents the general form which accounts for the weighting of the data. The general from is Equation B.6 scaled by the ratio of the mean weighting to the RMS of the weightings.

B.2.1   Sensitivity of Flagged Data

As data is flagged the sensitivity reduces. This section will show how the reduction in sensitive is proportional to the square root of the remaining fraction of data. First we start by writing an expression for the total number of independent data points n_d for an arbitrary observation:

$$n_d = n_p n_b n_\tau n_\nu. \tag{B.8}$$

In the above expression $n_p = 2$ is the number of polarisations, $n_b = N(N-1)/2$ is the number of baselines, $n_\tau = \tau_0/\tau_\alpha$ is the number of time samples and $n_\nu = \Delta\nu_0/\Delta\nu_\alpha$ is the number of frequency samples. After a flagging strategy has been applied, a certain fraction R_f of the data will be flagged. This means the remaining number of independent data points n_d' is equal to n_d times the remaining fraction $1-R_f$. Generally we can express n_d' as $n_d' = n_p n_b n_\tau n_\nu (1-R_f)$.

Now we consider the full expression for the total number of independent data points:

$$n_d = N(N-1) \frac{\tau_0}{\tau_\alpha} \frac{\Delta\nu_0}{\Delta\nu_\alpha} \tag{B.9}$$

We can rearrange this expression to match the denominator inside the square root of Equation B.6:

$$n_d \tau_\alpha \Delta \nu_\alpha = N(N-1) \Delta \nu \tau_0 \tag{B.10}$$

Therefore we can express Equation B.6 as:

$$\sigma_{S_{300}} = \frac{2k_b T}{A_{\text{eff}}} \sqrt{\frac{1}{n_d \tau_\alpha \Delta \nu_\alpha}}. \tag{B.11}$$

Following a similar argument we can likewise express $\sigma'_{S_{300}}$ as:

$$\sigma'_{S_{300}} = \frac{2k_b T}{A_{\text{eff}}} \sqrt{\frac{1}{n_d (1-R_f) \tau_\alpha \Delta \nu_\alpha}} \tag{B.12}$$

We then have the relationship:

$$\sigma'_{S_{300}} = \sigma_{S_{300}} \frac{1}{\sqrt{1-R_f}} \tag{B.13}$$

Using Equation B.13 if we know the percentage of data flagged we can estimate the expected theoretical sensitivity of the observation. This does not take into consideration the different weighting schemes that are applied to the independent visibility data points.

B.3   Uncertainty Propagation

Using linear error propagation the error in estimated $300\,\text{MHz}$ flux density is given by:

$$\Delta \log_{10}(S_{300}) \approx \frac{\Delta S_{300}}{\ln(10) S_{300}} \tag{B.14}$$

$$\Delta S_{300} \approx \Delta \log_{10}(S_{300}) \ln(10) S_{300} \tag{B.15}$$

This same form is extended to estimating the log-error in the flux density measurements for each source.

B.4   Determining All-Sky Image Sizes

This equation determines the number of pixels required to create an all-sky MWA image with a zenith phase centre:

$$N_{\text{pix}} = \frac{180 \times 3600}{R_p \Delta \theta} = 4.101 \times 10^5 \left(\frac{\Delta \theta}{\text{arcsec}} \right)^{-1} \tag{B.16}$$

$\Delta \theta$ is the pixel scale in arcseconds, and $R_p = 0.633$. This ratio was derived by taking the ratio of the size of the sine projected celestial sphere in degrees to the actual size.

Bibliography

Baars, J. W. M., Genzel, R., Pauliny-Toth, I. I. K., & Witzel, A. (1977). The absolute spectrum of Cas A; an accurate flux density scale and a set of secondary calibrators. *A&A*, *500*, 135–142.

Beardsley, A. P., Johnston-Hollitt, M., Trott, C. M., Pober, J. C., Morgan, J., Oberoi, D., & Kaplan, D. L. (2019). Science with the Murchison Widefield Array: Phase I results and Phase II opportunities. *PASA*, *36*, e050, `https://doi.org/10.1017/pasa.2019.41`.

Blundell, K. M., Rawlings, S., & Willott, C. J. (1999). The Nature and Evolution of Classical Double Radio Sources from Complete Samples. *AJ*, *117*(2), 677–706, `https://doi.org/10.1086/300721`.

Bock, D. C.-J., Large, M. I., & Sadler, E. M. (1999). SUMSS: A Wide-Field Radio Imaging Survey of the Southern Sky. I. Science Goals, Survey Design, and Instrumentation. *AJ*, *117*, 1578–1593, `https://doi.org/10.1086/300786`.

Bowman, J. D., Cairns, I., Kaplan, D. L., Murphy, T., Oberoi, D., Staveley-Smith, L., & Arcus, W. (2013). Science with the Murchison Widefield Array. *PASA*, *30*, `https://doi.org/10.1017/pas.2013.009` `http://dx.doi.org/10.1017/pas.2013.009`.

Briggs, D. S. (1995). High Fidelity Interferometric Imaging: Robust Weighting and NNLS Deconvolution. In *American Astronomical Society Meeting Abstracts*, volume 187 of *American Astronomical Society Meeting Abstracts* (pp. 112.02).

Callingham, J. R., Ekers, R. D., Gaensler, B. M., Line, J. L. B., Hurley-Walker, N., Sadler, E. M., & Tingay (2017). Extragalactic Peaked-spectrum Radio Sources at Low Frequencies. *ApJ*, *836*, 174, 174, `https://doi.org/10.3847/1538-4357/836/2/174`.

Condon, J. J. (1992). Radio emission from normal galaxies. *ARA&A*, *30*, 575–611, `https://doi.org/10.1146/annurev.aa.30.090192.003043`.

Condon, J. J., Cotton, W. D., Greisen, E. W., Yin, Q. F., Perley, R. A., Taylor, G. B., & Broderick, J. J. (1998). The NRAO VLA Sky Survey. *ApJ*, *115*, 1693–1716, `https://doi.org/10.1086/300337`.

Conway, R. G., Kellermann, K. I., & Long, R. J. (1963). The radio frequency spectra of discrete radio sources. *MNRAS*, *125*, 261, `https://doi.org/10.1093/mnras/125.3.261`.

xii

BIBLIOGRAPHY

de Gasperin, F., Intema, H. T., & Frail, D. A. (2018). A radio spectral index map and catalogue at 147-1400 MHz covering 80 per cent of the sky. *MNRAS*, *474*, 5008–5022, https://doi.org/10.1093/mnras/stx3125.

Duffy, P. & Blundell, K. M. (2012). The non-thermal emission of extended radio galaxy lobes with curved electron spectra. *MNRAS*, *421*(1), 108–115, https://doi.org/10.1111/j.1365-2966.2011.20239.x.

For, B. Q., Staveley-Smith, L., Hurley-Walker, N., Franzen, T., Kapińska, A. D., Filipović, M. D., & Collier, J. D. (2018). A multifrequency radio continuum study of the Magellanic Clouds - I. Overall structure and star formation rates. *MNRAS*, *480*(2), 2743–2756, https://doi.org/10.1093/mnras/sty1960.

Hamaker, J. P., Bregman, J. D., & Sault, R. J. (1996). Understanding radio polarimetry. I. Mathematical foundations. *A&A*, *117*, 137–147.

Hamaker, J. P. & Bregman, J. D. (1996). Understanding radio polarimetry. III. Interpreting the IAU/IEEE definitions of the Stokes parameters. *A&A*, *117*, 161–165.

Hamaker, J. P. (2000). Understanding radio polarimetry. IV. The full-coherency analogue of scalar self-calibration: Self-alignment, dynamic range and polarimetric fidelity. *A&A*, *143*, 515–534, https://doi.org/10.1051/aas:2000337.

Hancock, P. J., Sadler, E. M., Mahony, E. K., & Ricci, R. (2010). Observations and properties of candidate high-frequency GPS radio sources in the AT20G survey. *MNRAS*, *408*(2), 1187–1206, https://doi.org/10.1111/j.1365-2966.2010.17199.x.

Hancock, P. J., Murphy, T., Gaensler, B. M., Hopkins, A., & Curran, J. R. (2012). Compact continuum source finding for next generation radio surveys. *MNRAS*, *422*, 1812–1824, https://doi.org/10.1111/j.1365-2966.2012.20768.x.

Hancock, P. J., Trott, C. M., & Hurley-Walker, N. (2018). Source Finding in the Era of the SKA (Precursors): Aegean 2.0. *PASA*, *35*, e011, https://doi.org/10.1017/pasa.2018.3.

Harvey, V. M., Franzen, T., Morgan, J., & Seymour, N. (2018). A novel approach for characterizing broad-band radio spectral energy distributions. *MNRAS*, *476*, 2717–2730, https://doi.org/10.1093/mnras/sty386.

Higgins, J. P. T. & Green, S. (2008). *Cochrane handbook for systematic reviews of interventions.* Wiley-Blackwell.

Hogan, M. T., Edge, A. C., Geach, J. E., Grainge, K. J. B., Hlavacek-Larrondo, J., Hovatta, T., & Karim, A. (2015). High radio-frequency properties and variability of brightest cluster galaxies. *MNRAS*, *453*(2), 1223–1240, https://doi.org/10.1093/mnras/stv1518.

Högbom, J. A. (1974). Aperture Synthesis with a Non-Regular Distribution of Interferometer Baselines. *A&A*, *15*, 417.

Hurley-Walker, N. (2017). A Rescaled Subset of the Alternative Data Release 1 of the TIFR GMRT Sky Survey.

Hurley-Walker, N., Callingham, J. R., Hancock, P. J., Franzen, T. M. O., Hindson, L., Kapińska, A. D., & Morgan, J. (2017). GaLactic and Extragalactic All-sky Murchison Widefield Array (GLEAM) survey - I. A low-frequency extragalactic catalogue. *MNRAS*, *464*, 1146–1167, https://doi.org/10.1093/mnras/stw2337.

Hurley-Walker, N., Hancock, P. J., Franzen, T. M. O., Callingham, J. R., Offringa, A. R., Hindson, L., & Wu, C. (2019). GaLactic and Extragalactic All-sky Murchison Widefield Array (GLEAM) survey II: Galactic plane 345° < l < 67°, 180° < l < 240°. *PASA*, *36*, e047, e047, https://doi.org/10.1017/pasa.2019.37.

Hurley-Walker, N. (2019). GaLactic and Extragalactic All-sky MWA Survey - eXtended. In *Supernova Remnants: An Odyssey in Space after Stellar Death II* (pp. 48).

Intema, H. T., Jagannathan, P., Mooley, K. P., & Frail, D. A. (2017). The GMRT 150 MHz all-sky radio survey - First alternative data release TGSS ADR1. *A&A*, *598*, A78, https://doi.org/10.1051/0004-6361/201628536 https://doi.org/10.1051/0004-6361/201628536.

Jones, R. C. (1941). A New Calculus for the Treatment of Optical SystemsI. Description and Discussion of the Calculus. *J. Opt. Soc. Am.*, *31*(7), 488–493, https://doi.org/10.1364/JOSA.31.000488 http://www.osapublishing.org/abstract.cfm?URI=josa-31-7-488.

Kardashev, N. S. (1962). Nonstationarity of Spectra of Young Sources of Nonthermal Radio Emission. *Soviet Astronomy*, *6*, 317.

Kass, R. E. & Raftery, A. E. (1995). Bayes Factors. *Journal of the American Statistical Association*, *90*(430), 773–795, https://doi.org/10.1080/01621459.1995.10476572.

Kemball, A. & Wieringa, M. (2000). MeasurementSet definition version 2.0 https://casa.nrao.edu/aips2_docs/notes/229/229.html.

Lane, W. M., et al. (2014). The Very Large Array Low-frequency Sky Survey Redux (VLSSr). *MNRAS*, *440*, 327–338, https://doi.org/10.1093/mnras/stu256.

Large, M. I., Mills, B. Y., Little, A. G., Crawford, D. F., & Sutton, J. M. (1981). The Molonglo Reference Catalogue of Radio Sources. *MNRAS*, *194*(3), 693–704, https://doi.org/10.1093/mnras/194.3.693 https://doi.org/10.1093/mnras/194.3.693.

Leshem, A., van der Veen, A.-J., & Boonstra, A.-J. (2000). Multichannel Interference Mitigation Techniques in Radio Astronomy. *The Astrophysical Journal Supplement Series*, *131*(1), 355–373, https://doi.org/10.1086/317360 https://doi.org/10.1086%2F317360.

Line, J. L. B., Webster, R. L., Pindor, B., Mitchell, D. A., & Trott, C. M. (2017). PUMA: The Positional Update and Matching Algorithm. *PASA*, *34*, e003, e003, https://doi.org/10.1017/pasa.2016.58.

McConnell, D., Hotan, A., & Lenc, E. (2020). RACS - Rapid ASKAP Continuum Survey https://www.atnf.csiro.au/content/racs.

McKinley, B., Tingay, S. J., Carretti, E., Ellis, S., Bland-Hawthorn, J., Morganti, R., & Line (2017). The jet/wind outflow in Centaurus A: a local laboratory for AGN feedback. *MNRAS*, *474*(3), 4056–4072, https://doi.org/10.1093/mnras/stx2890 https://doi.org/10.1093/mnras/stx2890.

McMaster, W. H. (1954). Polarization and the Stokes Parameters. *American Journal of Physics*, *22*(6), 351–362, https://doi.org/10.1119/1.1933744.

McMullin, J. P., Waters, B., Schiebel, D., Young, W., & Golap, K. (2007). *CASA Architecture and Applications*, volume 376 of *Astronomical Society of the Pacific Conference Series*, (pp. 127).

Mitchell, D., Greenhill, L., Wayth, R., Sault, R., Lonsdale, C., Cappallo, R., & Morales, M. (2008). Real-Time Calibration of the Murchison Widefield Array. *IEEE Journal of Selected Topics in Signal Processing*, *2*(5), 707–717, https://doi.org/10.1109/jstsp.2008.2005327 http://dx.doi.org/10.1109/JSTSP.2008.2005327.

Ochsenbein, F. & Williams, R. (2009). VOTable Format Definition Version 1.2. IVOA Recommendation 30 November 2009.

Offringa, A. R., McKinley, B., Hurley-Walker, N., Briggs, F. H., Wayth, R. B., Kaplan, D. L., & Bell (2014). WSCLEAN: an implementation of a fast, generic wide-field imager for radio astronomy. *MNRAS*, *444*, 606–619, https://doi.org/10.1093/mnras/stu1368.

Offringa, A. R., Wayth, R. B., Hurley-Walker, N., et al. (2015). The Low-Frequency Environment of the Murchison Widefield Array: Radio-Frequency Interference Analysis and Mitigation. *PASA*, *32*.

Offringa, A. R., Trott, C. M., Hurley-Walker, N., Johnston-Hollitt, M., McKinley, B., Barry, N., & Beardsley, A. P. (2016). Parametrizing Epoch of Reionization foregrounds: a deep survey of low-frequency point-source spectra with the Murchison Widefield Array. *MNRAS*, *458*(1), 1057–1070, https://doi.org/10.1093/mnras/stw310 https://doi.org/10.1093/mnras/stw310.

Ord, S. M., Mitchell, D. A., Wayth, R. B., Greenhill, L. J., Bernardi, G., Gleadow, S., & Edgar, R. G. (2010). Interferometric Imaging with the 32 Element Murchison Wide-Field Array. *PASA*, *122*, 1353, https://doi.org/10.1086/657160.

Ord, S. M., Crosse, B., Emrich, D., Pallot, D., Wayth, R. B., Clark, M. A., & Tremblay, S. E. (2015). The Murchison Widefield Array Correlator. *PASA*, *32*, e006, e006, https://doi.org/10.1017/pasa.2015.5.

Perley, R. A., Chandler, C. J., Butler, B. J., & Wrobel, J. M. (2011). The Expanded Very Large Array: A New Telescope for New Science. *ApJ*, *739*(1), L1, L1, https://doi.org/10.1088/2041-8205/739/1/L1.

Perley, R. A. & Butler, B. J. (2017). An Accurate Flux Density Scale from 50 MHz to 50 GHz. *ApJS*, *230*(1), 7, 7, https://doi.org/10.3847/1538-4365/aa6df9.

Procopio, P., Wayth, R. B., Line, J., Trott, C. M., Intema, H. T., Mitchell, D. A., & Pindor, B. (2017). A High-Resolution Foreground Model for the MWA EoR1 Field: Model and Implications for EoR Power Spectrum Analysis. *PASA*, *34*, e033, e033, https://doi.org/10.1017/pasa.2017.26.

Rioja, M. J., Dodson, R., & Franzen, T. M. O. (2018). LEAP: an innovative direction-dependent ionospheric calibration scheme for low-frequency arrays. *MNRAS*, *478*(2), 2337–2349, https://doi.org/10.1093/mnras/sty1195 https://doi.org/10.1093/mnras/sty1195.

Sault, R. J., Hamaker, J. P., & Bregman, J. D. (1996). Understanding radio polarimetry. II. Instrumental calibration of an interferometer array. *A&A*, *117*, 149–159.

Schwarz, G. (1978). Estimating the Dimension of a Model. *Ann. Stat.*, *6*(2), 461–464, https://doi.org/10.1214/aos/1176344136 https://doi.org/10.1214/aos/1176344136.

Smirnov, O. M. (2011a). Revisiting the radio interferometer measurement equation. I. A full-sky Jones formalism. *A&A*, *527*, A106, A106, https://doi.org/10.1051/0004-6361/201016082.

Smirnov, O. M. (2011b). Revisiting the radio interferometer measurement equation. II. Calibration and direction-dependent effects. *A&A*, *527*, A107, A107, https://doi.org/10.1051/0004-6361/201116434.

Sokolowski, M., Colegate, T., Sutinjo, A. T., Ung, D., Wayth, R., Hurley-Walker, N., & Lenc, E. (2017). Calibration and Stokes Imaging with Full Embedded Element Primary Beam Model for the Murchison Widefield Array. *PASA*, *34*, e062, e062, https://doi.org/10.1017/pasa.2017.54.

Sutinjo, A., O'Sullivan, J., Lenc, E., Wayth, R. B., Padhi, S., Hall, P., & Tingay, S. J. (2015). Understanding instrumental Stokes leakage in Murchison Widefield Array polarimetry. *Radio Science*, *50*, 52–65, https://doi.org/10.1002/2014RS005517.

Taylor, M. B. (2005). TOPCAT & STIL: Starlink Table/VOTable Processing Software. In P. Shopbell, M. Britton, & R. Ebert (Eds.), *Astronomical Data Analysis Software and Systems XIV*, volume 347 of *Astronomical Society of the Pacific Conference Series* (pp.˜29).

Thompson, A. R., Clark, B. G., Wade, C. M., & Napier, P. J. (1980). The Very Large Array. *ApJS*, *44*, 151–167, https://doi.org/10.1086/190688.

Thompson, A. R. (2017). *Interferometry and Synthesis in Radio Astronomy*, chapter 15, (pp. 767–771). John Wiley Sons, Ltd.

Tingay, S. J., Goeke, R., Bowman, J. D., Emrich, D., Ord, S. M., Mitchell, D. A., & Morales, M. F. (2013). The Murchison Widefield Array: The Square Kilometre Array Precursor at Low Radio Frequencies. *PASA*, *30*, e007, e007, https://doi.org/10.1017/pasa.2012.007.

Ung, D. C. X. (2019). *Determination of Noise Temperature and Beam Modelling of an Antenna Array with Example Application using MWA*. PhD thesis http://link.library.curtin.edu.au/p?cur_dspace_dc20.500.11937/77989.

van der Laan, H. (1966). A Model for Variable Extragalactic Radio Sources. *Nature*, *211*, 1131–1133, https://doi.org/10.1038/2111131a0.

Wayth, R. B., Lenc, E., Bell, M. E., Callingham, J. R., Dwarakanath, K. S., Franzen, T. M. O., & For, B.-Q. (2015). GLEAM: The GaLactic and Extragalactic All-Sky MWA Survey. *PASA*, *32*, e025, e025, https://doi.org/10.1017/pasa.2015.26.

Wayth, R. B., Tingay, S. J., Trott, C. M., Emrich, D., Johnston-Hollitt, M., McKinley, B., & Gaensler, B. M. (2018). The Phase II Murchison Widefield Array: Design overview. *PASA*, *35*, 33, https://doi.org/10.1017/pasa.2018.37.

Wells, D. C., Greisen, E. W., & Harten, R. H. (1981). FITS - a Flexible Image Transport System. *A&A*, *44*, 363.